Reduced-order modeling: new approaches for computational physics[☆]

David J. Lucia[a,*], Philip S. Beran[b], Walter A. Silva[c]

[a] Air Force Research Laboratory, 2130 Eight Street, Suite 1, Building 45, WPAFB, OH 45433-7542, USA
[b] AFRL/VASD, Bldg 146, 2210 Eighth Street, WPAFB, OH 45433-7531, USA
[c] Aeroelasticity Branch, Mail Stop 340, NASA Langley Research Center, Hampton, VA 23681-0001, USA

Abstract

In this paper, we review the development of new reduced-order modeling techniques and discuss their applicability to various problems in computational physics. Emphasis is given to methods based on Volterra series representations, the proper orthogonal decomposition, and harmonic balance. Results are reported for different nonlinear systems to provide clear examples of the construction and use of reduced-order models (ROMs), particularly in the multi-disciplinary field of computational aeroelasticity. Unsteady aerodynamic and aeroelastic behaviors of two-dimensional and three-dimensional geometries are described. Large increases in computational efficiency are obtained through the use of ROMs, thereby justifying the initial computational expense of constructing these models and motivating their use for multi-disciplinary design analysis.
© 2003 Elsevier Ltd. All rights reserved.

Contents

---

*Corresponding author. Tel.: +1-937-656-6356; fax: +1-937-255-3740.
E-mail addresses: david.lucia@wpafb.af.mil (D.J. Lucia), philip.beran@wpafb.af.mil (P.S. Beran).

Nomenclature

System symbols

$\mathbf{F}$	implicit time integration function
$\mathbf{R}(\mathbf{w};\lambda)$	array of nonlinear functions
t	time
$\mathbf{w}$	vector of discretized full-system variables
Δt	time step size for integration
λ	any free parameter, or set of parameters

Aerodynamic symbols

L	reference length
m_x, m_y	fluid momentum components, ρu, ρv
M	Mach number
P	pressure, $P_d/\rho_\infty u_\infty^2$
Q	dynamic pressure
Re	reynolds number
u, v	fluid velocity components, $u_d/u_\infty, v_d/u_\infty$
x, y	spatial coordinates, $x_d/L, y_d/L$
γ	ratio of specific heats
ρ	density, ρ_d/ρ_∞

Volterra series symbols

$\mathbf{A}, \mathbf{B}, \mathbf{C}$	state-space matrix operators
$\mathbf{D}, \mathbf{P}, \mathbf{Q}$	singular value decomposition products
$\mathbf{H}_{rs}$	generalized Hankel matrix
$\mathbf{h}$	Volterra kernel function
K	number of time samples in impulse
n	time index
$\mathbf{P}$	vector of pressure on structure
q	number of states in realization
r	size of shift in data window
s	number of time samples in window
$\mathbf{u}$	vector of forcing inputs
$\mathbf{x}$	vector of dynamic states
$\mathbf{y}$	vector of measurement data
$\mathbf{Y}$	Markov parameter
β	scaling parameter

POD symbols

$\mathbf{A}$	frequency domain, linear dynamics matrix
$\hat{\mathbf{A}}$	reduced-order dynamics matrix
$\mathbf{b}, \tilde{\mathbf{b}}$	frequency domain, linearized forcing terms

$\hat{\mathbf{b}}$	reduced-order forcing term
$\mathbf{B}$	boundary operator
$\mathbf{e}$	basis vectors
$\mathbf{f}$	boundary state vector
$\mathbf{J}$	full-system Jacobian matrix
$\hat{\mathbf{J}}$	reduced-order Jacobian matrix
k	index on summation
M	number of DOFs for ROM
N	number of DOFs for full system

$Pe, \beta_1, \beta_2,$	
β_3, Γ	parameters for tubular reactor
$\mathbf{q}$	frequency domain amplitude disturbance
$\hat{\mathbf{q}}$	reduced variables in frequency domain
Q	number of snapshots taken
$\mathbf{S}$	matrix of field data, or snapshots
$\mathbf{V}$	matrix of eigenvectors of $S^{\mathrm{T}}S$
$\hat{\mathbf{w}}$	vector of reduced-order variables
$\mathbf{W}_0$	base solution
Φ	reduced-order mapping matrix

Harmonic balance symbols

$\mathbf{E}$	diagonal matrix of harmonic indicies
$\mathbf{R}^*$	harmonic flux term
	split operator source term
s	
$\mathbf{w}^n$	coefficients for the nth harmonic
	set of coefficients for all harmonics
$\mathbf{w}^*$	set of coefficients in periodic orbit

Subscripts

b	quantity on boundary
d	dimensional quantity
f	fluid system
n	Volterra kernel index
s	structural system
∞	freestream quantity, dimensional

Superscripts

n	time index
v	Newton iteration index

1. Introduction

1.1. Motivation

Prior to the recent appearance of powerful digital computers, it was necessary to construct models of physical behaviors that took advantage of existing analytical techniques or which involved numerical calculations with small numbers of degrees of freedom (DOFs). Now, partial differential equations, representative of complex physics that were previously unobtainable, can be discretized and integrated with numerical algorithms implemented on massive parallel supercomputers. Indeed, the simulation of nonlinear physical behaviors in even three space dimensions has become relatively commonplace; problems with millions of DOFs can be routinely simulated, thereby allowing investigators to capture precisely important phenomena. For example, as part of the Department of Energy's Accelerated Strategic Computing Initiative (ASCI), the world's fastest supercomputer (ASCI White—12 trillion calculations per second) is being used in a shift from nuclear test-based methods to computation-based methods.

In the absence of other tools and analysis, numerical simulation is often insufficient in itself to address complex physics. We see two main limitations of numerical simulation. First, while simulation can provide detailed time histories of discretized field variables, such data may not readily imbue the investigator with an increased level of understanding concerning the physics essential to a given phenomenon.

As is true of physical experiment, careful analysis of the data is required to develop simpler models that can be used to predict important characteristics of system behavior. This process can be impeded by the enormous size of computed data sets. Second, without the dedication of massive resources, numerical simulation of large systems remains far too computationally expensive to be used in various multi-disciplinary settings, including control model synthesis, multi-variable optimization, and stability prediction. For example, in the field of computational fluid dynamics (CFD), codes for the simulation of turbulent, viscous flows in three space dimensions are often used to obtain point solutions but are less frequently used in related disciplines, such as aeroelasticity and shape optimization. Thus, there is a fundamental gap between the analysis fidelity available to simulate an individual case and that practical for multi-disciplinary analysis.

Both limitations of numerical simulation suggest that computed data need to be distilled into lower-order models that can serve as the basis for additional analysis. The intent in constructing such reduced-order models (ROMs) is twofold: to provide quantitatively accurate descriptions of the dynamics of systems at a computational cost much lower than the original numerical model and to provide a means by which system dynamics can be readily interpreted. We think of a low-order model as a characterization of a physical process, such that the essential behaviors of the process are captured with a relatively small number of DOFs. The use of point vortices to simulate the nonlinear dynamics of vorticity generating systems is a simple example of low-order modeling. ROMs are low-order models derived from some appropriate projection of a full system's DOFs to a much smaller set that encapsulates most, if not all, of the system's fundamental dynamics. Model accuracy typically depends on the number of retained DOFs and the convergence properties of the ROM. The reduction in computational cost needed to solve the ROM is offset by a potential loss of accuracy and model robustness.

1.2. Definition of terms

The term "fidelity" is used to denote the degree to which a model captures the physics of a phenomenon of interest. Low fidelity implies that a computational model is missing key physical behaviors that render the model highly inaccurate in certain regimes, whereas high fidelity implies a broader range of model applicability. These terms alone are of ambiguous meaning; they are dependent on the class of problems to which models are applied. For example, the linear potential equation can form a very accurate basis for computing loads in the subsonic regime, especially if corrected for viscous effects. However, it is a low-fidelity representation of

flow behavior in the transonic regime, since leading-order (nonlinear) physical behavior is not properly modeled with this equation. Even in the subsonic regime, the linear potential equation may not be regarded to form the basis for a high-fidelity model if vehicles at large angles of attack are to be simulated. For a specified range of problem interest and physical behaviors, high-fidelity models capture the relevant physical behaviors using validated techniques to achieve acceptable levels of accuracy. Thus, use of high-fidelity models usually leads to accurate solutions. However, application of a high-fidelity model is not sufficient for accuracy, owing to the need to execute properly the model on a computer (e.g., proper construction of a grid and selection of a time step).

One important trend driving the development of new ROM techniques is the increasing level of fidelity within multi-disciplinary analysis and design, which is a necessary consequence of the need for increased performance and reliability in many systems. The general purpose of reduced-order modeling is to lower the computational DOFs present in a numerical model while retaining the model's fidelity, i.e., the model's ability to capture physics of interest. Point simulations using high-fidelity equation sets (e.g., Navier–Stokes equations) typically cannot be obtained fast enough to permit design. This situation will improve, but at the same time, it is likely that models of even greater fidelity will be desired as more complex interaction physics are addressed in simulation.

The use of the term "nonlinear" in this paper also deserves clarification. Each application discussed herein, encompassing both structural and fluid dynamics, is "linear" in the sense that all the solutions of interest can be formed via linear combination of some set of basis functions. POD is a linear technique in this sense, as is harmonic balance (HB). Even so, these techniques are able to properly treat "nonlinearity," because they can account for nonlinear coupling of terms acting within the linear space defined by the basis functions. In this paper, we will distinguish between two types of nonlinearity. The first type is nonlinear coupling of the time-varying states in the physics-based dynamics equations. The states are scalars in the simplest cases. For aeroelastic applications, these "temporal" nonlinearities are usually polynomial in nature, and the state variables typically represent modal amplitudes. The dynamics equations are classically referred to as nonlinear ordinary differential equations (ODEs). Linearizing about some equilibrium state eliminates these nonlinearities and yields a host of useful, linear reduced-order techniques (sometimes referred to as "time linearization"). The reduced-order methods described in this paper are suitable and have demonstrated to some extent the ability to model temporal nonlinearities. The second type of nonlinearity resides purely in

the spatial domain. This type refers to nonlinear and often discontinuous behavior of a spatial state variable (such as pressure in a fluid or temperature in structure) encountered by traversing the solution domain. Spatial nonlinearities arise within a geometric relationship due to nonlinear coupling of differential elements, resulting in nonlinear partial differential equations (PDEs). We distinguish spatial nonlinearity from temporal nonlinearity, because spatial nonlinearities can exist without the time dimension (referred to by some as "static" nonlinearities). For instance, steady-state solutions to many compressible flow problems contain standing shock waves. In aeroelastic applications, both temporal and spatial nonlinearities are coupled in the physics-based representations (this situation is sometimes called "dynamic" nonlinearity). In this case, the spatial nonlinearities can be stationary or move across the domain in time. When the nonlinearities are stationary, linearized dynamics equations are suitable for reduced-order modeling. When the nonlinearities are moving, the need for constant re-linearization makes these techniques impractical. Once the time domain and spatial domain are decoupled by modal approximations, the link between the two can be confusing. The ROM techniques presented in this paper are suitable for modeling moving, spatial nonlinearities. The ability of these techniques to address moving shocks and structural nonlinearities represents an exciting new capability for aeroelastic research and development.

One final definition is required to clearly relate what we mean by the term "moving shock." For this paper, a moving shock is defined as a dynamic spatial discontinuity that cannot be adequately modeled (errors less than 10%) via linearization. By "linearization," we imply linearization about a single, fixed shock location for all times of interest. In the literature, authors disagree on the use of this term. In many cases of interest, a shock wave of varying strength may appear and disappear periodically in an unsteady calculation. However, if the shock does not traverse a substantial distance, the overall flow field can be accurately approximated by linearizing about a single shock location. In our view, this case does not constitute shock motion, and we refer to such applications as addressing "stationary shocks". We do not mean to minimize the importance of what we term the "stationary shock" case, but we want to emphasize that large motions of a strong shock require special consideration for ROM development over and above those required for stationary shocks.

This paper reviews recent progress in the development of reduced-order modeling techniques and their application to multi-disciplinary problems, particularly in the area of computational aeroelasticity. The scope of the review is limited to the Volterra theory of nonlinear systems, the proper orthogonal decomposition (POD)

and HB. These three methods have been applied to the high-fidelity analysis of aeroelastic configurations in two and three space dimensions, and show great potential for continued practical use. The remainder of this introduction is devoted to an overview of these methods. Later in the paper, we describe a variety of applications where these methods have been employed with success.

1.3. Volterra theory of nonlinear systems

Over several decades of aerodynamics research, simple analytical models have given way to numerical descriptions of vehicle flight loads. This transition has been described by Silva [1] which we summarize here. Early mathematical models of unsteady aerodynamic response capitalized on the efficiency and power of superposition of scaled and shifted fundamental responses, or convolution. Classical models of two-dimensional airfoils in incompressible flow [2] include Wagner's function (response to a unit step variation in angle-of-attack (AoA)), Kussner's function (response to a sharp-edged gust in incompressible flow), Theodorsen's function (frequency response to sinusoidal motion), and Sear's function (frequency response to a sinusoidal gust). As geometric complexity increased, the analytical derivation of response functions was no longer practical, and the numerical computation of linear unsteady aerodynamic responses in the frequency domain became the method of choice [3]. When geometry and/or flow-induced nonlinearities were significant in the aerodynamic response of configurations of recent interest, the nonlinear equations were computed via time integration.

The trend towards time-domain numerical analysis of the aerodynamic equations has revealed the dynamics of numerous important and complex phenomena but has not provided a framework for the analysis of complex configurations without severe computational costs. Aeroelastic analyses involving coupling of the nonlinear aerodynamic equations with the linear structural equations have been particularly costly to carry out. Post-processing of time transients at numerous flight conditions can be used to compute stability boundaries of the coupled system, but this approach has not been used extensively in industry due to the prohibitively high computational costs.

Attempts to address the problem of high computational cost include the development of transonic indicial responses [4–6]. Transonic indicial (step) responses are responses due to a step excitation of a particular input, such as AoA, about a transonic (or non-linear) steady-state condition. Neural networks have also been used to develop nonlinear models of unsteady aerodynamics [7] and nonlinear models of maneuvers (using an experimental database) [6]. Neural networks and Volterra series have some similarities. Each involves the

characterization of a system via an input–output mapping [7,8]. In particular, there is a direct relationship between the weights of a neural network and the kernels of a Volterra series representation for a particular system [9].

A major difference between Volterra series and neural networks is in the training effort. Neural networks can require a substantial training effort [6] while Volterra series neither require a training period or curve fitting for model construction. Also, Volterra kernels provide a direct means for physical interpretation of a system's response characteristics in the time and frequency domains. However, potential disadvantages of the Volterra theory method include input amplitude limitations related to convergence issues and the need for higher-order kernels [1].

Another approach to reducing the computational cost of aerodynamic analysis with CFD is to restrict attention to linearized dynamics. The response of the linearized system about a nonlinear steady-state condition can be obtained with a linear state-space representation of the system at that condition. In this form, the order of the state-space model can be reduced using various techniques [10,11]. One method for building a linearized, low-order, frequency-domain model from CFD analysis is to apply the exponential (Gaussian) pulse input [12]. This method is used to excite the aeroelastic system, one mode at a time, using a broadband Gaussian pulse. The time-domain responses are transformed into the frequency domain to obtain a frequency-domain generalized aerodynamic force (GAF) influence coefficient matrix. These linearized GAFs can then be used in standard linear aeroelastic analyses [13]. Raveh et al. [14] apply this method while replacing the Gaussian pulse with step and impulse excitations. The responses to these alternate excitations can then be transformed into a state-space form for direct use in other disciplines such as controls or optimization [15]. We describe other frequency-domain representations in the context of the POD.

However, developing robust and efficient nonlinear CFD-based ROMs that are mathematically correct requires a rigorous method well defined in the time and frequency domains for continuous and discrete-time systems. The Volterra theory of nonlinear systems fulfills these requirements. In particular, this theory has found wide application in the field of nonlinear discrete-time systems [16] and nonlinear digital filters for telecommunications and image processing [17].

Application of nonlinear system theories, including the Volterra theory, to modeling nonlinear unsteady aerodynamic responses has not been extensive. One approach to modeling unsteady transonic aerodynamic responses is Ueda and Dowell's [18] concept of describing functions, which is a HB technique involving one harmonic. Tobak and Pearson [19] apply the continuous-time Volterra concept of functionals to indicial (step) aerodynamic responses to compute nonlinear stability derivatives. Jenkins [20] also investigates the determination of nonlinear aerodynamic indicial responses and nonlinear stability derivatives using similar functional concepts. Stalford et al. [21] develop Volterra models for simulating the behavior of a simplified nonlinear stall/post-stall aircraft model and the limit-cycle oscillations (LCOs) of a simplified wing-rock model. In particular, they establish a straightforward analytical procedure for deriving the Volterra kernels from known nonlinear functions.

A particular response from a CFD code may provide information regarding the nonlinear aerodynamic behavior of a complex configuration due to a particular input at a particular flight condition. It does not, however, provide general information regarding the behavior of the configuration to either a variation of the input or the flight condition or both. As a result, repeated use of the CFD code is necessary as input parameters and flight conditions are varied. A primary feature of the Volterra approach is the ability to characterize a linearized or nonlinear system using a small number of CFD-code analyses. Once characterized (via step or impulse responses of various orders), the functions can be implemented in a computationally efficient convolution scheme for prediction of responses to arbitrary inputs without the costly repeated use of the CFD code of interest. Characterization of the nonlinear response to an arbitrary input via the Volterra theory requires identification of the nonlinear Volterra kernels for a specified configuration and flight condition.

The problem of Volterra kernel identification is addressed by many investigators, including Rugh [22], Clancy and Rugh [23], Schetzen [24] and more recently by Boyd et al. [25] and Reisenthel [26]. There are several ways of identifying Volterra kernels in the time and frequency domains that can be applied to continuous- or discrete-time systems. Tromp and Jenkins [27] use indicial (step) responses from a Navier–Stokes CFD code and a Laplace domain scheme to identify the first-order kernel of a pitch-oscillating airfoil. Rodriguez [28] generates realizations of state-affine systems, which are related to discrete-time Volterra kernels, for aeroelastic analyses. Assuming high-frequency response, Silva [29] introduces the concept of discrete-time, aerodynamic impulse responses for a rectangular wing under linear (subsonic) and nonlinear (transonic) conditions. Silva [30] improves upon these results by extending the methodology to arbitrary input frequencies, resulting in the first identification of discrete-time impulse responses of an aerodynamic system. It should be noted that owing to separation of the input terms, Silva's first approach had limited applicability for the identification of nonlinear Volterra kernels [30], a situation which has been resolved more recently [1].

In his dissertation, Silva [1] discusses the then prevailing misconceptions concerning aerodynamic impulse responses, including the purported difficulty in computing such responses. These misconceptions primarily arise from fundamental differences between traditional, continuous-time theories and modern, discrete-time formulations. The appearance of discrete-time methods has great implications for aeroelasticity and aeroservoelasticity by providing a means for efficiently modeling nonlinear aerodynamics. In a similar fashion, other fields are likely to benefit from the coupling of large simulation codes and discrete-time response methods.

1.4. The Proper Orthogonal Decomposition

Before discussing the background of the POD, as applied to large, discrete systems, we will first summarize the role POD often plays in computational physics. Reduced-order modeling with POD is essentially analysis by an empirical spectral method. With spectral methods, field variables are approximated using expansions involving chosen sets of basis functions. The governing equations are manipulated to obtain sets of equations for the coefficients of the expansions that can be solved to predict the behavior of field variables in space and time. The POD is an alternative basis that is derived from a set of system observations. In short, samples, or snapshots, of system behavior are used in a computation of appropriate sets of basis functions to represent system variables. The POD is remarkable in that the selection of basis functions is not just appropriate, but optimal, in a sense to be described further in the Analysis section.

The need to obtain samples of system behavior to construct the POD-based ROM is both a strength and a weakness of the method. One strength is that models can be efficiently tuned to capture physics in a high-fidelity manner. Two noteworthy weaknesses are the need to compute samples with a high-order, high-fidelity method and the possible lack of model robustness to changes in parameters that govern system behavior. Generally, the payoff in applying POD is quite high. When following an initial investment of computation, a compact ROM can be constructed that can be used many times in, say, a multidisciplinary environment thar is valid over a useful range of system states.

The POD basis, otherwise known as the Karhunen–Loève (K–L) basis [31,32], dates to the 1940s for continuous systems. Use of the POD is also known as principal-component analysis in the statistical literature [33]. In fluid mechanics, the POD was first applied to the study of turbulence and the analysis of turbulent flow data [34,35]. Numerous studies since then have employed POD to characterize the turbulent properties and dominant, or coherent, structures of wall-bounded flows

and free shear layers using experimental data. This work, and much other activity related to the POD is thoroughly reviewed by Berkooz et al. [36] where references are given for early applications of POD in the fields of image processing, signal analysis, data compression, chemical engineering, and oceanography. Other references can be found in the fields of civil engineering [37,38] and structural dynamics [39,40].

More recently, computational data has been used in the construction of POD bases. For example, Moin and Moser [41] used data from a numerically simulated channel flow to compute characteristic structures within the channel flowfield. Sirovich also put forth the method of snapshots (or strobes) [42] to ease the computational burden of obtaining the K–L basis for a discrete system. With the method of snapshots, eigen analysis of an $M \times M$ matrix is carried out, where M is the number of snapshots, instead of an $N \times N$ matrix, where $N \gg M$ is the number of data points in a snapshot. This process will be described in Section 2.

With the successful interpretation of large computational data sets using POD, the technique was extended to the dynamical modeling of various systems, including fluid-dynamical systems. Through this approach, for example, fluid-dynamical systems are first simulated with CFD techniques, then samples are taken, a POD is constructed, and finally a set of low-order equations is formulated in the POD basis, typically with a Galerkin projection, to study the dynamics of the system. Deane et al. [43] give an early example of this process as applied to flows through grooved channels and about circular cylinders. In their noteworthy work, they successfully apply POD-based ROMs to the prediction of limit-cycle behavior in these systems. Other applications of POD to dynamic modeling of nonlinear heat transfer and fluid dynamic problems can be found elsewhere [44–47].

POD-based ROMs are now being developed for analyzing aeroelastic systems. Romanowski authored the first paper, which appeared quite recently, documenting reduction of the aeroelastic equations using a K–L basis [48]. His time-domain procedure involved the construction of a low-order model for the linearized dynamics of an airfoil with structural coupling about nonlinear static states computed with the Euler equations. Subsequent to this work, frequency-domain procedures have appeared that more efficiently compute POD basis functions for linearized aeroelastic systems [49,50]. Recent work has demonstrated the extension of POD techniques to analyzing problems in nonlinear aeroelasticity. Beran et al. [51] proposed and tested a computational framework for computing static and dynamic behaviors of nonlinear systems with POD-based ROMs that Pettit and Beran [52,53] have extended to treat the discrete Euler equations. This work formed the basis for several studies regarding nonlinear panel response in the transonic regime [54–56]. Dowell et al.

[57] have also used POD techniques to investigate the LCO of an airfoil with a nonlinear structural coupling in the transonic regime. Many of the results from these studies will be summarized later in this paper.

1.5. The Harmonic Balance approach

The recent advent of the HB approach into CFD was motivated by a desire to conduct design analysis for nonlinear, internal flow problems. HB is not a reduced-order modeling technique in the strictest sense. However, the computational savings can be significant for nonlinear, time-periodic, unsteady problems. In addition, the accuracy of the results make it a very attractive method. For these reasons, this innovative technique is gaining swift acceptance in the aeroelastic community as a viable approach for design analysis, and we chose to include HB as a subject for this paper. For the rest of the section, we incorporate the work of Maple [58] (with permission) to provide a brief introduction to HB and an overview of its history.

The HB method has been used for many years as a means of analyzing the behavior of harmonic ODEs [59]. The technique consists of assuming a solution in the form of a truncated Fourier series with a predetermined number of harmonics, substituting the assumed solution into the ODE, and algebraically manipulating the results to collect terms of like frequency. Any resulting terms with a frequency not in the Fourier series are dropped. Each harmonic is then balanced by requiring that like-frequency terms on each side of the equation satisfy equality independently. Balancing results in a system of coupled algebraic equations which are solved for the Fourier coefficients of the assumed solution.

It was not until recently that Hall et al. [60] adapted HB for CFD analysis of turbomachinery. High-fidelity numerical simulations of fluid flow through transonic turbomachinery are of considerable interest to designers of compressors and turbines in modern jet engines. Solutions can be obtained with conventional time-accurate CFD codes, but the considerable time required to generate these solutions limits their utility to the designer. Time-accurate calculations can be particularly inefficient for the class of problems where the flow is fully developed and periodic in time, such as flow past a rotor with oscillating blades or flow through a rotor–stator. It is usually necessary to step through many disturbance periods before a fully developed solution is reached. To achieve shorter computation times for this class of problem, CFD techniques have been developed that take advantage of the time-periodic nature of the flow. These techniques include the time-linearization technique [61–72]. The time-averaging technique [73–75] and the HB technique [60,76–78]. Of the three CFD techniques developed specifically for time-periodic flows, the HB technique is most suitable for modeling the large

disturbances and strong nonlinearities found in transonic turbomachinery.

Hall et al. [60] first used the HB method in CFD. They implemented a HB Reynolds-averaged Navier–Stokes solver and applied it to a single two-dimensional compressor blade row undergoing forced periodic vibration under transonic flow conditions. This configuration contained moderately strong shocks but limited shock motion. Solutions containing up to seven frequencies in the approximating series were calculated. Solutions containing three to five frequencies showed good agreement with standard time-accurate calculations for the time-average and first harmonic terms but took approximately one-tenth as long to compute. Solutions with seven frequencies failed to converge. In a follow-on effort, Thomas et al. [77] coupled an inviscid HB solver with a linear structural model to study LCOs of an aeroelastic system.

Additional work in HB CFD was conducted by McMullen et al. [76,78] who investigated several aspects of the HB method not previously addressed. Using a somewhat different formulation than Hall et al., they performed a stability analysis of the method and concluded that stability could be an issue when large numbers of frequencies were included in the solution. They applied the method to several test problems, including unsteady 1-D channel flow, 2-D oscillating flow behind a cylinder in crossflow, and a pitching airfoil. Their results show good agreement with analytical and numerical predictions for both time dependent and time-averaged data. Early cylinder crossflow calculations fixed the fundamental frequency at the theoretical frequency of vortex shedding [76]. Later cylinder crossflow and pitching airfoil calculations employed a gradient-based optimization approach to dynamically determine the correct fundamental frequency [78].

Finally, Maple et al. [58,79] have recently devised an adaptive HB method that employs a new multi-domain split-operator solution technique to remove a large-series stability restriction present in the non-adaptive approach. The adaptive method also minimizes the computational work required to obtain a HB solution by adapting the frequency content to the flow, starting with a small number of Fourier frequencies and augmenting the frequency content in each cell as necessary to capture local flow physics. The method reduces compute times by allowing larger integration time steps, reducing Fourier transform calculations, and reducing overall problem size.

Split-domain solutions to the 1-D inviscid Burgers' equation were computed with up to 97 frequencies, demonstrating improved stability [80]. Differences between harmonic balance solutions and time-accurate solutions were found to be asymptotic with Fourier series length. The adaptive split-domain approach was also applied to the 1-D and quasi-1-D Euler equations

[81]. Supersonic and subsonic Euler calculations showed that the adapted and non-adapted HB solutions were equivalent. Adapted quasi-1-D Euler solutions for a supersonic/subsonic diverging nozzle with periodic unsteady outflow conditions were generated in 86% less time than an equivalent non-adapted split-domain solution, demonstrating the benefit of adapting frequency content to local flow conditions. While the new adaptive approach is promising, additional research is required to extend the technique to higher space dimensions and investigate implementation and performance for aeroelastic problems.

1.6. Objectives, scope and layout of paper

The analysis section that follows develops the theory for each of the three reduced-order modeling approaches. Following the analysis section, we present results in three separate sections, one each concerning results obtained with the Volterra theory of nonlinear systems, the POD, and HB. Attention is primarily restricted to problems in unsteady aerodynamics and aeroelasticity, but results in other fields are drawn upon to show the wide applicability of the techniques. Volterra first-order kernels are used to simulate the unsteady response of viscous flows about driven airfoils and the aeroelastic response of airfoils and wings. Higher accuracy can be achieved with second-order kernels, and the relative improvement is quantified for selected configurations. We also report on Duke University's application of POD to the rapid prediction of flutter boundaries of airfoils and wings in the transonic regime [50,57] and Air Force Research Laboratory's investigation of reduced-order forms of the discrete Euler equations [52,54]. The paper is concluded with a summary of results obtained with the HB technique of Hall et al. [60] and the adaptive HB technique of Maple et al. [79].

2. Analysis

In this section, we review important aspects of the analytical foundation of Volterra theory, POD, and HB, as well as the application of these techniques to aerodynamic and aeroelastic systems. As described above, the POD is being applied in many different scientific and engineering disciplines, including aeroelasticity. While references are drawn from numerous sources, this review of POD analysis is not intended to be comprehensive but is focused on recent work with connectivity to Air Force research activities.

We will restrict our attention to solution vectors in N-dimensional, real, Euclidean space; these vectors will be written in boldface along with the matrices used in vector equations. Time-dependent vectors of spatially discretized field variables, referred to as full-system vectors, are written as $\mathbf{w}(t)$, where t is time.

2.1. Volterra theory

We begin by reviewing key features of the Volterra theory, as applied to time-invariant, nonlinear, continuous- and discrete-time systems. The literature on Volterra theory is rich, including several texts; [22, 82–84]. We follow the presentations of Silva [1,85] and Raveh et al. [14] to capture issues related to aeroelastic analysis. Furthermore, this section will concentrate on time-domain Volterra formulations consistent with the implied application to time-domain, computational aeroelasticity methods; the foundations and applications of frequency-domain Volterra theory can be found elsewhere [22,25,83,84].

2.1.1. Volterra kernels

While one goal of this work is to document the applicability of Volterra to discrete-time systems (e.g., systems arising in CFD), we first consider time-invariant, nonlinear, continuous-time, systems. Of interest is the response of the system about an initial state $\mathbf{w}(0) = \mathbf{W}_0$ due to an arbitrary input $u(t)$ (we take u as a real, scalar input, such as pitch angle of an airfoil) for $t \geqslant 0$. As applied to these systems, Volterra theory yields the response:

$$
\begin{aligned}
\mathbf{w}(t) = \mathbf{h}_0 &+ \int_0^t \mathbf{h}_1(t - \tau)u(\tau)\,\mathrm{d}\tau \\
&+ \int_0^t \int_0^t \mathbf{h}_2(t - \tau_1, t - \tau_2)u(\tau_1)u(\tau_2)\,\mathrm{d}\tau_1\,\mathrm{d}\tau_2 \\
&+ \sum_{n=3}^N \int_0^t \cdots \int_0^t \mathbf{h}_n(t - \tau_1, \ldots, t - \tau_n) \\
&\times u(\tau_1)\ldots u(\tau_n)\,\mathrm{d}\tau_1\ldots\mathrm{d}\tau_n.
\end{aligned}
\tag{1}
$$

The Volterra series in expression (1) contains three classes of terms. The first class is the steady-state term satisfying the initial condition, $\mathbf{h}_0 = \mathbf{W}_0$. Next is the first response term, $\int_0^\infty \mathbf{h}_1(t - \tau)u(\tau)\,\mathrm{d}\tau$, where $\mathbf{h}$ is known as the first-order kernel (or the linear unit impulse response). The identification of the kernel $\mathbf{h}(\tau_1)$ is based on measuring the response of the system to a unit impulse (Dirac delta function) at $\tau_1 = 0$. Eq. (1) requires the system to be time invariant, so that the system responds in an identical manner (but translated in time) to an impulse at any $\tau_1 > 0$. The first response term represents the convolution of the first-order kernel with the system inputs for times between 0 and t, where by causality, inputs beyond time t are excluded. Last, are the higher-order terms involving the second-order kernel, $\mathbf{h}_2$, and the nth-order kernels, $\mathbf{h}_n$. These terms do not all vanish when the system is nonlinear [85]. For example, identification of the second-order kernel is

based on measuring the two-dimensional response of the system following impulse inputs at two different times. More will be said about kernel identification shortly.

The convergence of the Volterra series is dependent on input magnitude and the degree of system non-linearity. Boyd [86] shows that the convergence of the Volterra series cannot be guaranteed when the maximum value of the input exceeds a critical value, which is system dependent. Of course, the issue of convergence is important, since the Volterra series must be truncated for analysis of practical systems. Silva [1,85] and Raveh et al. [14] consider a weakly nonlinear formulation, where it is assumed that the Volterra series can be accurately truncated beyond the second-order term:

$$\mathbf{w}(t) = \mathbf{h}_0 + \int_0^t \mathbf{h}_1(t - \tau)u(\tau)\,d\tau$$
$$+ \int_0^t \int_0^t \mathbf{h}_2(t - \tau_1, t - \tau_2)u(\tau_1)u(\tau_2)\,d\tau_1\,d\tau_2. \quad (2)$$

The assumption of a weakly nonlinear system is consistent with the emergence of LCO of a 2-D aeroelastic system in transonic flow through a super-critical Hopf bifurcation [51]. For linear systems, only the first-order kernel is non-trivial, and there are no limitations on input amplitude.

Silva [1] derives the first- and second-order kernels, which are presented here in final form in terms of various response functions:

$$\mathbf{h}_1(\tau_1) = 2\mathbf{w}_0(\tau_1) - \frac{1}{2}\mathbf{w}_2(\tau_1), \quad (3)$$

$$\mathbf{h}_2(\tau_1, \tau_2) = \frac{1}{2}(\mathbf{w}_1(\tau_1, \tau_2) - \mathbf{w}_0(\tau_1) - \mathbf{w}_0(\tau_2)). \quad (4)$$

In (3), $\mathbf{w}_0(\tau_1)$ is the time response of the system to a unit impulse applied at time 0 and $\mathbf{w}_2(\tau_1)$ is the time response of the system to an impulse of twice unit magnitude at time 0. These response functions represent the memory of the system. If the system is linear, then $\mathbf{w}_2 = 2\mathbf{w}_0$ and $\mathbf{h}_1 = \mathbf{w}_0$, which is why the first-order kernel is referred to as the linear unit impulse response. The identification of the second-order kernel is more demanding, since it is dependent on two parameters. Assuming $\tau_2 > \tau_1$ in (4), $\mathbf{w}_0(\tau_2)$ is the response of the system to an impulse at time τ_2.

Time is discretized with a set of time steps of equivalent size. Time levels are indexed from 0 (time 0) to n (time t), and the evaluation of $\mathbf{w}$ at time level n is denoted by $\mathbf{w}[n]$. The convolution in discrete time is

$$\mathbf{w}[n] = \mathbf{h}_0 + \sum_{k=0}^N \mathbf{h}_1[n - k]u[k]$$
$$+ \sum_{k_1=0}^N \sum_{k_2=0}^N \mathbf{h}_2[n - k_1, n - k_2]u[k_1]u[k_2]. \quad (5)$$

It should be noted that there is a fundamental difference between a continuous-time unit impulse response and a discrete-time unit impulse response [1,85]. The continuous-time unit impulse response is a highly abstract function which suffers from a difficult, if not impossible, practical (i.e., numerical) application. On the other hand, the discrete-time unit impulse response (also known as a unit sample response) is specifically designed for discrete-time (i.e., numerical) applications [87].

Finally, other related activities include fundamental research in the area of frequency-domain Volterra theory [88] and experimental applications of Volterra methods as applied to nonlinear aeroelastic problems [89].

2.1.2. Generalized aerodynamic forces

A GAF is a force that does work in the direction of a degree of freedom. From Lagrangian dynamics, the equations of motion of a system can be defined based on the DOFs of the system. For an aeroelastic system, the DOFs are the structural modes. Therefore, an aero-elastic generalized force is the projection of the aerodynamic pressures onto each structural mode shape. Therefore, there will be as many generalized forces as there are structural modes in a problem. Also, a generalized force does not necessarily have the usual units of force, as it could be a moment (torque) or a force along a particular mode shape that does not have a direct interpretation in terms of traditional force concepts.

GAFs are important to the Volterra ROM method, because they are used to couple the fluid dynamics with the structural dynamics. The behavior of the GAFs are described by scalar magnitudes, and the GAF dynamics are replicated using the Volterra approach. The effect of the fluid dynamics on the structure is then modelled by coupling the GAF dynamics with the modal structural dynamics.

2.1.3. Linear ROMs via the eigenvalue realization algorithm

The identification of linearized and nonlinear Volterra kernels is an essential step in the development of ROMs based on Volterra theory, but it is not the final step. Ultimately, these functional kernels can be transformed into linearized and nonlinear (bilinear) state-space systems that can be easily implemented into other disciplines such as controls and optimization [1,22]. The eigenvalue realization algorithm (ERA) [90] was successfully used to generate a linear, state-space ROM for an aeroelastic application by Silva and Raveh [15]. Results will be discussed later. The following development of ERA is taken from Lucia and Beran [91]. Currently, research is underway to develop methods for synthesizing nonlinear ROMs in state-space form using

the Volterra approach, but no results are available as of yet.

The ERA method identifies a discrete, linear, time-invariant state-space realization of the form

$$\mathbf{x}[n + 1] = \mathbf{A}\mathbf{x}[n] + \mathbf{B}\mathbf{u}[n],$$
$$\mathbf{y}[n] = \mathbf{C}\mathbf{x}[n], \qquad (6)$$

using data from a complete ensemble of impulse responses. Initial state responses can be used in lieu of impulse responses, but we only consider impulse response data in this overview for simplicity. The systems realization procedure takes measurement data $\mathbf{y}[n]$ from the free response of the system and produces a minimal state-space model $\mathbf{A}$, $\mathbf{B}$, and $\mathbf{C}$ such that functions $\mathbf{y}$ are accurately reproduced. For aeroelastic ROM realization, Silva and Raveh [15] used the measurement data $\mathbf{w}_0$ introduced in the previous section. The model output $\mathbf{y}[n]$ was $\mathbf{w}[n]$ from the linear portion of (5). In Silva's implementation, the state dimensionality (length of the vector $\mathbf{x}$) was generally larger than the length of $\mathbf{y}$, which was required for model accuracy and robustness. In a related work, Lucia and Beran used ERA in a new hybrid POD-Volterra approach [91]. In this case, the model output $\mathbf{y}[n]$ was the modal amplitude vector $\hat{\mathbf{w}}[n]$ to be introduced in (13), and the state dimensionality of $\mathbf{x}$ was equal to the number of POD modes. A full development of this variant will be provided in Section 2.4.

The ERA method is summarized as follows. The free pulse response of linear, time invariant, discrete systems is given by a function known as the Markov parameter:

$$\mathbf{Y}[n] = \mathbf{C}\mathbf{A}^{n-1}\mathbf{B}. \qquad (7)$$

The superposition principle states that a system response to any arbitrary input can be obtained from a linear combination of impulse responses from that system. A generalized Hankel matrix of impulse responses is related to the Markov parameter by the superposition principle. The Hankel matrix is formed by windowing the impulse response data. A total of K data points are provided at discrete time steps $t = t_1, \ldots, t_K$, and the $r \times s$ Hankel matrix $\mathbf{H}_{rs}$ is formed as follows:

$$\mathbf{H}_{rs}^{n-1} = \begin{bmatrix} \mathbf{Y}[n] & \cdots & \mathbf{Y}[n + t_{s-1}] \\ \mathbf{Y}[j_1 + n] & \cdots & \mathbf{Y}[j_1 + n + t_{s-1}] \\ \vdots & \vdots & \vdots \\ \mathbf{Y}[j_{r-1} + n] & \cdots & \mathbf{Y}[j_{r-1} + n + t_{s-1}] \end{bmatrix}, \qquad (8)$$

where s is the total size of the data window, and r is the number of time steps used to shift the data window. The choice of r and s is arbitrary as long as $r + s + k \leqslant K + 2$.

The ERA method eliminates redundant data by using singular value decomposition (SVD) on $\mathbf{H}_{rs}^0$,

$$\mathbf{H}_{rs}^0 = \mathbf{P}\mathbf{D}\mathbf{Q}^{\mathrm{T}}. \qquad (9)$$

Unwanted state dimensionality is eliminated by truncating the elements of $\mathbf{P}, \mathbf{D}$, and $\mathbf{Q}$ associated with very small singular values of $\mathbf{H}_{rs}^0$. The number of states is reduced to a minimal number q. The number of observations p and the number of forcing terms m are known from the problem formulation. The dimension of the Markov parameter $\mathbf{Y}[n]$ is $p \times m$. Algebra is used to recast (7) in terms of the time shifted Hankel matrix $\mathbf{H}_{rs}^1$, and the elements $\mathbf{P}$, $\mathbf{D}$, and $\mathbf{Q}$. The state-space realization flows from this manipulation, and is as follows:

$$\mathbf{A} = \mathbf{D}^{-1/2}\mathbf{P}^{\mathrm{T}}\mathbf{H}_{rs}^1\mathbf{Q}\mathbf{D}^{-1/2}, \qquad (10a)$$

$$\mathbf{B} = \mathbf{D}^{1/2}\mathbf{Q}^{\mathrm{T}}\mathbf{E}_m, \qquad (10b)$$

$$\mathbf{C} = \mathbf{E}_p^{\mathrm{T}}\mathbf{P}\mathbf{D}^{1/2}. \qquad (10c)$$

$\mathbf{E}_p^{\mathrm{T}}$ and $\mathbf{E}_m^{\mathrm{T}}$ are defined below:

$$\mathbf{E}_p^{\mathrm{T}} = [\mathbf{I}_p, \mathbf{0}_p, \ldots, \mathbf{0}_p], \qquad (11a)$$

$$\mathbf{E}_m^{\mathrm{T}} = [\mathbf{I}_m, \mathbf{0}_m, \ldots, \mathbf{0}_m], \qquad (11b)$$

where $\mathbf{0}_p$ and $\mathbf{0}_m$ as the null matrices of order p and m, respectively, and $\mathbf{I}_p$ and $\mathbf{I}_m$ are the identity matrices of order p and m.

2.2. Proper orthogonal decomposition

POD is a linear method for establishing an optimal basis, or modal decomposition, of an ensemble of continuous or discrete functions. Detailed derivations of the POD and its properties are available elsewhere [92,93] and not repeated herein. This section describes how the POD basis functions are obtained for aeroelastic applications and a variety of ways these basis functions have been used to address aeroelastic phenomena.

2.2.1. Obtaining basis functions with POD

In our discussion of POD, M basis vectors are used to represent deviations of $\mathbf{w}(t)$ from a base solution, $\mathbf{W}_0$. These are written as $\{\mathbf{e}^1, \mathbf{e}^2, \ldots, \mathbf{e}^M\}$ and are referred to by many names, including POD vectors [50], empirical eigenfunctions [92] or simply, modes [52,92]. For the sake of brevity, we shall use the term "modes" to denote the POD basis vectors. The modes are orthonormal

$$\mathbf{e}^{iT}\mathbf{e}^j = \begin{cases} 1 & \text{if } i = j, \\ 0 & \text{otherwise} \end{cases} \qquad (12)$$

and computed in a manner to be described shortly. The modal decomposition of $\mathbf{w}$ using M modes is given by

$$\mathbf{w} \approx \mathbf{W}_0 + \sum_{i=1}^{M} \hat{w}_i \mathbf{e}^i = \mathbf{W}_0 + \mathbf{\Phi}\hat{\mathbf{w}}, \qquad (13)$$

where $\mathbf{\Phi}$ is an $N \times M$ matrix containing the ordered set of modes, $\mathbf{\Phi} = [\mathbf{e}^1, \mathbf{e}^2, \ldots, \mathbf{e}^M]$, and $\hat{\mathbf{w}}$ is an M-dimensional

vector of modal amplitudes, $\hat{\mathbf{w}} = [\hat{w}_1, \hat{w}_2, \ldots, \hat{w}_M]$. As a time-varying function, $\mathbf{w}$ is approximated by $\mathbf{W}_0 + \mathbf{\Phi}\hat{\mathbf{w}}(t)$.

As stated by Holmes et al. [92], "Linearity is the source of the [POD] method's strengths as well as its limitations ...". The method is linear, owing to the independence of the modes from the modal amplitudes, thereby allowing for the straightforward construction of reduced-order equation sets from the full equation sets following mode computation.

The POD modes are constructed by first computing samples, or snapshots, of system behavior (solutions at different instants in time for dynamic problems, or equilibrium solutions at different parameter values for static problems) and by storing these samples in a snapshot matrix, $\mathbf{S}$. For now, we assume that M snapshots are collected and column-wise collocated into the $N \times M$ snapshot matrix: $\mathbf{S} = [\mathbf{w}^1, \mathbf{w}^2, \ldots, \mathbf{w}^M]$. By assumption, the snapshot matrix represents a random vector class of signals associated with the system. The basis provided by the POD, known as the K–L basis [31,32], minimizes the error in approximating a member of this class with fewer than M basis vectors. This property of optimal convergence associated with the K–L basis is established in many works [50,92–95]. The K–L basis can be readily computed by relating the mode matrix to the snapshot matrix through a transformation matrix V, $\mathbf{\Phi} = \mathbf{SV}$, maximizing the projection of the snapshot matrix onto the POD basis. This leads to the eigenproblem

$$\mathbf{S}^{\mathrm{T}}\mathbf{SV} = \mathbf{V\Lambda} \qquad (14)$$

for eigenvectors $\mathbf{V}$ and eigenvalues $\mathbf{\Lambda} = \mathrm{diag}(\lambda_i)$. The eigenvalues are non-negative, since $\mathbf{S}^{\mathrm{T}}\mathbf{S}$ is symmetric and positive semi-definite. Provided that the eigenvectors $\mathbf{V}$ are scaled to be orthonormal, $\mathbf{V}^{\mathrm{T}}\mathbf{V} = \mathbf{I}$ ($\mathbf{I}$ is the identity matrix), the transformation formula $\mathbf{\Phi} = \mathbf{SV}$ yields $\mathbf{\Phi}^{\mathrm{T}}\mathbf{\Phi} = \mathbf{\Lambda}$. Multiplying each $\mathbf{e}^i$ by $\sqrt{\lambda_i}$ yields an orthonormal set of modes, $\mathbf{\Phi}^{\mathrm{T}}\mathbf{\Phi} = \mathbf{I}$, as originally specified. It should be noted that for their frequency domain analysis, Hall et al. construct complex modes from $\mathbf{S}^H\mathbf{SV} = \mathbf{V\Lambda}$, where $\mathbf{S}^H$ is the complex conjugate of the transpose of $\mathbf{S}$.

In practice, fewer than M modes are retained to simulate system behavior. These are selected based on the size of the modal eigenvectors. Simply put, the K–L basis for a subspace of dimension $M_r < M$ is obtained by retaining the modes associated with the M_r largest eigenvalues computed in (14). It should also be noted that K–L theory establishes the K–L basis to be the eigenvectors of $\mathbf{SS}^{\mathrm{T}}/M$, where $\mathbf{SS}^{\mathrm{T}}$ is the snapshot covariance matrix. Manipulation of (14) yields $\mathbf{SS}^{\mathrm{T}}\mathbf{\Phi} = \mathbf{\Phi\Lambda}$, and from the singular value decomposition of $\mathbf{S}$, M eigenvalues are equivalent to those in $\mathbf{\Lambda}$, while the other $N{-}M$ eigenvalues vanish (for finite-dimensional problems of dimension N) [96]. Computation of $\mathbf{V}$ followed

by evaluation of $\mathbf{\Phi} = \mathbf{SV}$ much more efficiently yields the POD modes than explicit analysis of the covariance matrix. In the following, we will consider the number of modes retained to be a variable denoted by M that is less than equal to the number of snapshots in $\mathbf{S}$.

The techniques described below provide different means for obtaining reduced-order equations sets governing $\mathbf{w}(t)$ in the POD subspace. There are several methods for accomplishing the projection, and we will describe several approaches herein.

2.2.2. Full-system description

We place the nonlinear and spatially discretized, full-system equations in first-order form:

$$\frac{\mathrm{d}\mathbf{w}}{\mathrm{d}t} = \mathbf{R}(\mathbf{w}; \lambda), \qquad (15)$$

where $\mathbf{w}$ is an array of variables associated with interior evaluation points (e.g., cell centers) throughout a computational domain; λ is a free parameter (or set of parameters); $\mathbf{R}$ is an array of nonlinear functions of the discrete variables, and t is time. For the discrete Euler equations in two space dimensions and conservative form, $\mathbf{w}$ is a collocation of density, two components of momentum, and total energy, involving $N = 4N_p$ variables, where N_p is the number of interior evaluation points. We also define an array of variables associated with boundary grid points (so-called ghost points), $\mathbf{w}_b$, that are referenced in the evaluation of $\mathbf{R}$ but not explicitly carried as variables. The $4N_b$ boundary conditions are specified in general form as

$$\mathbf{B}(\mathbf{w}, \mathbf{w}_b) = \mathbf{f}(t), \qquad (16)$$

where $\mathbf{B}$ can be nonlinear in $\mathbf{w}$ and $\mathbf{w}_b$, and $\mathbf{f}$ is a time-dependent array representative of an evolving boundary state. Note that $\mathbf{B}$ is not related to the state-space matrix using the same symbol in (6). When $\mathbf{f}$ vanishes, equilibrium states, $\mathbf{W}$, of (15) exist and satisfy $\mathbf{R}(\mathbf{W}; \lambda) = \mathbf{0}$ and $\mathbf{B}(\mathbf{W}, \mathbf{W}_b) = \mathbf{0}$.

2.2.3. Linear (frequency domain) ROM formulation

Rapid progress has been made in the application of POD to aerodynamic and aeroelastic equation sets using a linear POD formulation [50]. The basic approach is to develop POD-based ROMs for the linearized dynamics about equilibrium solutions of the fully non-linear equations (15). For a given value of λ (e.g., Mach number), the nonlinear base solution is computed with CFD methods accelerated for steady-state conditions. The governing equations are then linearized for periodic disturbances of small amplitude, placed in frequency-domain form, and solved using similarly accelerated CFD methods. Solutions of the linearized equations gathered for a range of different frequencies serve as snapshots in the construction of a POD-based, linear ROM. Furthermore, a linearized ROM representative of

the aerodynamics can be attached to a set of nonlinear structural dynamic equations to form a low order, nonlinear aeroelastic model [50,97].

Following Hall et al. [50], small disturbance to the equilibrium state is introduced:

$$\mathbf{w}(t; \lambda) = \mathbf{W}(\lambda) + \mathbf{q}e^{j\omega t}, \tag{17}$$

where ω is the disturbance frequency; $\mathbf{q}$ is a disturbance of small amplitude; j is the imaginary number. The disturbance is a response to forced oscillation about the equilibrium state at the boundary (e.g., a response in fluid velocity to the time rate-of-change of AoA for a pitching airfoil):

$$\mathbf{B}(\mathbf{w}, \mathbf{w}_b) = \frac{\mathrm{d}}{\mathrm{d}t}\mathbf{b}e^{j\omega t} = j\omega \mathbf{b}e^{j\omega t}, \tag{18}$$

where $\mathbf{b}$ represents the type of forcing applied to the system. Introducing $\mathbf{w}_b = \mathbf{W}_b + \mathbf{q}_b e^{j\omega t}$ leads to a small-disturbance boundary equation (assuming the invertability of $\partial \mathbf{B}/\partial \mathbf{w}_b$):

$$\frac{\partial \mathbf{B}}{\partial \mathbf{w}_b}\mathbf{q}_b = j\omega \mathbf{b} - \frac{\partial \mathbf{B}}{\partial \mathbf{w}}\mathbf{q}. \tag{19}$$

This equation is coupled to the small-disturbance form of the governing equation

$$\mathbf{J}\mathbf{q} + \frac{\partial \mathbf{R}}{\partial \mathbf{w}_b}\mathbf{q}_b = j\omega \mathbf{q}, \tag{20}$$

where $\mathbf{J} \equiv \partial \mathbf{R}/\partial \mathbf{w}$ is the system Jacobian (an $N \times N$ real matrix). Combining both sets of equations yields

$$\mathbf{A}\mathbf{q} = j\omega \tilde{\mathbf{b}},$$
$$\mathbf{A} \equiv \frac{\partial \mathbf{R}}{\partial \mathbf{w}_b}\frac{\partial \mathbf{B}^{-1}}{\partial \mathbf{w}_b}\frac{\partial \mathbf{B}}{\partial \mathbf{w}} + j\omega \mathbf{I}, \quad \tilde{\mathbf{b}} \equiv \frac{\partial \mathbf{R}}{\partial \mathbf{w}_b}\frac{\partial \mathbf{B}^{-1}}{\partial \mathbf{w}_b}\mathbf{b}. \tag{21}$$

The solution of (21), $\mathbf{q}$, is a function of the forcing frequency, ω, and the character and amplitude of the forcing as expressed through $\mathbf{b}$.

It should be noted that (21) is based solely on the spatial discretization leading to $\mathbf{R}$ and does not account for the iterative character of numerical schemes by which $\mathbf{q}$ is computed. For example, Hall et al. obtain an equation with structure equivalent to that of (21) using an explicit, cell-centered, finite-volume Godunov method, but derive an expression for a Lax–Wendroff scheme that contains additional terms which are second order in ω [50].

The POD is constructed using M solutions $\mathbf{q}^i$ ($i = 1, \ldots, M$) of (21), for different frequencies and forcing conditions (e.g., airfoil pitch and airfoil plunge), as column entries in the complex snapshot matrix, $\mathbf{S}$ [50]. As has been reported, accuracy can be retained while keeping M quite small; M is typically between 10 and 100. Approximately half of the solutions need not be computed from (21), since solutions $\mathbf{q}$ at negative frequencies are complex conjugates of those at positive frequencies. The complex mode matrix $\mathbf{\Phi}$ is computed by first solving the complex form of (14), and then

forming the product $\mathbf{SV}$. To predict the time-dependent response about the equilibrium state, $\mathbf{q}$ is approximated by $\mathbf{\Phi}\hat{\mathbf{q}}$ ($\hat{\mathbf{q}}$ is the array of reduced-order variables) and substituted into the small-disturbance equation (21): $\mathbf{A}\mathbf{\Phi}\hat{\mathbf{q}} = j\omega\tilde{\mathbf{b}}$. Hall et al. [50] project this equation onto the space spanned by $\mathbf{\Phi}$ to obtain a reduced-order set of equations:

$$\hat{\mathbf{A}}\hat{\mathbf{q}} = j\omega\hat{\mathbf{b}} \quad (\hat{\mathbf{A}} \equiv \mathbf{\Phi}^H\mathbf{A}\mathbf{\Phi}, \ \hat{\mathbf{b}} \equiv \mathbf{\Phi}^H\tilde{\mathbf{b}}). \tag{22}$$

Returning to the original system, (21), we see the advantage of the POD formulation. If several solutions of (21) are required for different forcing conditions, the matrix $\mathbf{A}$ may be LU-decomposed or may be analyzed for eigenmodes that will dominate in the predicted response. Such "up-front" computations reduce the per unit computational cost of solutions beyond the first, but become impractical when N becomes sufficiently large, since the computational effort grows at a much faster rate than the number of equations. For example, on square computational domains, the decomposition of $\mathbf{A}$ grows as N^2.

With POD, the up-front cost is far less than that just described. The empirical eigenvectors are computed once in no more than $O(NM^2)$ operations (the product $\mathbf{S}^H\mathbf{S}$). These eigenvectors are used in the construction of $\hat{\mathbf{A}}$, which also requires $O(NM^2)$ operations (assuming $\mathbf{A}$ is not explicitly formed, but implied through the computation of $\mathbf{A}\mathbf{\Phi}_i$ as suggested by Hall et al. [50]. In practice, M is sufficiently small that the work is dominated by computation of the snapshots, a process requiring $O(NM)$ operations. Furthermore, for a specified level of accuracy, M does not typically grow with N; i.e., beyond a nominal threshold. Grid refinement does not better capture low-frequency, high-energy structures. Once (22) is formed through a set of transformations involving the empirical eigenvectors, many different cases ($O(N)$) can be examined at a commensurate cost, owing to the smallness of $\hat{\mathbf{A}}$ (an $M \times M$ matrix). Accuracy of the approach is high, provided that a sufficient number of modes are retained and provided that the forcing conditions are within the scope of the sampling process.

The POD approach is well-suited to multi-disciplinary analysis involving repeated interactions between equation sets. A POD-based ROM can be used to simplify a computationally demanding equation set so that it can be efficiently integrated with a simpler equation set. For example, Hall et al. [50] apply their analysis to the study of an isolated airfoil in transonic flow with pitch (α) and plunge (h) structural coupling. Their development is now summarized. Following collocation of the structural variables into the array $\mathbf{h} = (h, \alpha)^{\mathrm{T}}$, the structural dynamic equations are expressed as

$$\begin{bmatrix} -\mathbf{I} & \mathbf{0} \\ \mathbf{0} & \mathbf{M} \end{bmatrix}\frac{\mathrm{d}}{\mathrm{d}t}\begin{bmatrix} \mathbf{h} \\ \dot{\mathbf{h}} \end{bmatrix} + \begin{bmatrix} \mathbf{0} & \mathbf{I} \\ \mathbf{K} & \mathbf{0} \end{bmatrix}\begin{bmatrix} \mathbf{h} \\ \dot{\mathbf{h}} \end{bmatrix} = \begin{bmatrix} \mathbf{0} \\ \mathbf{F}(\mathbf{w}) \end{bmatrix}, \tag{23}$$

where $\mathbf{M}$ is a 2×2 matrix containing the airfoil mass, static imbalance and moment of inertia (about the elastic axis); $\mathbf{K}$ is the 2×2 stiffness matrix; $\mathbf{F}$ is an array representing the integration of the discrete flowfield into an applied force and moment, and $\dot{\mathbf{h}} = \mathrm{d}\mathbf{h}/\mathrm{d}t$).

Here, (23) is placed in small-disturbance form assuming that aeroelastic equilibrium is achieved when $\mathbf{h} = 0$, such that $\mathbf{h} = \mathbf{h}_0 e^{j\omega t}$ and $\dot{\mathbf{h}} = j\omega \mathbf{h}_0 e^{j\omega t}$. The force and moment function is written as $\mathbf{F} = \mathbf{C}\mathbf{q}e^{j\omega t}$, where $\mathbf{q}$ is the flowfield disturbance captured by the aerodynamic equations. $\mathbf{C}$ is a sparse $2 \times N$ matrix that represents the discrete force and moment integration; it is a function of the reduced velocity ($V = U_\infty/\omega_\alpha b\sqrt{\mu}$, where U_∞ is the freestream velocity; ω_α is the pitch natural frequency; b is the airfoil semi-span, and μ is the airfoil–fluid mass ratio). Using a POD-based ROM, suitably trained for pitch and plunge oscillations, the disturbance $\mathbf{q}$ is replaced by a set of reduced-order variables as shown above: $\mathbf{q} = \mathbf{\Phi}\hat{\mathbf{q}}$. In small-disturbance form, (23) becomes

$$\begin{bmatrix} \mathbf{0} & \mathbf{I} \\ \mathbf{K} & \mathbf{0} \end{bmatrix} \begin{bmatrix} \mathbf{h}_0 \\ \dot{\mathbf{h}}_0 \end{bmatrix} + j\omega \begin{bmatrix} -\mathbf{I} & \mathbf{0} \\ \mathbf{0} & \mathbf{M} \end{bmatrix} \begin{bmatrix} \mathbf{h}_0 \\ \dot{\mathbf{h}}_0 \end{bmatrix} = \begin{bmatrix} \mathbf{0} \\ \mathbf{C}\mathbf{\Phi}\hat{\mathbf{q}} \end{bmatrix}. \quad (24)$$

Pitch and plunge variables are linked to the aerodynamic disturbance problem by defining a sparse $N \times 2$ transformation matrix $\tilde{\mathbf{B}}$ such that $\tilde{\mathbf{b}} \equiv \tilde{\mathbf{B}}\mathbf{h}$. Thus, (22) becomes $\hat{\mathbf{A}}\hat{\mathbf{q}} - j\omega\mathbf{\Phi}^H\tilde{\mathbf{B}}\mathbf{h} = \mathbf{0}$, leading to a coupled set of $M + 4$ equations:

$$\begin{bmatrix} \hat{\mathbf{A}} & \mathbf{0} & \mathbf{0} \\ \mathbf{0} & \mathbf{0} & \mathbf{I} \\ -\mathbf{C}\mathbf{\Phi} & \mathbf{K} & \mathbf{0} \end{bmatrix} \begin{bmatrix} \hat{\mathbf{q}} \\ \mathbf{h}_0 \\ \dot{\mathbf{h}}_0 \end{bmatrix}$$
$$+ j\omega \begin{bmatrix} \mathbf{0} & -\mathbf{\Phi}^H\tilde{\mathbf{B}} & \mathbf{0} \\ \mathbf{0} & -\mathbf{I} & \mathbf{0} \\ \mathbf{0} & \mathbf{0} & \mathbf{M} \end{bmatrix} \begin{bmatrix} \hat{\mathbf{q}} \\ \mathbf{h}_0 \\ \dot{\mathbf{h}}_0 \end{bmatrix} = \mathbf{0}. \quad (25)$$

Eq. (25) represents a complex, general eigenvalue problem (for $\beta = j\omega$) of small size that can be used to compute the stability properties of the aeroelastic system with great efficiency. For a given airfoil configuration, the flutter speed can be bracketed by systematically varying reduced velocity as a parameter until the eigenvalue with largest real part changes sign. This approach can be contrasted with the direct approach of Morton and Beran [98–100], which has been successfully applied to the prediction of airfoil flutter speeds in the transonic regime. Their direct method does not reduce the number of DOFs in the solution array and amounts to an implicit analysis of the eigensystem $\beta\mathbf{q} = \mathbf{J}\mathbf{q}$, which is expanded to include the structural equations. However, the method does search for a single, conjugate pair of eigenvectors that becomes neutrally stable, and with this restriction, allows flutter speeds to be predicted at a computational rate comparable to that of solving the nonlinear equations for the static base solution. As will be further reported in the Results section, the POD-based approach extends nicely into three dimensions [101], while much additional work in this direction is required for the direct approach.

2.2.4. Nonlinear ROM formulation with subspace projection

The linear POD formulation described above provides a practical means for assessing the linear stability and dynamics of complex, aeroelastic systems at a very small fraction of the computational cost of full-system analysis. In cases where the dynamics are nonlinear, or in which a ROM of the nonlinear static behavior is desired, a different class of methods is required. One approach suitable to nonlinear problems is the subspace projection technique [51,52].

Eq. (15) is projected onto the subspace of reduced-order variables through a weighted-residual approach [102]. The dynamic residual, $\boldsymbol{R}$, is defined as

$$\boldsymbol{R} \equiv \frac{\mathrm{d}\mathbf{w}}{\mathrm{d}t} - \mathbf{R}(\mathbf{w}; \lambda),$$

which, when forced to vanish after weighting by each of the M modes, yields

$$\mathbf{\Phi}^T\left(\frac{\mathrm{d}\mathbf{w}}{\mathrm{d}t} - \mathbf{R}(\mathbf{W}_0 + \mathbf{\Phi}\hat{\mathbf{w}}; \lambda)\right) = \mathbf{0}. \quad (26)$$

With $\mathbf{\Phi}^T\mathbf{\Phi} = \mathbf{I}$, (26) takes a form equivalent to that previously applied by Pettit and Beran [52]:

$$\frac{\mathrm{d}\hat{\mathbf{w}}}{\mathrm{d}t} = \mathbf{\Phi}^T\mathbf{R}(\mathbf{W}_0 + \mathbf{\Phi}\hat{\mathbf{w}}; \lambda). \quad (27)$$

Equilibrium solutions of (27) satisfy the equation

$$\hat{\mathbf{R}} \equiv \mathbf{\Phi}^T\mathbf{R}(\mathbf{W}_0 + \mathbf{\Phi}\hat{\mathbf{w}}; \lambda) = \mathbf{0}. \quad (28)$$

2.2.4.1. Sensitivity analysis. Sensitivities of equilibrium solutions to λ can be very efficiently predicted with POD-based ROMs. Three formulas are relevant: the relationship between full-system and ROM sensitivities, $\mathrm{d}\mathbf{w}/\mathrm{d}\lambda = \mathbf{\Phi}\mathrm{d}\hat{\mathbf{w}}/\mathrm{d}\lambda$, the definition of ROM residuals, $\hat{\mathbf{R}} = \mathbf{\Phi}^T\mathbf{R}$, and a condition on the ROM solution path

$$\mathrm{d}\hat{\mathbf{R}} = \hat{\mathbf{J}}\mathrm{d}\hat{\mathbf{w}} + \frac{\partial\hat{\mathbf{R}}}{\partial\lambda}\mathrm{d}\lambda = 0, \quad (29)$$

$$\frac{\mathrm{d}\hat{\mathbf{w}}}{\mathrm{d}\lambda} = -\hat{\mathbf{J}}^{-1}\frac{\partial\hat{\mathbf{R}}}{\partial\lambda}. \quad (30)$$

From these formulas, it follows that sensitivities satisfy

$$\frac{\mathrm{d}\mathbf{w}}{\mathrm{d}\lambda} = \mathbf{\Phi}\hat{\mathbf{J}}^{-1}\mathbf{\Phi}^T\frac{\partial\mathbf{R}}{\partial\lambda}. \quad (31)$$

The ROM is most beneficial for sensitivity analysis when there are several different parameters on which the system depends. In the procedure above, $\hat{\mathbf{J}}$ can be computed and decomposed once (as true for the steady-state analysis) and then repeatedly used in evaluating the

sensitivity formula (31) for each variable. Following the decomposition of $\hat{\mathbf{J}}$, the primary computational expense in evaluating (31) is calculating $\partial \mathbf{R}/\partial \lambda$, which is variable dependent, but efficiently obtained.

2.2.4.2. Stability analysis. The point at which (27) loses stability to time-oscillatory disturbances is a Hopf bifurcation point. The stability exchange occurs when a complex pair of eigenvalues of $\hat{\mathbf{J}}$ has vanishing real part, while other real components of the eigenvalues of $\hat{\mathbf{J}}$ are negative [51]. For small M, this process can be inexpensively and indirectly tracked through examination of all the eigenvalues of $\hat{\mathbf{J}}$. We define γ such that $\gamma(\lambda)$ is the eigenvalue of $\hat{\mathbf{J}}(\lambda)$ with largest real part; critical points of stability exchange, λ^*, satisfy $\gamma(\lambda^*) = 0$. For practical problems, where M may not be very small, critical points can be directly found in a manner similar to that applied to aeroelastic systems by Beran and Morton [98]. The direct approach involves solving $\gamma = 0$ through Newton's method:

$$\left.\frac{\partial \gamma}{\partial \lambda}\right|_{\lambda=\lambda^v} (\Delta^{v+1}\lambda) = -\gamma(\lambda^v), \tag{32}$$

where the correction $\Delta^{v+1}\lambda$ is typically relaxed with the parameter ω_{hopf}: $\lambda^{v+1} = \lambda^v + \omega_{\text{hopf}}\Delta^{v+1}\lambda$.

2.2.4.3. Implicit, steady ROM solutions. Eq. (28) is a system of M nonlinear equations which can be efficiently solved with the chord method following computation of the Jacobian, $\hat{\mathbf{J}} \equiv \partial \hat{\mathbf{R}}/\partial \hat{\mathbf{w}}$ [51]. With this approach, the Jacobian is numerically computed about a specified state, $\mathbf{w}^0$, and then frozen in the iterative procedure $\hat{\mathbf{J}}(\mathbf{w}^0)(\hat{\mathbf{w}}^{v+1} - \hat{\mathbf{w}}^v) = -\hat{\mathbf{R}}$, where the superscript index denotes iteration. Only $O(M)$ evaluations of $\mathbf{R}$ and $\mathbf{\Phi}\hat{\mathbf{w}}$ are necessary to construct $\hat{\mathbf{J}}$. Chord iterates are continued until $\|\hat{\mathbf{R}}\| < 10^{-3}$ or a lack of convergence is demonstrated.

2.2.4.4. Time accurate, unsteady ROM solutions. Unsteady solutions, $\hat{\mathbf{w}}(t)$, of (27) can be time integrated using either explicit or implicit techniques. Time accurate explicit integration for the reduced-order solver can be accomplished using the first-order accurate, forward Euler, time integration,

$$\hat{\mathbf{w}}^{n+1} = \hat{\mathbf{w}}^n + \Delta t \mathbf{\Phi}^{\mathrm{T}}(\mathbf{R}(\mathbf{W}_0 + \mathbf{\Phi}\hat{\mathbf{w}}^n; \lambda)). \tag{33}$$

Here Δt denotes a global time step which is generally small to preserve stability for the smallest node spacing in the domain, and the superscript denotes time level. This time accurate integration scheme is computationally burdensome due to repeated evaluation of $\mathbf{R}$, however the CFL condition for stability is increased by the subspace projection method [51]. This simple integration scheme has been used to explore the use of POD for a variety of applications [51,54,103].

The chord method can also be used to implicitly obtain time accurate solutions. Consider the implicit time integration function $\mathbf{F}$:

$$\mathbf{F}(\mathbf{w}^{n+1}) \equiv \mathbf{w}^{n+1} - \mathbf{w}^n - \Delta t \mathbf{R}(\mathbf{w}^{n+1}). \tag{34}$$

The value of $\mathbf{w}^{n+1}$ that results in $\mathbf{F}(\mathbf{w}^{n+1}) = \mathbf{0}$ is the solution for the flow field at time $t_n + \Delta t$ from $\mathbf{w}^n$. The Newton iterations to obtain this solution (for subiterate v to $v+1$) at reduced order are shown below:

$$\hat{\mathbf{F}}(\hat{\mathbf{w}}^v) = \mathbf{\Phi}^{\mathrm{T}}\mathbf{F}(\mathbf{w}^v),$$

$$\Delta \hat{\mathbf{w}} = \left[\frac{\mathrm{d}\hat{\mathbf{F}}(\hat{\mathbf{w}})}{\mathrm{d}\hat{\mathbf{w}}}\right]^{-1} \hat{\mathbf{F}}(\hat{\mathbf{w}}^v),$$

$$\hat{\mathbf{w}}^{v+1} = \hat{\mathbf{w}}^v + \Delta \hat{\mathbf{w}},$$

$$\mathbf{w}^{v+1} = \mathbf{W}_0 + \mathbf{\Phi}\hat{\mathbf{w}}^{v+1}.$$

The Jacobian is $\mathbf{I} - \Delta t \hat{\mathbf{J}}(\hat{\mathbf{w}})$ and again, the full-system function call is required for each Newton iteration. Results have recently been presented [104] for integration with a second-order-accurate Crank–Nicolson scheme [105]. In this formulation, the implicit time integration function from (34) is recast in reduced order as follows:

$$\hat{\mathbf{F}}(\hat{\mathbf{w}}^{n+1}) \equiv \hat{\mathbf{w}}^{n+1} - \hat{\mathbf{w}}^n - \frac{\Delta t}{2}(\mathbf{\Phi}^{\mathrm{T}}\mathbf{R}(\mathbf{W}_0 + \mathbf{\Phi}\hat{\mathbf{w}}^n; \lambda)$$
$$+ \mathbf{\Phi}^{\mathrm{T}}\mathbf{R}(\mathbf{W}_0 + \mathbf{\Phi}\hat{\mathbf{w}}^{n+1}; \lambda)) = \mathbf{0}, \tag{35}$$

and the Jacobian is $\mathbf{I} - \Delta t \hat{\mathbf{J}}(\hat{\mathbf{w}})/2$.

At each time step, the nonlinear system in (34) or (35) may again be solved with the chord method. For weakly nonlinear systems, the Jacobian terms can be evaluated once at $t = 0$; with stronger nonlinearities the Jacobian can be periodically updated at additional computational expense.

2.2.5. Nonlinear low-dimensional ROM formulation

While sufficient to demonstrate the adequacy of the POD basis functions for aeroelastic analysis, the subspace projection method does not afford a computational performance benefit on the order of the reductions in DOFs [55,56,91,106–109]. This inefficiency is especially problematic when time accurate calculations are required, which is the case for unsteady aeroelastic analysis.

In a recent work, Lucia and Beran [108] use both Galerkin and direct projection to recast the compressible flow equations in terms of $\hat{\mathbf{w}}$. These projection techniques produce a set of ODEs of the same order as the number of POD basis functions. Both of these techniques are suitable for linear and nonlinear ROM realizations. A summary of the development in Lucia and Beran [108] is given below.

2.2.5.1. Orthogonal projections. Consider the evolution equation from (15). The continuous form of (15) is

denoted below:

$$\frac{\partial w}{\partial t} = R(w, \lambda). \tag{36}$$

The set of all functions that are potential outcomes of (36) must have sufficient smoothness such that the spatial derivatives within the operator R are defined. The set of functions that are Lebesgue integrable when taken to the second power meet this condition. Otherwise known as the L^2 functions, this set forms a complete linear space that admits spatial functions with any number of discontinuities (a countably infinite number) [110,111]. The domain $D(R)$ and range $R(R)$ of the operator R from (15) are the subset of L^2 functions that meet the boundary conditions posed to give the problem of interest a unique result.

Operating within L^2 is important, because when coupled with an inner product, L^2 provides a geometric structure that gives meaning to the notion of projection. The inner product provides a measure of "closeness" between two functions, and in L^2 the inner product between two functions $\psi_1(\mathbf{x})$ and $\psi_2(\mathbf{x})$ is defined as follows [110]:

$$\langle \psi_1, \psi_2 \rangle = \int_{\Omega} \psi_1(\mathbf{x})\psi_2(\mathbf{x}) \, d\mathbf{x} \quad \text{for } \psi_1, \psi_2 \in L^2. \tag{37}$$

The $\langle \, , \, \rangle$ operator is an inner product because it has the properties of additivity, homogeneity, symmetry and positive definiteness [110]. L^2 is a Hilbert space when endowed with the inner product from (37) [110].

The geometric structure of the inner product space allows us to introduce the notion of orthogonality. Two functions ψ_1 and ψ_2 within an inner product space are orthogonal when

$$\langle \psi_1, \psi_2 \rangle = 0. \tag{38}$$

This is denoted as $\psi_1(\mathbf{x}) \perp \psi_2(\mathbf{x})$. Two subsets A and B are orthogonal when all the functions within A are orthogonal to all the functions within B. This is denoted $A \perp B$.

2.2.5.2. Galerkin projection. The geometric structure of L^2 provides the means to minimize errors due to the uniqueness of orthogonal projections in Hilbert spaces. The remainder of this discussion assumes the continuum spatial functions have been suitably discretized, and the problem has been projected from L^2 into Euclidean N space (which also forms a Hilbert space when accompanied by a suitable norm). Galerkin projection seeks to minimize error resulting in the use of the modal approximation described earlier in (13). The residual ($\mathbf{E}_r$) is defined using the dynamics in (15) as

$$\mathbf{E}_r \equiv \frac{d\mathbf{w}_M}{dt} - \mathbf{R}(\mathbf{w}_M; \lambda), \tag{39}$$

where $\mathbf{w}_M = \sum_{k=1}^{M} \hat{w}_k \mathbf{e}_k$, and $\mathbf{E}_r$ is identically zero when $\mathbf{w}_M = \mathbf{w}$. Errors are minimized by forcing them to lie

outside of $R(\mathbf{R})$, which for this case means we want $\mathbf{E}_r \in R(\mathbf{R})^{\perp}$. By the definition of orthogonality, the following must be true for any $\mathbf{e}_k \in R(\mathbf{R})$:

$$\langle \mathbf{E}_r, \mathbf{e}_k \rangle = 0. \tag{40}$$

Since every vector $\phi \in R(\mathbf{R})$ can be expressed as a linear combination of the orthogonal basis $\{\mathbf{e}\}$, the requirement $\mathbf{E}_r \in R(\mathbf{R})^{\perp}$ is completely specified by the series of inner products $\langle \mathbf{E}_r, \mathbf{e}_k \rangle = 0$ given below, where $k = 1$ through M.

$$\left\langle \frac{d\mathbf{w}_M}{dt} - \mathbf{R}(\mathbf{w}_M; \lambda), \mathbf{e}_k \right\rangle = \mathbf{0}. \tag{41}$$

Eq. (41) is called Galerkin projection. The inner products map vectors to scalars, including the boundary data. What remains is a system of coupled ODEs describing the dynamics of the modal coefficients $\hat{w}_k$ in time, one for each of the M basis functions.

Since the spatial domain is discrete, the inner product becomes a summation as follows:

$$\langle \psi_1, \psi_2 \rangle \approx \sum_{i=1}^{I} \sum_{j=1}^{J} \psi_1(i,j)\psi_2(i,j)\Delta y(i,j)\Delta x(i,j), \tag{42}$$

where i and j are indices of the discretized mesh (in two space dimensions here). The total number of discrete points is $N = I*J$, and typically $N \gg M$. Once the inner products have been evaluated, time integration of the reduced-order set of ODEs can be accomplished very quickly (order M^2 computations as opposed to order N^2 or more). However, evaluating the inner products is not trivial. Even though integrating (41) numerically using (42) might seem simple enough, the nonlinearities and spatial derivatives in the operator $\mathbf{R}$ complicate matters greatly.

The implementation of Galerkin projection is greatly simplified by assuming incompressibility of the governing equations. Park and Lee have applied Galerkin projection to the reduction of the Navier–Stokes equations in non-conservative form for the two-dimensional flow of an incompressible fluid [45]. They obtain a set of M ODEs for $\hat{\mathbf{w}}$ (for $k = 1, \ldots, M$):

$$\frac{d\hat{w}_k}{dt} = a_k + \sum_{l=1}^{M} \hat{w}_l P_{kl} + \sum_{l=1}^{M} \sum_{m=1}^{M} \hat{w}_l \hat{w}_m Q_{klm}, \tag{43}$$

where a_k, P_{kl}, and Q_{klm} are elements of singly, doubly and triply indexed arrays computed by integrating over terms involving the M retained modes. For example, one term appearing in the expression for Q_{klm} is $\int_{\Omega} \mathbf{e}^k \mathbf{e}^l \frac{\partial \mathbf{e}^m}{\partial x} \, d\Omega$, which is evaluated numerically, since the modes are available in discrete form.

2.2.5.3. Direct projection. Direct projection is an extension of the subspace projection method from (27). When the full-order function evaluation $\mathbf{R}$ is replaced with a

general Taylor series expansion [112]:

$$\mathbf{R}(\mathbf{w}_0 + \Delta\mathbf{w}) = \mathbf{R}(\mathbf{w}_0) + \sum_{i=1}^{N} \Delta w_i \frac{\partial \mathbf{R}}{\partial w_i}(\mathbf{w}_0)$$
$$+ \frac{1}{2} \sum_{i,j=1}^{N} \Delta w_i \Delta w_j \frac{\partial^2 \mathbf{R}}{\partial w_i \partial w_j}(\mathbf{w}_0)$$
$$+ \frac{1}{3!} \sum_{i,j,k=1}^{N} \Delta w_i \Delta w_j \Delta w_k \frac{\partial^3 \mathbf{R}}{\partial w_i \partial w_j \partial w_k}(\mathbf{w}_0)$$
$$+ \text{H.O.T.}, \tag{44}$$

pre-multiplication by $\mathbf{\Phi}^{\mathrm{T}}$ and post-multiplication by $\mathbf{\Phi}$ will produce a set of nonlinear ODEs, with the linear portion in state-space form. The numerical computation of the Jacobians is done with $O(M)$ computations as described earlier for the implicit subspace formulation. If central differences are used, the number of full-order function evaluations to accomplish the projection is $(2M)^p$ where p is the order of the largest derivative term retained in the expansion.

2.2.6. Domain decomposition

Domain decomposition in conjunction with POD was introduced by Lucia [113]. The motivation for this approach was to improve the robustness of the ROM, in the presence of moving shocks. The number of modes required to reproduce a flow field with a stationary shock are few, and they are relatively simple to identify. Identifying modes for flows with moving shocks requires much more data, enough to cover all shock locations expected. Once identified, the number of modes retained to reproduce a moving shock is much greater than the few modes typically suitable for Euler analysis [56,106,107]. Retaining a large number of modes for the entire solution domain to accommodate a moving shock contained within a small subset of the domain is problematic. The low energy modes required to allow shock motion tend to destabilize the ROM by introducing non-physical, high-frequency oscillations outside the shock region. Domain decomposition also affords the opportunity to use a variety of modeling techniques of varying fidelity in distinct spatial regions of a complex fluid problem.

Domain decomposition has been used to separate a fluid problem spatially into regions and isolate the region of the flow experiencing a moving shock wave [56,106,107,113]. This assumed the shock was confined to a spatial region of the flow field that could be reasonably identified. For the regions of the flow field not containing a shock, POD was employed as previously described. The region of the flow field containing the moving shock was approached in two ways. The first approach was using the full-order model. Even though the shocked region of the flow had no reduction in the number of DOFs, the use of POD over

the non-shocked portions of the flow field still provided a significant reduction in the number of DOFs relative to the original problem. The second approach was developing a ROM for the shocked region of the flow field.

Analysis using POD and domain decomposition involves solving several smaller fluid problems that are linked by internal boundaries. The full-system dynamics in (15) are applied to each individual domain section. Internal boundaries are handled with ghost cells, which are filled with the corresponding values from the adjacent domain. Domain overlap is necessary under certain conditions. The domain decomposition approach provides flexibility when choosing the set of snapshots and number of modes used to create the ROM for each section.

Under certain conditions, constraints must be introduced into the reduced-order solver to enforce smoothness on the internal boundary. Constraints are necessary when subspace projection is used, and the domain coupling provided by the use of ghost cells and the full-system dynamics is not sufficient to ensure continuity. Consider the case where the internal boundary between two adjacent regions overlap, such that the outer boundary of one region extrudes beyond the inner boundary of the adjacent region by a few cells. When computing solutions for each individual domain at reduced order, the flow field from both domains should match in the overlapping portion of the flow field. Without this occurrence, a constraint can be included to force the flow field sections to match in the overlap region. A constrained optimization method is developed below, which has been applied to steady, quasi-steady, and unsteady analysis [113].

Consider $\mathbf{w}_{S1}$ and $\mathbf{w}_{S2}$ as solution vectors corresponding to adjacent domains with a shared internal boundary Γ. The domains overlap on the internal boundary, and the sections combine to form the fluid vector

$$\mathbf{w} = \begin{bmatrix} \mathbf{w}_{S1} \\ \mathbf{w}_{S2} \end{bmatrix}. \tag{45}$$

Two constraint options are considered. The first constraint C^1 can be written as

$$C^1(\mathbf{w}) = \sum_{i \in \Gamma} w_{i_{S1}} - w_{i_{S2}} = 0. \tag{46}$$

This option is similar to requiring the mean difference be zero on the boundary, and C^1 approximates the L^1 norm. Notice that the absolute value is not included. This omission weakens the constraint, since negative errors can be cancelled by positive errors of equal magnitude; however, neglecting the absolute value improves computational performance. The implicit solver will use the first and second derivatives of the constraints (look ahead to (54)). When the C^1 constraints are used without the absolute values, the first

and second derivatives are a constant function and zero, respectively, and the Jacobian can be pre-computed prior to solver integration. Pre-computing a Jacobian that is valid for the entire run significantly reduces compute time. If an absolute value is introduced, the first and second derivatives are both functions of the flow variables, and pre-computing the Jacobian is not possible. Instead of using the absolute value on the C^1 constraint, the squared difference is constrained to zero which is written as

$$C^2(\mathbf{w}) = \sum_{i \in \Gamma} (w_{i_{S1}} - w_{i_{S2}})^2 = 0. \qquad (47)$$

This option is similar to requiring the variance to be zero on the boundary, and C^2 approximates the L^2 norm. Like including the absolute value on the C^1 constraint, the use of the C^2 expression provides a much stronger constraint, and the computational load is increased because the first and second derivatives are functions of flow variables. However, the derivative expressions are much simpler with C^2 constraints than the case of absolute value on the C^1 constraints, which is why this formulation is preferred.

For the implicit, time-accurate integration, a functional $\ell(\mathbf{w})$ is defined such that

$$\frac{\mathrm{d}\ell(\mathbf{w})}{\mathrm{d}\mathbf{w}} = \mathbf{F}(\mathbf{w}), \qquad (48)$$

where $\mathbf{F}$ comes from (34). For steady analysis, $\ell(\mathbf{w})$ is defined such that $\mathrm{d}\ell(\mathbf{w})/\mathrm{d}\mathbf{w} = \mathbf{R}$ where $\mathbf{R}$ is the non-linear, spatial operator from the full-system dynamics in (15). In either case, solving for the critical values of $\ell(\mathbf{w})$ is equivalent to solving either $\mathbf{F} = \mathbf{0}$ or $\mathbf{R}(\mathbf{w}) = \mathbf{0}$, i.e. finding the flow solution of interest. Either the C^1 or C^2 constraints are introduced to force the flow field from both sections to match in the overlapping portion of their respective domains. In some cases, a series of constraints is used. The constraints are themselves functionals that produce scalar outcomes. These scalar outcomes tend to zero when the flow variables for the overlapping sections approach equality. For overlapping fluid variables that are not identical, the constraint functionals produce a small scalar residual.

The following development is for a single constraint, $C(\mathbf{w})$. The Lagrange constrained optimization minimizes $\ell(\mathbf{w})$ subject to the constraint through the use of a Lagrange multiplier, λ, introduced as an additional DOF. Note that in this section only, λ is used to refer to the Lagrange multiplier, which is consistent with widely used convention. Everywhere else in this paper, λ is a free parameter as defined in (15). Lagrange-constrained optimization [114] modifies $\ell(\mathbf{w})$ adding the linear constraint to form the function $Q(\mathbf{y})$:

$$Q(\mathbf{y}) = \ell(\mathbf{w}) + \lambda C(\mathbf{w}). \qquad (49)$$

The solution vector is augmented to include λ,

$$\mathbf{y} = \begin{bmatrix} \mathbf{w}_{S1} \\ \mathbf{w}_{S2} \\ \lambda \end{bmatrix} = \begin{bmatrix} \mathbf{w} \\ \lambda \end{bmatrix}. \qquad (50)$$

The critical values of Q are the values of $\mathbf{w}$ and λ such that

$$\mathbf{G}(\mathbf{y}) = \frac{\mathrm{d}Q(\mathbf{y})}{\mathrm{d}\mathbf{y}} = \begin{bmatrix} F(\mathbf{w}) + \lambda \dfrac{\mathrm{d}C(\mathbf{w})}{\mathrm{d}\mathbf{w}} \\ C(\mathbf{w}) \end{bmatrix} = \mathbf{0}. \qquad (51)$$

As long as the constraints are linearly independent, and the fluid problem has a unique solution, the critical value will be the unique minimizing function for Q [114]. The reduced-order mapping includes the Lagrange multiplier:

$$\mathbf{y} = \begin{bmatrix} \boldsymbol{\Phi}_1 & \mathbf{0} & \mathbf{0} \\ \mathbf{0} & \boldsymbol{\Phi}_2 & \mathbf{0} \\ \mathbf{0} & \mathbf{0} & 1 \end{bmatrix} \begin{bmatrix} \hat{\mathbf{w}}_{S1} \\ \hat{\mathbf{w}}_{S2} \\ \lambda \end{bmatrix}, \qquad (52)$$

which is rewritten as

$$\mathbf{y} = \boldsymbol{\Phi}_\lambda \hat{\mathbf{y}}. \qquad (53)$$

Newton iterations are used to solve the reduced-order system for $\hat{\mathbf{y}}$. The flow field is obtained by expanding $\hat{\mathbf{w}}_{S1}$ and $\hat{\mathbf{w}}_{S2}$ with reduced-order mappings for each section, after which λ is discarded. The reduced-order Jacobian comes from the full-order Jacobian

$$\frac{\mathrm{d}\mathbf{G}(\mathbf{y})}{\mathrm{d}\mathbf{y}} = \begin{bmatrix} \dfrac{\mathrm{d}F(\mathbf{w})}{\mathrm{d}\mathbf{w}} + \lambda \dfrac{\mathrm{d}^2 C(\mathbf{w})}{\mathrm{d}\mathbf{w}^2} & \dfrac{\mathrm{d}C(\mathbf{w})}{\mathrm{d}\mathbf{w}} \\ \dfrac{\mathrm{d}C(\mathbf{w})}{\mathrm{d}\mathbf{w}} & \mathbf{0} \end{bmatrix} \qquad (54)$$

$$\frac{\mathrm{d}\hat{\mathbf{G}}(\hat{\mathbf{y}})}{\mathrm{d}\hat{\mathbf{y}}} = \boldsymbol{\Phi}_\lambda^{\mathrm{T}} \frac{\mathrm{d}\mathbf{G}(\mathbf{y})}{\mathrm{d}\mathbf{y}} \boldsymbol{\Phi}_\lambda. \qquad (55)$$

We will summarize results from several analysis employing domain decomposition [56,106,107] later in this paper.

2.2.7. Deforming grids

Grid deformation is used in CFD to model a variety of moving boundary problems such as dynamic interaction between airfoils and flaps and deforming aeroelastic structures. The POD techniques just described do not directly account for grid deformation. In POD, snapshot data of the flow-field are arranged in column (index) form. The order of the data in the column is irrelevant to the process, although the order must be maintained throughout. With a deforming grid, the physical location of any data point changes from one snapshot to the next. If this information is not contained within the POD development, the transformation from index space to physical space produces errors.

Anttonen extensively studied the impact of grid deformation on POD [115]. To treat grid deformation with POD, Anttonen developed an algorithm that

successfully accounted for grid deformation in ROMs formed using subspace projection. In this algorithm, snapshots of the grid were taken along with the snapshots of the solution during the training process. These "training grids" were then compared to the grids in the full-order solver as the ROM was time integrated. The relative differences were compared, and this comparison allowed error measurement between the ROM and the full-order solution.

In Anttonen et al. [116], the authors used several ROMs trained for various sets of grid deformation. To determine the timing for the transition of one ROM to another, a metric was developed to determine if a ROM was applied to grids which differed significantly from the training condition. To evaluate the match between the training condition and actual grid motion during time integration, a grid modal matrix was created from the grid snapshots. Snapshot matrices of the x and y locations for the deforming grid were stored during the training process. The snapshots were based on the perturbation from a default grid to highlight the relative deformation. The grid snapshot matrices were used to create a grid modal matrix, $\mathbf{\Phi}_G$. In the same fashion these matrices were used to create the POD modal matrix $\mathbf{\Phi}$ in (13). The grid modal matrix represented the range of grid deflections during training. Grid snapshots were taken at the same points in time as the fluid snapshots. An error term was as developed using $\mathbf{\Phi}_G$, where $\mathbf{\Phi}_G$ was related to modal amplitude vectors $\hat{\mathbf{x}}$ and $\hat{\mathbf{y}}$ as follows:

$$\begin{bmatrix} \mathbf{x} \\ \mathbf{y} \end{bmatrix} \approx \mathbf{\Phi}_G \begin{bmatrix} \hat{\mathbf{x}} \\ \hat{\mathbf{y}} \end{bmatrix}. \tag{56}$$

Here $\mathbf{x}$ and $\mathbf{y}$ were arrays of the x and y coordinates of the actual grid deformation during the time integration of the ROM. The vectors $\hat{\mathbf{x}}$ and $\hat{\mathbf{y}}$ were computed using the inverse of $\mathbf{\Phi}_G$, which is $\mathbf{\Phi}_G^{\mathrm{T}}$ when the columns of $\mathbf{\Phi}_G$ are orthonormal vectors:

$$\begin{bmatrix} \hat{\mathbf{x}} \\ \hat{\mathbf{y}} \end{bmatrix} = \mathbf{\Phi}_G^{\mathrm{T}} \begin{bmatrix} \mathbf{x} \\ \mathbf{y} \end{bmatrix}. \tag{57}$$

Finally, the error vector $\mathbf{Err}_{x,y}$ of the difference between the training condition and the current grid was determined by first projecting the grid coordinates into the training condition using $\mathbf{\Phi}_G^{\mathrm{T}}$. The vectors $\hat{\mathbf{x}}$ and $\hat{\mathbf{y}}$ were expanded back into full-order form using $\mathbf{\Phi}_G$, and this result was subtracted from the exact grid coordinates $\mathbf{x}$ and $\mathbf{y}$:

$$\mathbf{Err}_{x,y} = \begin{bmatrix} \mathbf{x} \\ \mathbf{y} \end{bmatrix} - \mathbf{\Phi}_G \mathbf{\Phi}_G^{\mathrm{T}} \begin{bmatrix} \mathbf{x} \\ \mathbf{y} \end{bmatrix}. \tag{58}$$

Notice that the product $\mathbf{\Phi}_G \mathbf{\Phi}_G^{\mathrm{T}}$ represents the projection of the current grid coordinates onto the space of grid deformations experienced during ROM training. If the grid coordinates $\mathbf{x}$ and $\mathbf{y}$ are not significantly affected by $\mathbf{\Phi}_G \mathbf{\Phi}_G^{\mathrm{T}}$, then the error approaches $\mathbf{0}$. In other words, the vectors $\mathbf{x}$ and $\mathbf{y}$ must lie within (or close to) the nullspace of $\mathbf{I} - \mathbf{\Phi}_G \mathbf{\Phi}_G^{\mathrm{T}}$.

To calibrate the algorithm, Anttonen et al. created a ROM at one set of grid deformations and time integrated this ROM using a second set of grid deformations. The actual flow parameters were identical for both runs to control errors caused solely by grid deformation. The error of the ROM was compared to the full-order result, and any errors were due to the misalignment of the modes to the grid point locations. By comparing the relative grid error and the ROM error, the correlation between the errors was determined. An acceptable level of error was selected and a corresponding threshold of grid error established. Once the grid error was correlated to the ROM error, the grid error was used as a threshold indicator for accuracy. When the grid error exceeded a certain threshold, the ROM was replaced.

This method relies on the repeated function calls to the full-order model afforded by the subspace projection technique described in Section 2.2.4. The full-order function call provides the updated grid deformation values $\mathbf{x}$ and $\mathbf{y}$ for the grid metric evaluation. Additional research in this area is required for extending grid deformation into low-order ROM realizations obtained via Galerkin projection, direct projection, or Volterra methods.

2.2.8. Balanced POD

We conclude our overview of POD with a brief discussion of balanced model reduction. For this discussion, we will summarize the work of Willcox and Peraire [117]. The concept of balanced reduction for state-space models was introduced by Moore [118]. The basic idea was to utilize information from both the inputs and outputs of a dynamical system. This utilization was done by examining both the primal and dual formulations of the dynamical system to ensure proper scaling of the reduced-order states. The resulting algorithm used the controllability and observability grammians in the formulation of the POD basis functions. These grammian matrices are related to the correlation matrix used to generate the POD basis vectors [119]. Wilcox and Peraire devised a concept to produce a balanced realization without requiring the construction of the full-order, approximate grammians, which is computationally extensive for CFD applications.

The balanced algorithm is summarized as follows:

(1) Use the method of snapshots to obtain POD modes for the primal system.
(2) Use the method of snapshots to obtain POD modes for the dual system.
(3) Formulate low-rank approximations for the controllability and observability grammians.

(4) Obtain the modes of the product of both grammians to determine the balanced transformation.
(5) Retain only the balanced modes that correspond to large Hankel singular values.

This approach was demonstrated on a 2-D plunging airfoil problem [117]. The ROM was formed using the frequency domain technique described in Section 2.2.3. The benefit of the balanced POD was improved robustness to changes in parameters, and improved accuracy with fewer overall DOFs relative to a ROM trained without the balanced formulation. The drawback of the technique was the need for a high-fidelity simulation for the dual problem, which was not as readily available as the CFD codes for the primal system. Even so, there may be future POD applications where the dual solver is easily obtained, and in these cases, the use of balanced model-reduction is warranted.

2.3. Nonlinear dynamics with HB

In addition to Volterra and POD, the HB formulation of Hall et al. [60] is another prevalent approach with many successful applications to fluid dynamics problems. HB was first applied to the computation of time-periodic, nonlinear, viscous flows in 2-D turbomachinery cascades and is now being used to analyze the aeroelastic behavior of airfoils in transonic flow [77]. The goal of the HB method is the efficient computation of time-periodic solutions of large, nonlinear systems. Current methods based on time integration, for example those applied to aeroelastic computations [120,121], can be very demanding, owing to the need for retention of time accuracy. The requirement for small, global time steps and accurate integration over numerous cycles increases computational cost over steady-state analysis, for which large, local time steps can be used. With the HB method, the governing equations can be recast in a steady-state form that accounts for the underlying time periodicity of the solution and that can be solved with pseudo-time-integration using standard acceleration techniques (local time stepping and multigrid acceleration).

2.3.1. HB development

There are several techniques, including HB the finite-difference method, the shooting method, and the Poincaré map method, that have been applied to a large number of relatively low-order problems involving nonlinear oscillations. These techniques are described in numerous texts and papers (and the references within) [122–125]. The method of multiple scales has also been applied to the simulation of LCO for an airfoil/flap configuration in transonic flow [126].

However, the HB method developed by Hall et al. is designed to treat nonlinear, aerodynamic problems of practical size for which there are large shock motions [60]. To describe this technique, we choose $\mathbf{w}$ to be a discretized field variable with N DOFs satisfying $\mathbf{w}(t) = \mathbf{w}(t + T)$, where T is the period of the oscillation. The solution is expanded in a Fourier series in time, truncated to $2N_{\mathrm{HB}} + 1$ terms:

$$\mathbf{w}(t) = \sum_{n=-N_{\mathrm{HB}}}^{N_{\mathrm{HB}}} \mathbf{w}^n \mathrm{e}^{j\omega n t}. \tag{59}$$

The term $n = 0$ corresponds to the mean flow. Expansion (59) can be substituted into the governing equation (15) to obtain $2N_{\mathrm{HB}} + 1$ equations for the vector coefficients in the Fourier expansion, $\mathbf{w}^n$, by collecting terms of like frequency. Using the nomenclature of Hall et al., these equations are written as $\tilde{\mathbf{S}}(\tilde{\mathbf{w}}) = \tilde{\mathbf{R}}(\tilde{\mathbf{w}}; \lambda)$, where, in the unsteady term, $\tilde{\mathbf{S}}$ represents a collocation of the Fourier coefficients:

$$\tilde{\mathbf{S}} = j\omega\tilde{\mathbf{N}}\tilde{\mathbf{w}}. \tag{60}$$

$\tilde{\mathbf{R}}$ is a collection of nonlinear terms arising from the residual array, $\mathbf{R}$. $\tilde{\mathbf{N}}$ is a diagonal matrix containing the harmonic indices $(-N_{\mathrm{HB}}, \ldots, 0, \ldots, N_{\mathrm{HB}})$, and $\tilde{\mathbf{w}}$ is the set of vector coefficients:

$$\tilde{\mathbf{w}} = (\mathbf{w}^{-N_{\mathrm{HB}}}, \ldots, \mathbf{w}^0, \ldots, \mathbf{w}^{N_{\mathrm{HB}}})^{\mathrm{T}}. \tag{61}$$

The evaluation of $\tilde{\mathbf{R}}$, which Hall et al. calls the harmonic fluxes, is computationally expensive $(O(NN_{\mathrm{HB}}^3))$ for the Euler equations and not easily extended to turbulent, viscous flow [60]. They propose an alternative HB formulation that is both simpler and more efficient. First, $\mathbf{w}$ is defined at $2N_{\mathrm{HB}} + 1$ instants in time, evenly distributed about the periodic orbit, and collected into a single array $\mathbf{w}^*$:

$$\mathbf{w}^* = \left(\mathbf{w}(0), \mathbf{w}\left(\frac{T}{2N_{\mathrm{HB}} + 1}\right), \ldots, \mathbf{w}\left(\frac{2N_{\mathrm{HB}}T}{2N_{\mathrm{HB}} + 1}\right)\right).$$

Then, the discrete Fourier transform operator, $\tilde{\mathbf{E}}$, which is an $NN_{\mathrm{HB}} \times NN_{\mathrm{HB}}$ blocked matrix, is used to relate $\mathbf{w}^*$ and $\tilde{\mathbf{w}}$ according to $\tilde{\mathbf{w}} = \tilde{\mathbf{E}}\mathbf{w}^*$. Substitution of this expression into the equation $\tilde{\mathbf{S}} = j\omega\tilde{\mathbf{N}}\tilde{\mathbf{w}} = \tilde{\mathbf{R}}$ provides

$$j\omega\tilde{\mathbf{E}}^{-1}\tilde{\mathbf{N}}\tilde{\mathbf{E}}\mathbf{w}^* = \mathbf{R}^*, \tag{62}$$

where $\mathbf{R}^*$ is the residual array evaluated at the $2N_{\mathrm{HB}} + 1$ temporal points. The right-hand side of (62) reduces to a simple form. Since the governing equations are in strong-conservation form, the product $\tilde{\mathbf{E}}^{-1}\tilde{\mathbf{E}} = \tilde{\mathbf{I}}$ can be formed through the linear derivative expressions in $\mathbf{R}$.

Finally, Hall et al. introduce a pseudo-time τ[60] by which (62) is integrated towards "steady state":

$$\frac{\partial\mathbf{w}^*}{\partial\tau} + j\omega\tilde{\mathbf{E}}^{-1}\tilde{\mathbf{N}}\tilde{\mathbf{E}}\mathbf{w}^* = \mathbf{R}^*(\mathbf{w}^*; \lambda). \tag{63}$$

This step is an important benefit of the HB method, because it allows the time-dependent solution to be computed with existing, accelerated steady-state methods that need far fewer iterations than time-accurate,

time-integration methods. In this formulation, the "unsteady" term is replaced by $j\omega\tilde{\mathbf{E}}^{-1}\tilde{\mathbf{N}}\tilde{\mathbf{E}}\mathbf{w}^*$, requiring $\mathbf{O}(NN_{\text{HB}}^2)$ operations to evaluate (e.g., the multiplication of $\tilde{\mathbf{E}}\mathbf{w}^*$), an improvement over the HB method in fully spectral form. Furthermore, Hall et al. [60] report that the evaluation of the fluxes, $\mathbf{R}^*$, which requires $\mathbf{O}(NN_{\text{HB}})$ operations using standard techniques, dominates the cost of the numerical scheme.

We comment that the HB technique does not involve a reduction in the number of variables arising from spatial discretization and does not provide a model that is a compact representation of the full system. However, this technique does yield an efficient and low-order representation of the temporal variations of complex systems experiencing cyclic behavior in time. Also, a form of this HB method that allows the period T to be explicitly treated as an unknown (i.e., for an autonomous system) is currently being developed by Hall and his colleagues.

2.3.2. Adaptive HB

The work of Maple et al. [79] introduces the notion of adaptive HB as a modification to the original HB approach of Hall et al. Adaptive HB involves two complimentary innovations: a split-operator method [80] and dynamic frequency allocation [81].

2.3.2.1. Split-operator method.
In Maple et al. [80], the authors developed the split-operator method for the 1-D inviscid Burger's equation. The authors observed that the HB source term $\mathbf{R}^*(\mathbf{w}^*; \lambda)$ from (62) reduced the stability limit of MacCormack's scheme such that a CFL $\leqslant 0.6$ was required. To improve the stability limit of the system, a second discretization scheme incorporating a split-operator approach was implemented.

The split-operator approach was first used in CFD to improve the convergence rates problems in finite-rate chemistry [127]. For Burger's equation, Maple et al. [80] implemented the approach by dividing the inhomogeneous problem into a homogeneous PDE and a homogeneous ODE. These two equations were solved alternately using appropriate, possibly different, techniques until the steady-state solution was reached. The split HB form of Burger's equation is given by

$$\frac{\partial \mathbf{w}^*}{\partial \tau} + \frac{\partial \mathbf{F}^*}{\partial x} = 0, \tag{64a}$$

$$\frac{\partial \mathbf{w}^*}{\partial \tau} = -\hat{\mathbf{S}}, \tag{64b}$$

For this effort, the homogeneous PDE, (64a), was solved with a standard, explicit MacCormack scheme. The homogeneous ODE, (64b), was solved using a three stage Runge–Kutta integration. With this approach, the time-step restriction observed in the original implementation was removed.

2.3.2.2. Dynamic frequency allocation.
Just as some regions in a flow field may require more cells or grid points to adequately capture the flow physics, some regions also require more frequencies in a HB solution. Analogous to grid adaptation, which adjusts the number of grid points in a region to better resolve the flow, the adaptive HB approach automatically adjusts the number of Fourier frequencies included in the solution to resolve the flow at a given cell on a cell-by-cell basis.

The HB solution is begun with a user-specified initial number of frequencies. As the solution develops, frequencies are added in fixed increments to individual grid cells until a final frequency distribution and solution are obtained. Such an approach requires a reliable indicator of solution fidelity at each computational cell. Since the final time-response of the flow is not known a priori, the indicator must rely only on the current (and possibly past) state of the solution. A reliable indicator is the fraction of spectral energy contained in the highest computed Fourier frequency, given by

$$\mathbf{E}_N = \frac{|\mathbf{w}^{N_{\text{HB}}}|^2}{\sum_{n=0}^{N_{\text{HB}}} |\mathbf{w}^n|^2}, \tag{65}$$

where all mathematical operations are performed element-wise, so that $\mathbf{E}_N$ contains the fraction of spectral energy of the highest computed frequency for each variable expanded in a series ($\rho, \rho u$, etc.). For the flow fields of interest, discontinuities in the time response are localized and do not take the form of pure impulses, so $\mathbf{E}_N$ decreases as N is made larger. The use of $\mathbf{E}_N$ as an adaptation metric is dependent on this property.

The decision to augment frequencies at a cell is made by comparing each element of $\mathbf{E}_N$ to a threshold value, $\mathbf{E}_{\text{thresh}}$. Because $\mathbf{E}_N$ tends to mirror the spatially oscillatory nature of the high-frequency coefficients, it is smoothed with an unweighted 5-point spatial average prior to thresholding. When any element of the smoothed $\mathbf{E}_N$ exceeds the threshold, additional frequencies are incorporated into the solution at that cell. Selection of the threshold value is based on the desired solution fidelity.

Once a cell is identified for augmentation, its frequency content is increased by a predetermined increment, chosen to minimize execution time. The time required to solve the split-domain HB equations is composed mainly of two components—the time required to solve the time-domain equations (see (63)) and the time required to perform the necessary Fourier transforms.

According to Maple, the frequency augmentation approach is most efficient when initiated with solutions that are representative of the final solution. If adaptation is attempted too early in the solution process, unnecessary frequencies could be added based on transient flow structures that are not present in the final

solution. On the other hand, if the solution is allowed to develop too long before adaptation is attempted, too much time could be spent refining flow details that change when the solution is adapted, resulting in increased execution times. Therefore, adaptation should occur soon after the major flow features are developed.

In Maple et al. [81], the authors employ two adaptation triggers. The primary trigger was based on a measure of the flow development, as given by a modified L_2 norm of the change in the solution during one iteration. Adaptation was triggered when the trigger value dropped by a user-specified amount. In the rare cases where convergence stalls and the specified residual drop was not achieved, a secondary trigger, which was based on the number of iterations completed, initiated adaptation.

Discretization of (64a) requires the addition and subtraction of the vector $\mathbf{w}^*$ (and the flux expression) within a discretization stencil. This requirement presents a problem for cells in the discretization stencil that have different sample rates (numbers of frequencies). Not only do the vectors have different lengths, but the elements correspond to the state of the flow at different points in time. Cell quantities must be resampled so that the sample rate is consistent across the discretization stencil.

Frequency-domain truncation/zero-padding was selected as the primary resampling method due to the superior quality of the solution at sample rate transitions [81]. To achieve a smooth solution at frequency transitions, it was necessary to resample the transition boundaries at every solver integration stage. Attempts to time-lag the transitions by freezing the resampled values at the first integration stage resulted in discontinuities at the transition cell, even when both sides of the transition had the same number of frequencies and no interpolation was required. Results from the application of adaptive HB will be presented in Section 5.2.

2.4. Hybrid POD and Volterra

The last technique to be described in this review is the hybrid POD and Volterra approach introduced by Lucia and Beran [91,109]. This technique extends the application of Volterra theory to reduced-order modeling of compressible flows by considering the modal response of global fluid modes obtained through POD. Volterra theory, as described earlier in this paper, has been used with good success to characterize GAFs for structural dynamics applications [128] but had not been successfully applied to a flow field. In structural systems, the traditional Volterra approach can be applied to scalar modal amplitudes to provide a small set of time signals for systems realization. POD provides an analogous approach for fluid flows. In the hybrid method, GAFs are replaced with global fluid modes, which are

identified with POD, and systems realization theory is used to identify the modal responses from numerical data. The numerical data is the response of the fluid flow to the impulse excitation of one or more forcing terms. The fluid response at each sampled time is projected onto the POD basis functions to obtain the time history of the modal amplitudes. The resulting data is used to synthesize a very low-order state-space model, which can be integrated quickly to obtain time histories of the modal amplitudes. The entire flow-field can be reconstructed from the modal amplitudes for any time of interest, which is the primary advantage of the hybrid approach.

2.4.1. Motivation

The goal of the Volterra-POD approach was to explore a ROM synthesis method that could achieve computational savings on the order of DOF reductions obtained with POD for nonlinear flow-fields. This goal was achieved in the initial application [91], where four orders of magnitude reduction was obtained in both DOFs and compute time. To date, the hybrid Volterra-POD method has only been applied to flow-fields characterized by linear behavior. The product of the technique was a linear, state-space system of ODEs governing the dynamics of modal coefficients corresponding to a small number of POD basis functions. The state-space realization was obtained from a set of impulse responses that were processed using ERA (see Section 2.1.3).

The applicability of POD basis functions to nonlinear problems has been documented in the literature, but a tractable nonlinear, low-order model realization procedure is a key missing link. Two techniques, Galerkin projection and direct projection, were previously described as having potential for obtaining nonlinear terms [108]. However, the linear portion of these realization procedures is generally unstable, requiring dissipation techniques that affect model performance. The Volterra-POD approach provides a stable reduced-order equation set and is an important advance toward achieving stable, nonlinear ROMs.

2.4.2. Aeroelastic ROM development

The aeroelastic ROM development from Lucia et al. [109] is summarized below. Since the development involves representations for both fluid and structural dynamics, some notation needs to be clarified. The full-order vector of fluid variables $\mathbf{w}$ from (15) represents the spatially discretized flow field. POD provides a transformation $\mathbf{\Phi}$ that maps $\mathbf{w}$ to a low-order vector of modal coefficients $\hat{\mathbf{w}}$ (from (13)). The reduced-order fluid variable $\hat{\mathbf{w}}$ will be denoted $\mathbf{Y}_f$, which will be the vector of outputs $\mathbf{y}[n]$ in the state-space model from (6). Likewise, a nonlinear structural model $\dot{\mathbf{w}}_s = \mathbf{R}_s(\mathbf{w}_s, \mathbf{P}; \lambda)$ is necessary, and for this development,

$\mathbf{w}_s$ is a vector of scalar amplitudes modifying a set of structural modes as in Beran et al. [55]. The pressure term $\mathbf{P}$ couples the dynamics models at the fluid–structure interface, and the structural variable $\mathbf{w}_s$ will be denoted $\mathbf{Y}_s$.

A state-space model for $\mathbf{Y}_f$ can be obtained from impulse responses using the ERA method. Impulses for the fluid system use the structural variable ($\mathbf{Y}_s$) as the forcing terms. Each structural term is impulsed, and the fluid system response is generated using the full-order model. The time history of the impulse response is projected onto each of the POD basis functions to obtain the impulse response of the reduced-order fluid vector $\mathbf{Y}_f$. POD basis functions are obtained using the method of snapshots as described previously. The process is repeated for each structural mode, and the collection of impulse responses is used to generate a linear state-space model for the reduced-order fluid system:

$$\dot{\mathbf{X}}_f = \mathbf{A}\mathbf{X}_f + \mathbf{B}\mathbf{Y}_s, \tag{66a}$$

$$\mathbf{Y}_f = \mathbf{C}\mathbf{X}_f, \tag{66b}$$

where $\mathbf{X}_f$ is the state vector from the ROM realization, and $\mathbf{Y}_s$ represents the modal coefficients for the structural deformation. The continuum form of (6) is readily obtained from the discrete form given the time step size Δt used in the ERA realization.

The structural model is coupled to the reduced-order fluid model (66a) and (66b) through the projected pressure term $\mathbf{P}$. The reduced-order variables, $\mathbf{Y}_s$, are obtained from the dynamic states $\mathbf{X}_f$ by the linear mapping $\mathbf{C}$. Fluid pressure on the panel is extracted from $\mathbf{Y}_s$ using the portion of the reduced-order mapping $\boldsymbol{\Phi}$ that pertains to the moving boundary. The mapping of reduced-order fluid states to projected pressure is denoted $\mathbf{f}_P$:

$$\mathbf{P} = \mathbf{f}_P(\mathbf{X}_f). \tag{67}$$

Eq. (67) is used to couple the structure and fluid dynamic state variables,

$$\dot{\mathbf{Y}}_s = R_s(Y_s, \mathbf{f}_P(\mathbf{X}_f); \lambda). \tag{68}$$

Eqs. (66a) and (68) comprise the low order, aeroelastic ROM with linear fluid dynamics and nonlinear structural dynamics.

The fluid and structural terms are grouped into arrays $\mathbf{Y}$ and $\hat{\mathbf{R}}$ as follows:

$$\mathbf{Y} = \begin{bmatrix} \mathbf{X}_f \\ \mathbf{Y}_s \end{bmatrix}, \tag{69}$$

$$\hat{\mathbf{R}} = \begin{bmatrix} \mathbf{A}\mathbf{X}_f + \mathbf{B}\mathbf{Y}_s \\ \mathbf{R}_s(\mathbf{Y}_s, \mathbf{f}_P(\mathbf{X}_f); \lambda) \end{bmatrix}. \tag{70}$$

The reduced-order, aeroelastic system is denoted as

$$\dot{\mathbf{Y}} = \hat{\mathbf{R}}(\mathbf{Y}). \tag{71}$$

2.4.3. Time integration of the aeroelastic system

The aeroelastic ROM in (71) can be efficiently integrated in time with the two-time level, second-order accurate, Crank–Nicolson method:

$$\frac{\mathbf{Y}^{n+1} - \mathbf{Y}^n}{\Delta t} = \frac{1}{2}(\hat{\mathbf{R}}^{n+1} + \hat{\mathbf{R}}^n), \tag{72}$$

$$\boldsymbol{R} \equiv \mathbf{Y}^{n+1} - \frac{\Delta t}{2}\hat{\mathbf{R}}^{n+1} - \mathbf{Y}^n - \frac{\Delta t}{2}\hat{\mathbf{R}}^n = \mathbf{0}. \tag{73}$$

At each time level, $\boldsymbol{Y} \equiv \mathbf{Y}^{n+1}$ is computed from (73) using a chord technique with a time-frozen Jacobian

$$\left(\mathbf{I} - \frac{\Delta t}{2}\hat{\mathbf{J}}_o\right)(\boldsymbol{Y}^{v+1} - \boldsymbol{Y}^v) = -\boldsymbol{R}(\boldsymbol{Y}^v), \tag{74}$$

where v is a subiteration index, and $\hat{\mathbf{J}}_o$ is the Jacobian of the reduced-order aeroelastic system evaluated for the base flow condition and $\mathbf{Y}_s = \mathbf{0}$. A suitable number of subiterations are computed at each time step to obtain a good approximation to $\mathbf{Y}^{n+1}$. Prior to subiteration, Y is predicted from the explicit formula

$$\boldsymbol{Y} = \mathbf{Y}^n + \Delta t \hat{\mathbf{R}}^n. \tag{75}$$

3. Volterra results

In this section, we present results obtained with the Volterra theory of nonlinear systems. The results presented encompass both 2-D and 3-D analysis and include ROM synthesis from data collected analytically and experimentally from wind tunnel results.

3.1. Volterra analysis of an RAE airfoil in transonic plunge

First- and second-order kernels for the Navier–Stokes solution (with Spalart–Allmaras turbulence model) of an RAE airfoil in plunge at a transonic Mach number using the CFL3D code [129] are presented in Fig. 1. On the left are two sets of first-order kernels due to two different sets of excitation amplitudes. Recall that the first-order kernel is computed using (3) and is the result of two pulse responses, one at a particular amplitude and the second at double the first amplitude. One of the first-order kernels shown in Fig. 1 was computed using excitation plunge amplitudes of $w = 0.01$ and 0.02, where w is a percent of the chord of the airfoil. The other first-order kernel was computed using excitation plunge amplitudes of $w = 0.1$ and 0.2. It is clear that the two kernels are not linearly related, which demonstrates how the first-order kernel can capture amplitude-dependent nonlinear effects. On the right of Fig. 1 are
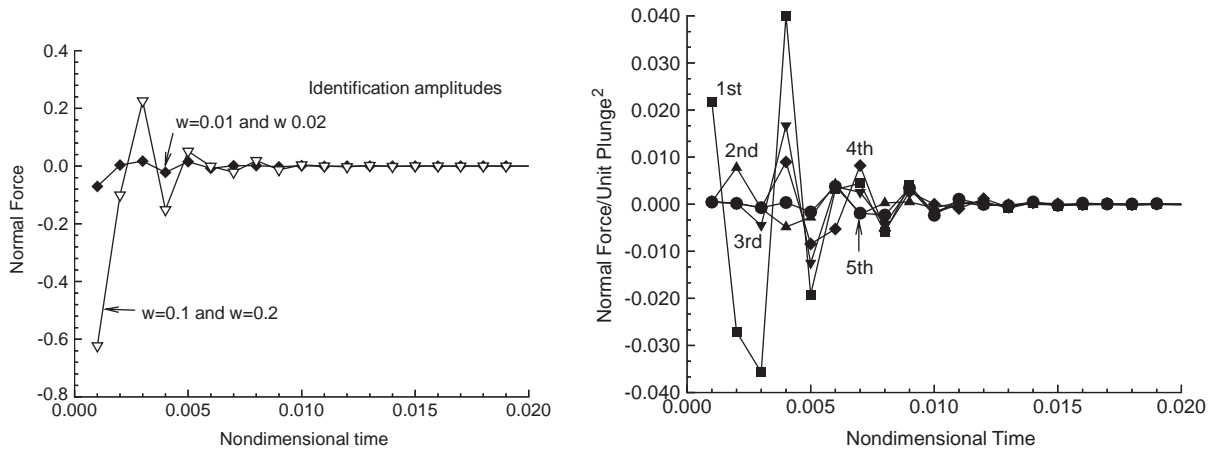
Fig. 1. Volterra kernels for CFD analysis of RAE airfoil. Left: first-order kernel and effect of ID amplitudes. Right: first five components of the second-order kernel for plunge.
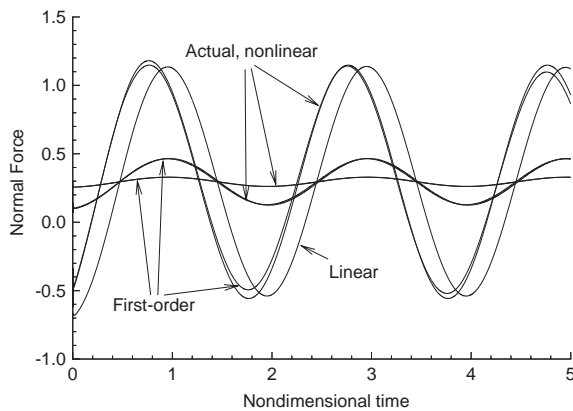

Fig. 2. Comparison of actual nonlinear and first-order Volterra responses for three different plunge motions and a linear response for the largest motion.

five components of the second-order kernel for this case. The second-order kernel is more complicated because it is a two-dimensional function of time. The important point is that this kernel is readily generated, and its relatively smaller values (compared with the first-order kernel) and its rapid convergence indicate a small level of nonlinearity present. This information might be used to determine that the first-order kernel may be sufficient to capture the dominant nonlinear effects. This point is demonstrated in Fig. 2.

Fig. 2 is a comparison of plunge responses for three different plunge amplitudes for the same configuration. Specifically, a comparison is made between the full CFD solution due to a sinusoidal plunging motion, and that comparison is obtained using the first-order kernel from Fig. 1 (due to the larger excitation amplitudes). As can be seen, the plunge response obtained using the Volterra first-order kernel compares identically with the response

obtained from the full CFD solution for the two smaller amplitude responses. The comparison for the largest amplitude response (i.e., nonlinear) is very good as well, with a slight but noticeable difference between the two results. The nonlinearity of the large-amplitude plunge responses is confirmed by a simple linear scaling of the smallest amplitude (i.e. linear) response, which, as shown in Fig. 2, cannot capture the amplitude-dependent nonlinear plunge dynamics seen at the larger amplitude. The turnaround time ("wallclock") for the full CFD solution was on the order of a day, whereas the Volterra first-order solution was computed on a workstation in 30 s using digital convolution. The initial cost of computing the first-order kernel was trivial as well, due to the rapid convergence of the pulse responses. In fact, since each pulse (unit and double amplitudes) goes to zero in less than 100 time steps, the responses were generated using a debugging mode option available on the supercomputer system used. Using this option, computations requiring less than 300 time steps are executed immediately, intended for debugging purposes. As a result, each pulse was computed within 5 min, resulting in a first-order kernel that was computed in about ten minutes. Of course, once the kernel has been computed, it can be used to predict the response to an arbitrary input (steady, any and all frequencies, random) of arbitrary length via digital convolution on a workstation. Using this method, there is no need for the repeated, and costly, execution of the CFD code for different inputs.

3.2. Volterra analysis of an AGARD 445.6 wing

Raveh et al. [14] have applied the Volterra-based ROM approach to analysis of the AGARD 445.6 wing. They simulate the flow field around the wing using the EZNSS/Euler/Navier–Stokes code [130]. This code

provides a choice between two implicit algorithms, the Beam-Warming algorithm and the partially flux-vector splitting algorithm of Steger et al. Grid generation and inter-grid connectivity are handled using the Chimera approach. The code was enhanced with an elastic capability to compute trimmed maneuvers of elastic aircraft [130]. For the CFD computations, the flow field around the wing was evaluated on a C-H type grid with 193 points in the chordwise direction along the wing and its wake, 65 grid points in the spanwise direction, and 41 grid points along the normal direction.

As discussed previously, a process of mode-by-mode excitation was performed for this wing using four elastic modes at a Mach number of 0.96. The mode-by-mode excitation technique provides the unsteady aerodynamic response in all four modes, due to an excitation of one of the modes. In this fashion, a matrix of four-by-four functions (16 total) is developed. Two sets of excitation inputs were used: the discrete-time pulse input and the discrete-time step input. The cost of computing these functions is minimal, due to the rapid convergence of these functions, and it consists of only four code executions. Once these functions were defined, several full CFD solutions were generated that were due to various sinusoidal inputs at various frequencies. Shown in Fig. 3 is just one of these results for a 5 Hz input frequency, which compares the result obtained from the full CFD solution to that obtained via convolution of the step or pulse responses with a 5 Hz sinusoid. As can be seen, the comparison is exact to plotting accuracy for most of the responses. The full CFD solution, consisting of 8000 iterations required approximately 24 h on an SGI Origin 2000 computer with four processors (CPUs). By comparison, the Volterra-based ROM response shown required about a minute. Even including the upfront cost of computing the pulse (or step responses), the computational cost savings are significant. More importantly, the same pulse (or step) functions can now be used to predict the response of the aeroelastic system to any arbitrary input of any length.

Shown in the left and middle portions of Fig. 4 is a comparison of linear and nonlinear GAFs for the first two modes of the AGARD 445.6 Aeroelastic Wing at a Mach number of 0.96. Nonlinear GAFs refers to the GAFs computed using the Volterra pulse-response technique about a nonlinear steady-state value by exciting one mode at a time and obtaining the resultant responses in the other modes. The CFD results are compared with those using the ZAERO code for a purely linear case. Frequency-domain values were obtained by performing a convolution of several frequencies of interest with the computed CFD-based pulse responses. As can be seen, the comparison is reasonable and shows
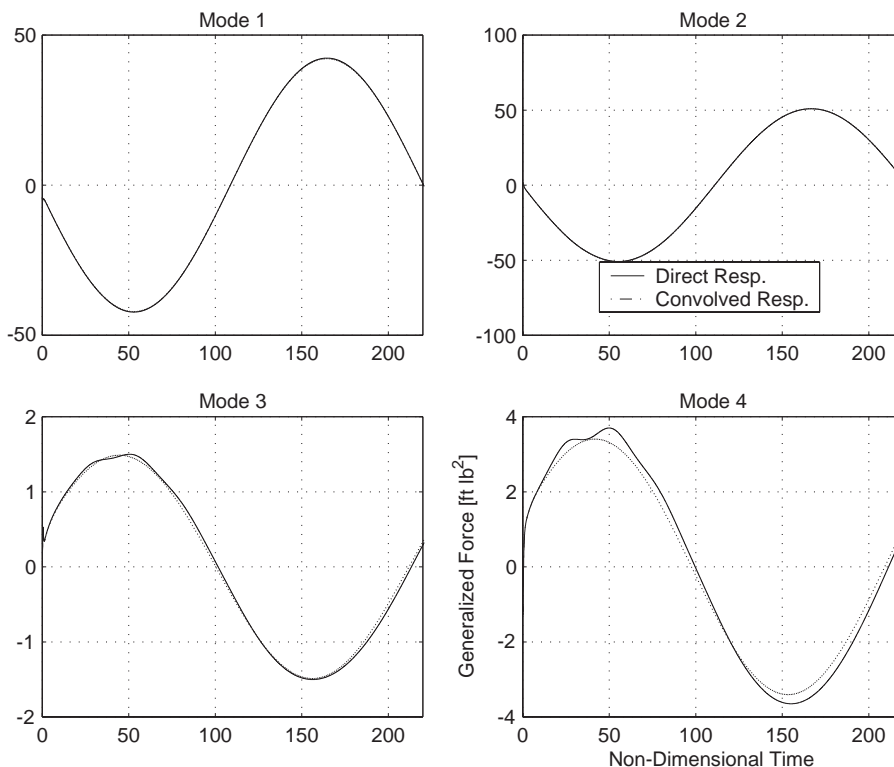
Fig. 3. Comparison of direct and convolved responses to sinusoidal excitation at 5 Hz (Mach 0.96).
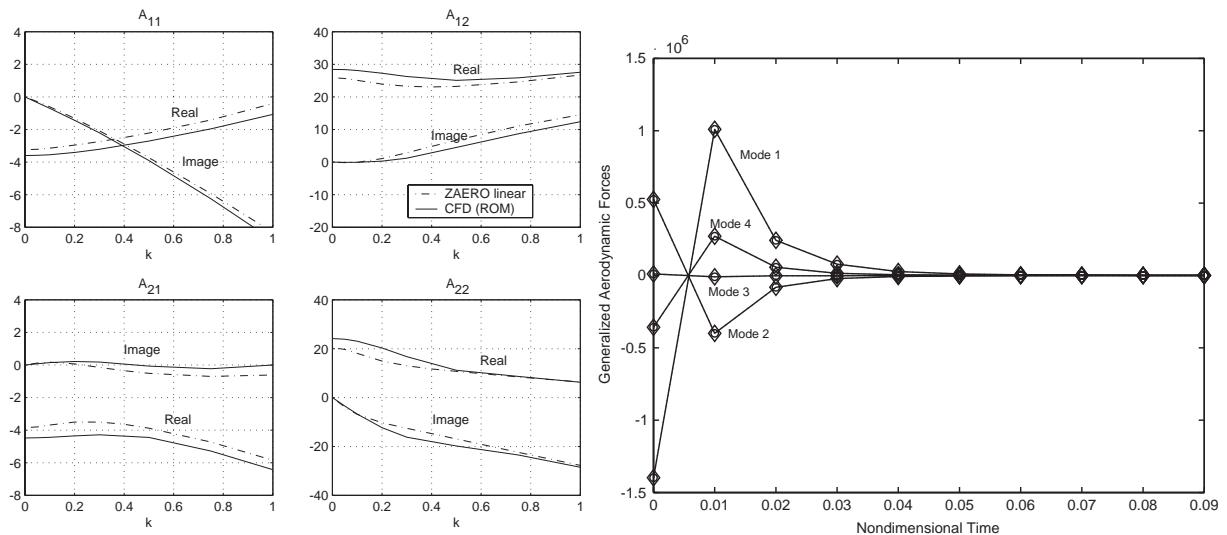
Fig. 4. Volterra results for the AGARD 445.6 wing at Mach 0.96. Left and middle: comparison of linear and nonlinear GAFs for the first two wing modes. Right: comparison of pulse responses.

the small (but not negligible) nonlinear aerodynamic effects identified using the Volterra pulse-response technique.

Rather than transforming the time-domain GAFs into the frequency domain, discrete-time, state-space systems can be created using the Volterra pulse responses directly [15]. Presented in the right portion of Fig. 4 is a comparison of the pulse responses for the AGARD 445.6 Aeroelastic Wing due to a unit pulse in the first mode. The CFD-based pulses (circles) compare exactly with the pulse responses obtained from a state-space system generated to model this system. The 32nd-order state-space system is a complete representation of the entire frequency spectrum of the unsteady aerodynamics defined by the GAF influence functions for the four aeroelastic modes of this wing. Due to unit pulses in the second, third, and fourth mode, the pulse responses are just as good as those shown in Fig. 4 but are not presented here for brevity.

Silva et al. took this research one step further by using ERA to synthesize a linear state-space ROM from the GAF impulse responses for the AGARD 445.6 wing [128]. For this work, Silva et al. used CFL3Dv6 to compute the impulse responses for each mode of the aeroelastic system. The GAF impulse responses were input into the ERA method (see Section 2.1.3), and a 196th order state-space model was generated as the aerodynamics ROM. Coupling the state-space model of the unsteady aerodynamic system with a state-space model of the structure within MATLAB/SIMULINK results in the state-space aeroelastic system shown in Fig. 5. The aeroelastic response of the system is a function of the initial conditions of the structure and the dynamic pressure.
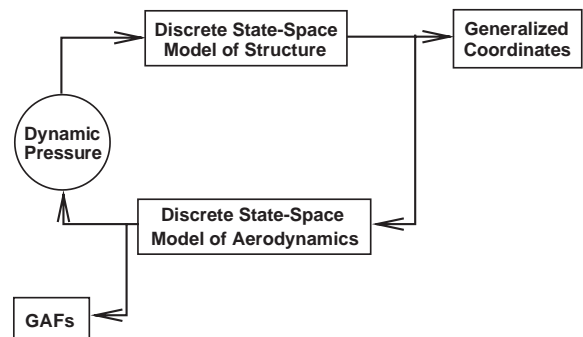
Fig. 5. SIMULINK model of the aeroelastic system.

In order to validate this state-space aeroelastic system, simulations were performed at various dynamic pressures. The generalized coordinate time histories and the corresponding generalized coordinate FFTs at zero dynamic pressure (wind-off) are shown in Fig. 6. The zero dynamic pressure attenuates all aerodynamic effects, leaving only structural effects. With zero structural damping, the response consists of simple harmonic motion of the uncoupled vibration modes in the time domain and frequency spikes of the uncoupled vibration modes: 9.60, 38.2, 48.35, and 91.54 Hz in the frequency domain.

At a dynamic pressure of 50 psf, as in Fig. 7, the effect of aerodynamic damping is evident in the decaying response of the generalized coordinate time histories. The associated modal frequency spikes at this condition are no longer uncoupled as they were in Fig. 6.

Finally, at a dynamic pressure of 75 psf, as in Fig. 8, flutter is evident. A close-up of this aeroelastic transient is presented as Fig. 9. The ROM results compare
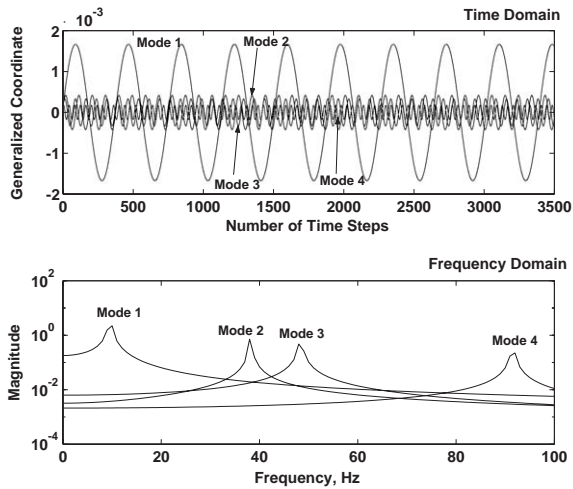
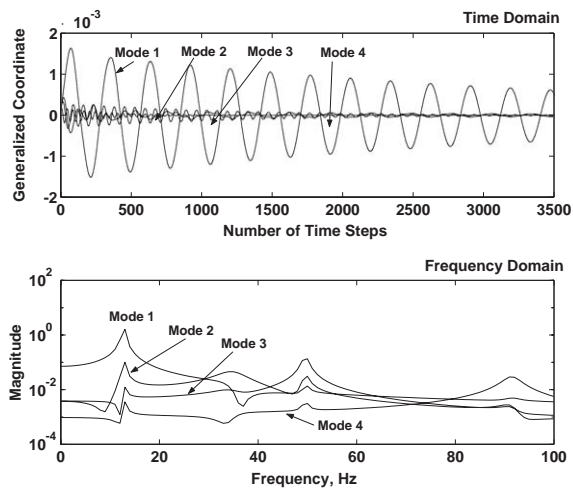Fig. 6. Aeroelastic response of the state-space aeroelastic system at $M = 0.9$ and $Q = 0$ psf.

Fig. 7. Aeroelastic transients in terms of generalized coordinates for the state-space system at $M = 0.9$, $Q = 50$ psf, and $g = 0.0$.
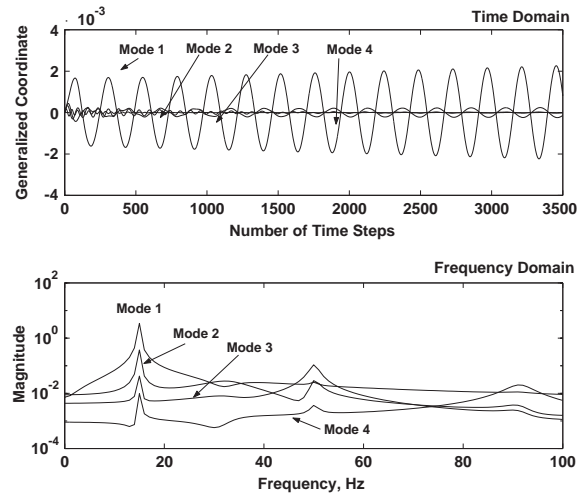

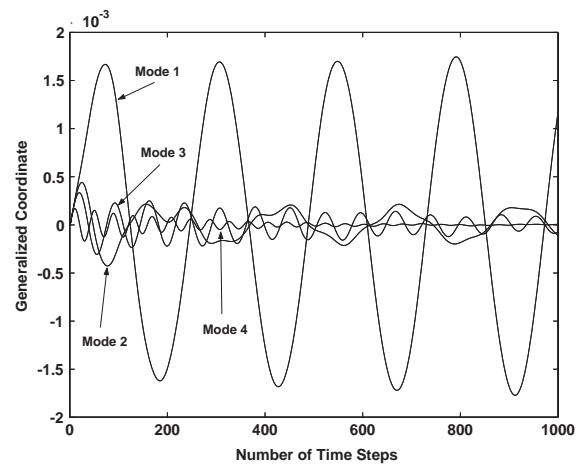Fig. 8. Aeroelastic transients in terms of generalized coordinates for the state-space system at $M = 0.9$, $Q = 75$ psf, and $g = 0.0$.

Fig. 9. Close-up of the aeroelastic transients for the state-space system at $M = 0.9$, $Q = 75$ psf, and $g = 0.0$.

identically with results using CFL3Dv6 directly at all dynamic pressures investigated.

These aeroelastic transients are computed in seconds within MATLAB/SIMULINK, thus allowing a larger number of cycles to be computed for improved frequency resolution. In addition, if parametric variations that involve the structure are desired (structural damping, updated frequencies, etc), the analyses can be performed using this approach since the unsteady aerodynamic system is unaffected by these variations.

These results validate the ROM methodology presented and are examples of a new and powerful tool available to the aeroelastician. Most importantly, the

state-space models developed are suitable for use within a multidisciplinary design environment. Beyond the AGARD wing case, the Volterra method has been extended to swept wings and supersonic wings [131–133]. As a result of these early successes, the Volterra approach is growing more widespread and gaining favor with aeroelasticians.

3.3. Synthesis of Volterra ROMs from experimental data

Silva et al. [134,135] have recently computed aerodynamic impulse responses using experimental data, showing that accurate ROMs could be synthesized independent of CFD tools. Silva et al. demonstrated the experimental technique using two wind-tunnel

models: a Rigid Semispan Model (RSM) (see Fig. 10) and a Benchmark Supercritical Wing (BSCW) (see Fig. 11). The method was used to successfully predict the pressure responses due to various sinusoidal oscilla-
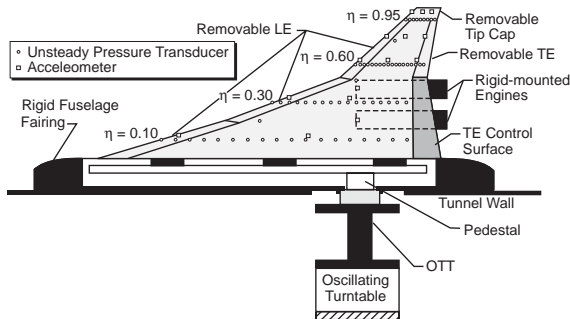
Fig. 10. Planform, model details, and instrumentation layout for the RSM wind-tunnel model.
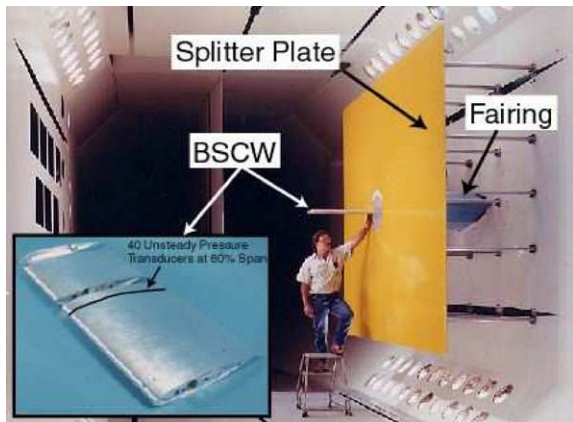
Fig. 11. The BSCW wind-tunnel model.

tions for both wind-tunnel models. Results for the RSM are summarized here.

The step pitch input commanded to the wind tunnel model and the resultant pressure response at a single pressure transducer location are shown in Fig. 12. Although a theoretical step input consists of an infinite slope where the step occurs, a physically realizable step input will be limited by the pitch inertia, stress, and load limitations of the model undergoing pitch. As can be seen, a step input that closely approaches a theoretical step input can be applied by an experimental device. The unsteady pressure measurement is also quite noisy.

Using the sequence of step pitch motions of the oscillating turn table (OTT) as the input and the unsteady pressure measurement as the output, deconvolution is applied to identify the unsteady aerodynamic impulse response. The time- and frequency-domain versions of the pressure impulse response, identified via deconvolution, are shown in Fig. 13. As seen in Fig. 13, the identified impulse response exhibits significant frequency content, as is to be expected for an impulse response. An analysis of the unsteady aerodynamic impulse responses at all pressure transducer locations can provide a spatial mapping of the frequency characteristics of a given configuration at a given test condition. This type of spatial mapping may be useful for the design and optimal placement of various flow control devices.

Upon identification, the unsteady aerodynamic impulse response can then be used to predict the unsteady aerodynamic response due to any OTT input using convolution and the impulse response of Fig. 13. The comparison between the measured pressure response and the corresponding predicted pressure response for a commanded oscillation of 1.2 Hz is presented in Fig. 14. The comparison is excellent and demonstrates the ability
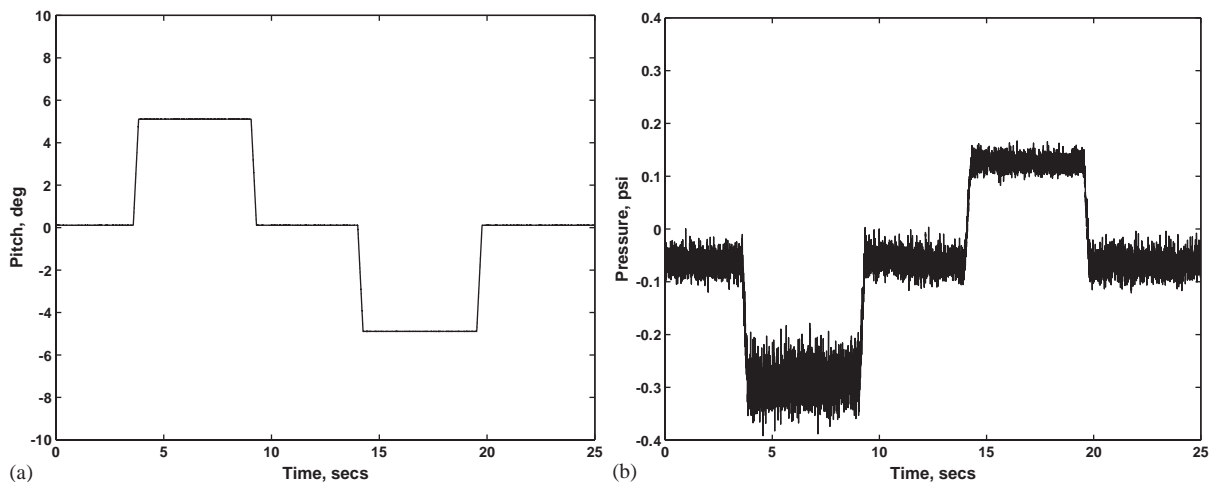
Fig. 12. Commanded pitch motion and resultant pressure response on the upper surface of the RSM at 60% span and 30% chord at $M = 0.8$, $q = 150$ psf. (a) Step input in pitch and (b) pressure response due to step input in pitch.
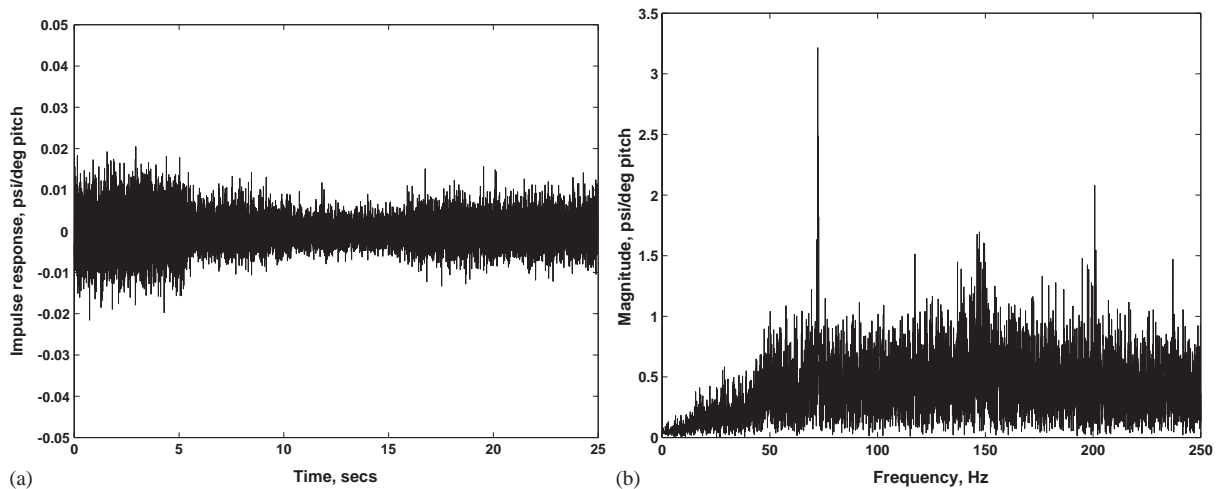
Fig. 13. Pressure impulse response obtained via deconvolution for the RSM; time domain and frequency domain (magnitude). (a) Time domain and (b) frequency domain.
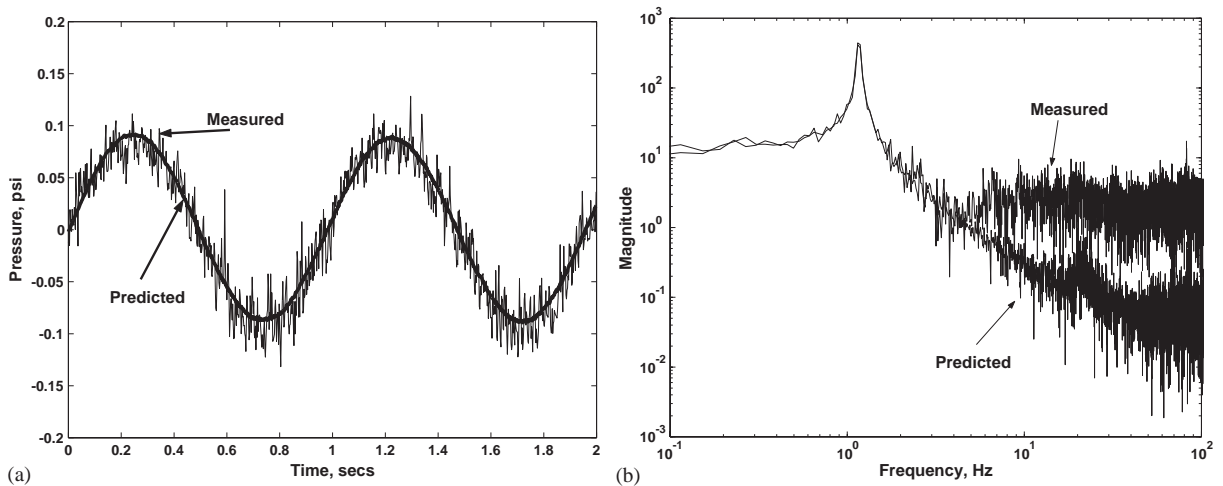

Fig. 14. Measured and predicted pressure responses due to a 1.2 Hz sinusoidal motion of the OTT for the RSM; time domain and frequency domain (magnitude). (a) Time domain and (b) frequency domain.

of the method to capture the dominant (driving) frequency while filtering out uncorrelated noise. The deconvolution process automatically identifies the input/output correlations, which results in the impulse response.

The process of identifying these correlations for a given input/output pair also has the added benefit that it filters out any information that is not correlated to the input. Therefore, uncorrelated measurement noise, for example, is automatically removed as the impulse response is generated. This filtering capability is visible in Fig. 14. The method can be used to (1) identify the level of linearity for a given measurement and (2) filter out the noise from experimental measurements.

Additional analysis are required to (1) further investigate the value of spatial frequency mappings for a given configuration and (2) use the information provided by this method to gain insight into the dominant flow physics. These results represent the first time that experimental unsteady aerodynamic impulse responses have been successfully identified.

Finally, Hajj and Silva [136] used this methodology to identify the nonlinear aspects that lead to the flutter of a high speed civil transport (HSCT) flexible semispan model. A hierarchy of spectral moments was used to determine the characteristics of the aerodynamic loading and structural strains and motions. Nonlinear analysis of the pressure fluctuations under transonic conditions

showed that the aerodynamic forces acting on the model had nonlinearly coupled frequency components. The results showed how nonlinear analysis tools could be used to identify nonlinear aspects of the flutter phenomenon for potential validation of nonlinear computational tools.

4. POD results

The POD has been applied to a variety of multi-disciplinary problems involving the aerodynamic equations. In this section, we summarize recent findings arising from the reduction of system order through POD-based modeling. We first review application of the frequency-domain POD to aeroelastic systems in two and three space dimensions and then describe progress in the analysis of nonlinear equation sets with POD, including those that exhibit LCO and moving shocks.

4.1. Prediction of flutter boundaries using linear (frequency domain) POD analysis

Hall et al. [50] report an application of their linear POD formulation (see Section 2.2.3) to a two-dimensional aeroelastic configuration, and in an ongoing study, Thomas et al. [101] extend this previous work to the analysis of three-dimensional wings. In 2-D, Hall et al. develop POD-based ROMs for the NASA Ames Research Center NACA 64A010 airfoil with a pitch and plunge structural model representative of a swept-wing section [137]. Base solutions of the Euler equations, W_0, are computed with a node-centered Lax–Wendroff scheme for freestream Mach numbers, M_∞, between 0.7 and 1.0. A shock first becomes evident in the base flow solution near the airfoil crest at about Mach 0.8. The aero-dynamic equations are solved on grids of O topology; solution insensitivity to grid refinement is verified using a sequence of grids involving 65×33, 97×49 and 129×65 nodes.

ROMs of the flow equations are constructed from solution snapshots resulting from two independent airfoil movements about base states: pitch oscillation and plunge oscillation. Using the procedure detailed in the Analysis section, snapshots are computed from (21) for reduced frequencies (nondimensionalized by freestream velocity and airfoil chord) evenly distributed between -1 and 1. Following collection of 41 snapshots, Hall et al. assemble ROMs with up to 41 retained modes [50]. A ROM is computed for each different Mach number (and base flow) examined. The aerodynamic equations in reduced-order form are then coupled with the structural equations, leading to the low-order, aeroelastic eigenproblem (25).

Hall et al. [50] carry out very efficient analyses of (25) to construct flutter boundaries for the thickened NACA 64A010 airfoil. Their results are summarized in Fig. 15. Flutter speeds predicted with POD-based ROMs compare well with those previously reported from transonic small-disturbance analyses [137–139] and are used to document precisely the fold in the flutter boundary characteristic of the NACA 64A010 airfoil. As observed by Hall et al., the Mach number at which the fold occurs is under predicted by the small-disturbance analyses relative to the POD-based Euler analysis [50]. Fig. 15 also illustrates that the POD results are well converged in the number of grid points used in the CFD computations and the number of modes retained in the ROM. The results obtained with either the coarsest grid or the fewest number of retained modes deviate from the remaining results for only a small set of Mach numbers. In particular, the highly nonlinear behavior around Mach 0.9 is well defined in most cases.

In Thomas et al. [101], the authors have extended the linear POD formulation to the analysis of the (weakened) AGARD 445.6 wing. Their investigation addresses two potential concerns for the application of POD-based methods to practical aeroelastic configurations: the size of ROMs necessary to capture 3-D effects and the sampling requirements associated with a multiplicity of configuration-dependent structural modes. Thomas et al. compute base flow solutions of the Euler equations with a grid of O-O topology containing $49 \times 33 \times 33$ nodes and construct flutter boundaries through POD analysis for Mach numbers between 0.5 and 1.141. They develop POD-based ROMs using two approaches. First, a 55-mode POD is built at each Mach number by computing solutions of (21) at reduced frequencies evenly distributed between 0 and 0.5 (conjugate solutions are associated with negative frequencies) for the first five natural modes of the wing structure. With this surprisingly small number of POD modes, Thomas et al. obtain results that are very consistent with those published by Lee-Rausch and Batina [140] in terms of flutter speed and frequency ratio. Thomas et al. also propose and demonstrate a promising technique for reducing the number of snapshots necessary to construct an effective POD-based ROM for an aeroelastic configuration. With this approach, only two snapshots are required for each natural mode of the structure in addition to a set of "fundamental" modes to construct the aeroelastic ROM.

4.2. POD applied to turbomachinery

Internal flows in turbomachinery represent another important application for ROM methods. Modeling the flow physics in the rotor–stator interaction is important for designing high-efficiency, reliable compressors and turbines. Potential flow interaction, wake interaction, hot streak interaction, vortex shedding, and blade flutter are all important phenomena present in the rotor–stator
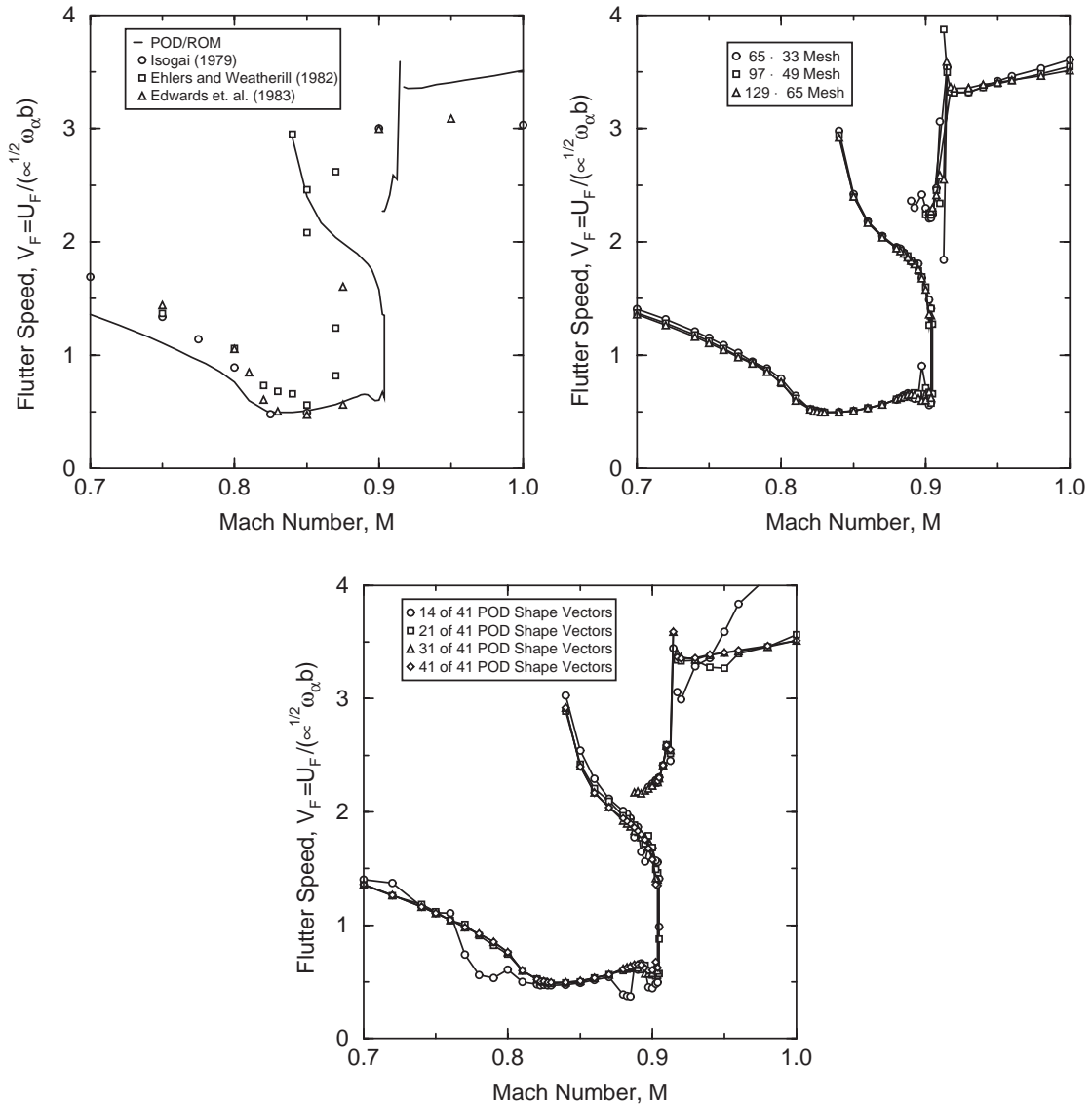
Fig. 15. Flutter speed of NASA Ames Research Center NACA 64A010 air-foil for various Mach numbers computed with frequency domain, POD-based ROMs. Left: results from, 41-mode ROM (finest grid) versus other computational results; middle: sensitivity of 41-mode ROM to grid refinement; right: sensitivity of POD results (finest grid) to number of retained modes (from Hall et al. [50] with permission).

interaction. The interaction between these phenomena makes the simulation challenging and requires a large computational effort. In addition, the large number of geometric and flow parameters makes it expensive to include the numerical simulation of rotor–stator interaction in the turbomachinery design system.

In one body of work in this area, Epureanu et al. [141–143] applied the frequency domain POD technique from Section 2.2.3 to compressor cascades. In Epureanu et al. [141], the authors assessed the influence of far-field upstream Mach number on the performance of the

ROMs. For this work, the full potential equation was linearized about a steady, nonuniform flow and a small perturbation model was formed. Unsteadiness was introduced by forcing small pitch-oscillations about the mid-chord portion of the airfoil. Results were obtained for subsonic Mach numbers of 0.50, 0.55, 0.70 and a transonic condition of 0.80. The subsonic airfoil response was accurately modelled using 10 DOFs, while 35 DOFs were required to precisely recreate the flow dynamics. For the transonic case, 15 DOFs were required to provide the same accuracy in modelling the

airfoil response, and 50 DOFs were required for the flow dynamics. Mach number influenced ROM accuracy indirectly, since the Mach number used for POD training dictated the applicability of the POD modes.

In another work, Cizmas and Palacios [144] used POD to model the unsteady compressible flow through a multistage axial compressor or turbine with arbitrary blade counts. For this effort, POD was applied to the Reynolds-averaged Navier–Stokes equations. The flow was modeled as quasi-three-dimensional and assumed to be fully turbulent. The ROM was formed using the nonlinear subspace projection method from Section 2.2.4.

The analysis reported ROM results for the energy variable, e. Results were also presented for density and skin friction coefficient. The turbine used for the numerical simulation had 32 stator airfoils and 48 rotor airfoils. The radius at mid-span was approximately 1 m. The solidity of the stator row was 0.93, and the solidity of the rotor row was 0.91. The flow conditions for the test turbine were subsonic, with inlet Mach number of 0.155, Reynolds number 65,799, inlet temperature 869 K, exit to inlet pressure ratio of 0.68, and rotational speed 3600 rotations/min.

The spatio-temporal variation of energy, e, in the stator is shown in Fig. 16. The non-dimensional energy varied between approximately 2.25 and 3.41. The time-averaged energy varied from 2.27 to 3.39. For POD development, a snapshot of the solution was saved every 10 time steps, while the blade passing period was divided into 3000 time steps. Consequently, 300 snapshots were saved over a blade passing period.

The POD reconstruction of energy in the stator and rotor rows at time $t = 0$ is shown in Fig. 17.
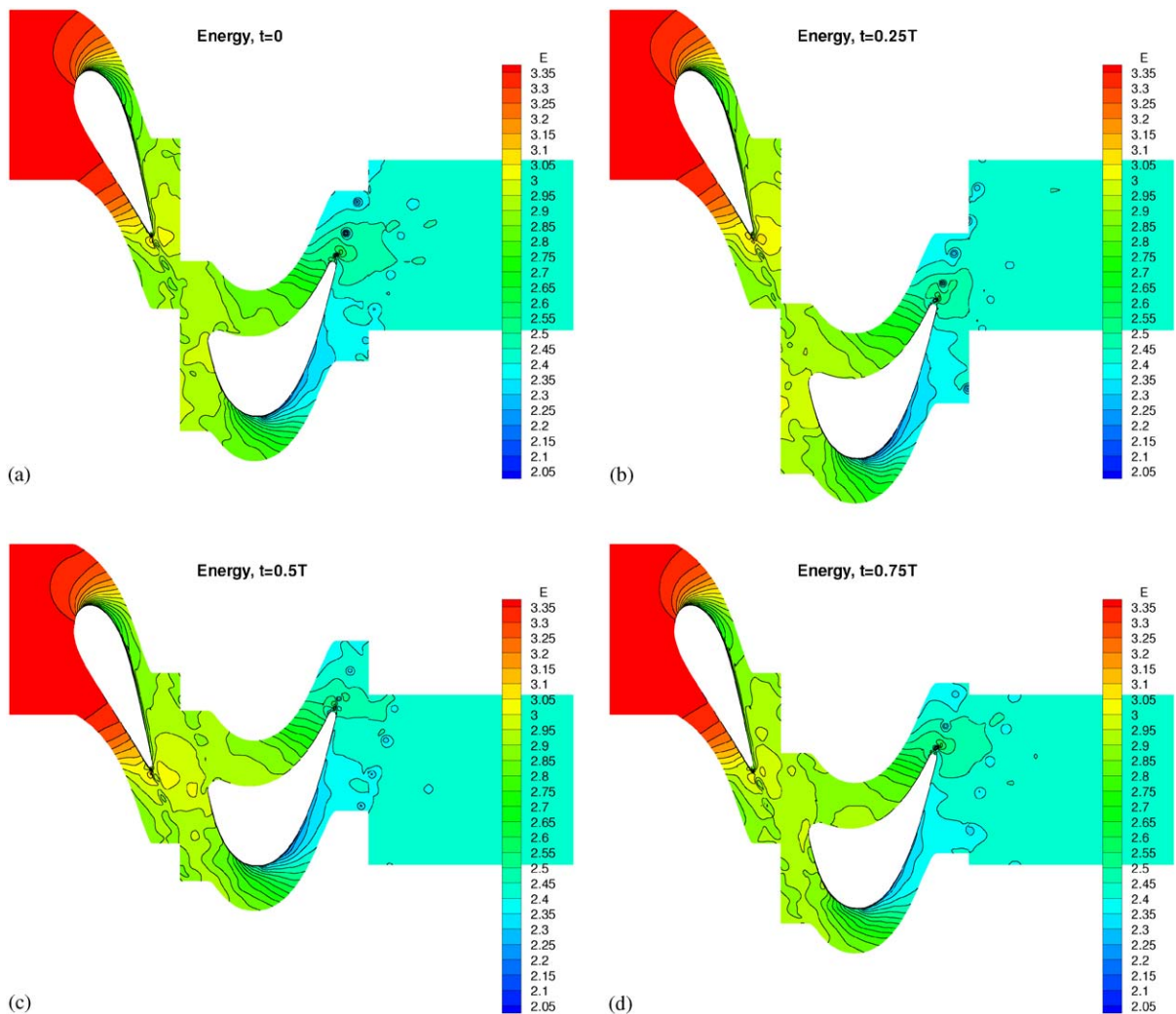
Fig. 16. Spatio-temporal variations of state variable e recorded at equal time intervals during one period T of the flow motion (from Cizmas and Palacios [144] with permission). (a) $t = 0$ (b) $t = 0.25T$ (c) $t = 0.5T$ (d) $t = 0.75T$.
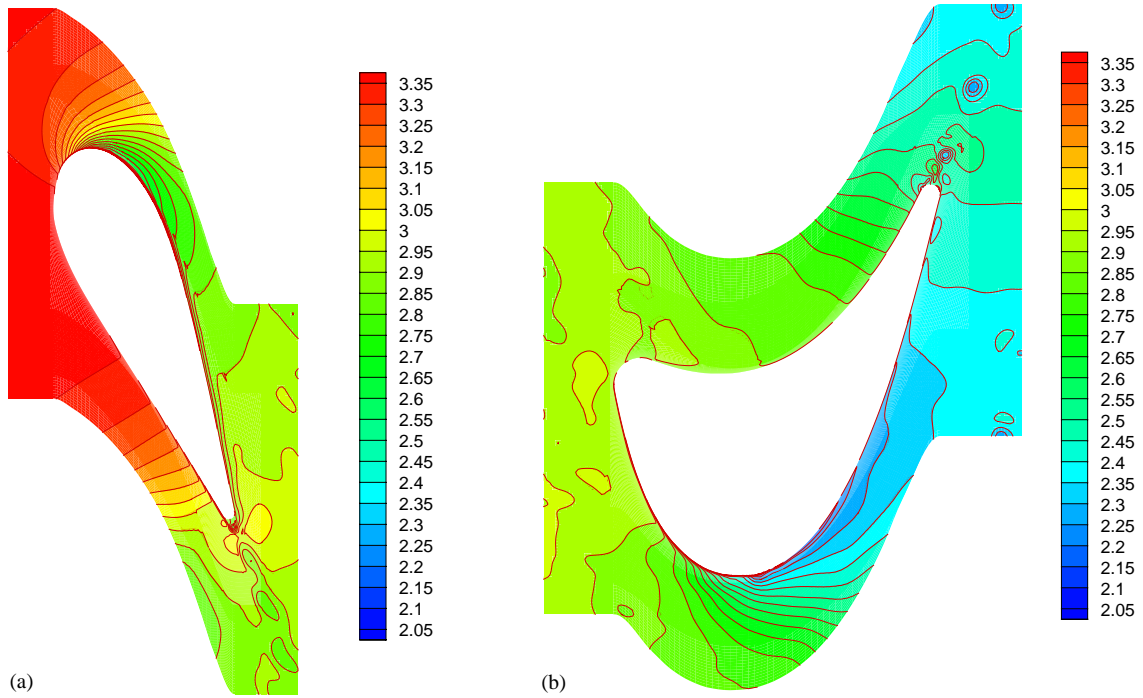
Fig. 17. POD reconstruction of state variable e on the stator and rotor at $t = 0$ using 40 modes (from Cizmas and Palacios [144] with permission). (a) Stator and (b) rotor.

By comparing these results with the original, full model, spatio-temporal evolution of energy shown in Fig. 16, Cizmas and Palacios conclude that most of the details of the flow were captured by using 40 POD modes. Notice that the stator flow was better captured than the rotor flow because the flow on the rotor was more complex, mainly due to the impact of the wakes coming from the stator. The differences between the two solutions varied between −0.0141 and 0.0123. Consequently, the error varied at most between −0.61% and 0.53%. The largest errors occurred in the region that is facing the downstream row and they were concentrated in the wake region.

Both the work of Epurneau et al. and Cizmas and Palacios verify the low-dimensional dynamics associated with internal flow problems and motivate continued research into identification of efficient, ROMs applied to practical design problems of interest to turbomachinery designers.

4.3. POD for the discrete Euler equations

A great deal of research has been accomplished in the past decade applying POD to fluid dynamics problems. The application of POD to incompressible flow problems has enjoyed a great deal of success [45,46, 145–148]. In preparation for aeroelastic analysis with POD, additional research is being conducted to apply

POD to compressible flow problems. This next section summarizes results obtained at the Air Force Research Laboratory demonstrating POD for nonlinear, compressible flows. Several major research questions were addressed by these activities that have enabled a more complex application of POD to fluid–structure interactions. In the results that follow, compressibility affects were considered by applying POD to the discrete Euler equations.

4.3.1. Steady and unsteady results using subspace projection

To study the application of POD to problems in aeroelasticity for which the ROM is nonlinear, Pettit and Beran have first examined flowfield response to steady and unsteady changes in structural shape. ROMs in this section were formed using sub-space projection (see Section 2.2.4). One such problem, which has proved valuable, is the response of inviscid flow over a deforming panel in two space dimensions [52,104]. The flowfield is situated above an infinite panel that lies in the $y = 0$ coordinate plane, except for a segment between $x = -\frac{1}{2}$ and $\frac{1}{2}$ for which the panel shape is a parabolic arc defined by $y_s(x, t) = \delta(t)(1 - 4x^2)$. For steady problems, the amplitude parameter δ is a specified constant, while for unsteady problems, $\delta(t) = \delta_1 \sin(\omega_t)(1 - e^{-\alpha t})$ is assumed, where δ_1, ω, and α are constants. The length of the "bump" and the far-field

velocity, U_∞, serve in the nondimensionalization of the aerodynamic analysis. A schematic of the bump and the 71×141 baseline grid are shown in Fig. 18.

The flowfield response is assumed to be governed by the Euler equations, which are discretized and solved with the upwind total variation diminishing scheme of Harten [149] and Yee [150]. A transpiration condition is used by Pettit and Beran to satisfy approximately the boundary conditions on the bump surface while not requiring grid deformation.

Pettit and Beran [53] conduct an analysis of flow changes in response to static changes in amplitude of the bump described above, and their results are summarized here. The algorithm for full-system analysis is validated by comparing computed results with those obtained using Cobalt$_{60}$, an unstructured, finite-volume algorithm for the Euler and Navier–Stokes equations [151] that has been validated extensively. Differences in the predictions of the two techniques are small for variations of both Mach number and bump amplitude in the range of interest.

A single, ROM for the steady-state bump is constructed from 26 full-system solutions computed at Mach 1.1, 1.15, 1.2, 1.25 and 1.3. At each Mach number, snapshots are computed at several different values of δ. For a given Mach number, there is a critical bump amplitude beyond which the shock attached to the leading edge of the bump detached, forming a bow shock. At sufficiently large values of δ and prior to shock detachment, response of the system is nonlinear to changes in δ. Once the bow shock forms, flow structure (i.e., shock position) becomes highly sensitive to additional changes in Mach number and bump amplitude, a situation not well suited for POD analysis. Thus, most sampling and ROM application is limited to cases for which the flow is entirely supersonic.

With 26 solutions, a total of 104 modes are computed. Pettit and Beran examine results when all modes are included in the analysis and when there is truncation to 60 and 40 modes [53]. The full-system solutions to (15) are time integrated to steady state with 2000–10,000 function evaluations, depending on parameter selection, and are initialized with uniform flow. While these cases were computed serially, they could also have been computed in parallel. Up to a point, sampling is a naturally parallel process; as a solution space is revealed, fill-in cases can be computed when resources become available. Equilibrium solutions of the POD-based ROM, satisfying (28), are computed along paths of constant Mach number and varying δ, starting with the trivial solution at $\delta = 0$ and progressing in increments of $\Delta_\delta = 0.001$. At each point, ROM values are initialized using the previous solution, and solutions are typically computed in 3–10 function evaluations. Computing on the order of 100 solution points with the ROM typically requires fewer function evaluations than those necessary for a single solution of the full system.

Pettit and Beran interpreted the steady-state results using the minimum local Mach number, which typically is observed at the bump leading edge [53]. Examination of other flow variables did not alter their conclusions concerning the viability of the POD-based ROM. Solutions are compared in Fig. 19. Full-system solutions not used as ROM snapshots are also computed to obtain predictions of system behavior away from snapshot locations. Norms of the full-system residual are readily computed after each function evaluation in the subspace projection method and are used to evaluate the quality of reduced-order solutions. Modeling of parameter-space subdomains where residual norms become unacceptably high can be improved by retaining different sets of modes or through model reconstruction. In the
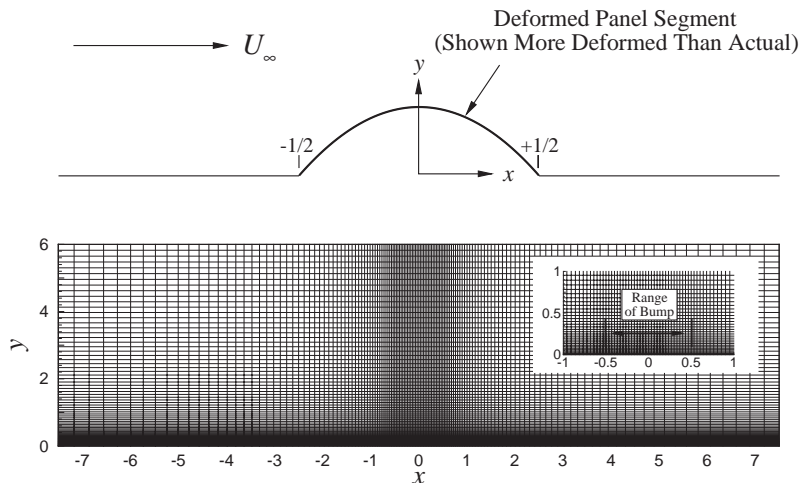

Fig. 18. Top: schematic of panel and coordinate system. Bottom: baseline grid.
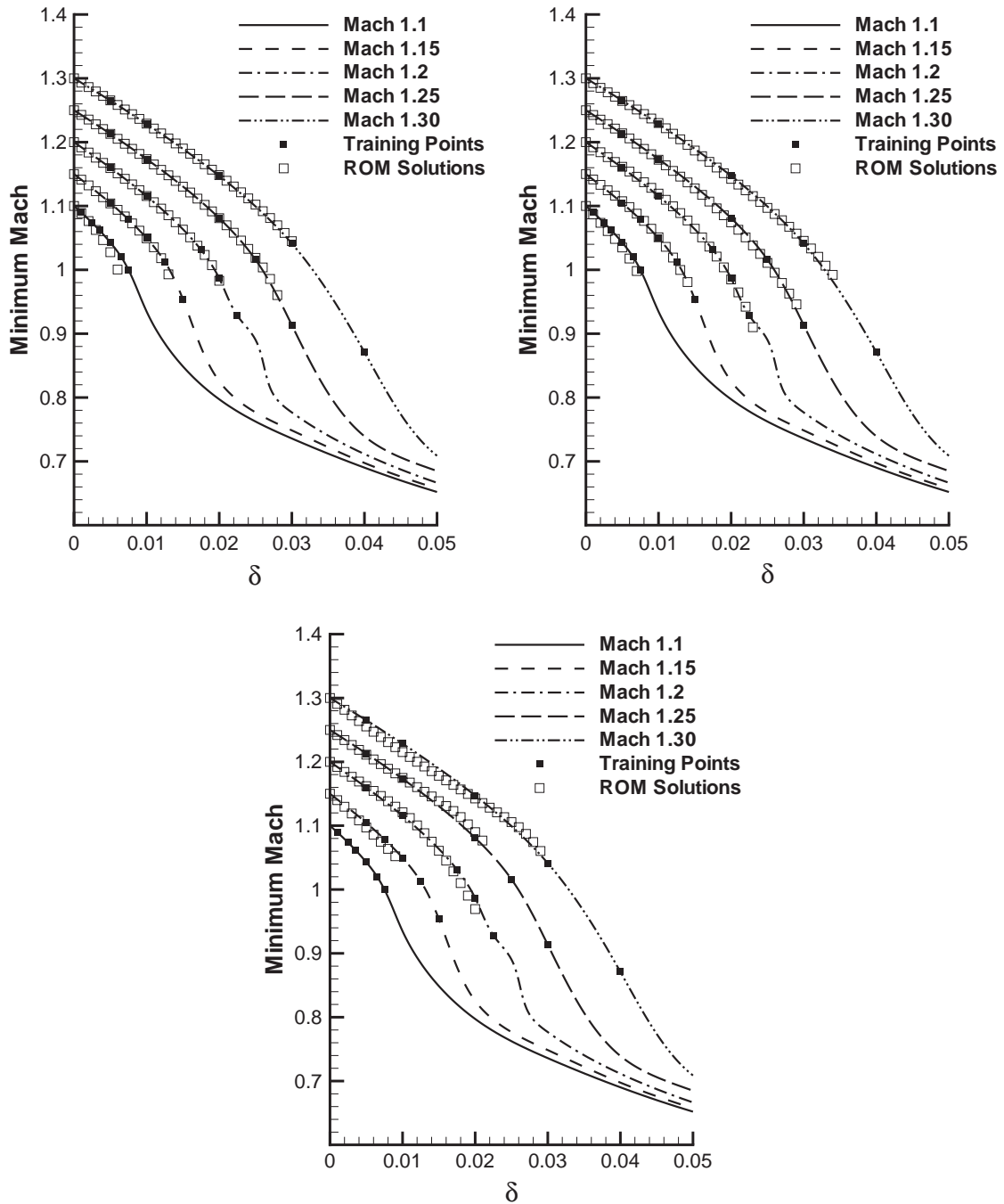
Fig. 19. Minimum local Mach number achieved by full-system and ROM solutions at selected freestream Mach numbers and bump amplitudes: left: all 104 modes; middle: 60 modes; right: 40 modes.

figures just cited, only ROM solutions with a residual norm less than 0.6 are displayed. Pettit and Beran found this cutoff value to be consistent with good ROM solutions for the configuration being investigated. When 60 or all 104 modes are retained, ROM solutions are highly accurate and reproduce the nonlinear behavior

evident in the response of the full system. Interestingly, the 60-mode ROM is somewhat superior to that of the full, or 104-mode, ROM. Pettit and Beran speculate that higher-order modes in the 104-mode ROM, which possess length scales on the order of the node spacing, can lightly pollute solutions with the present scheme,

which makes no attempt to filter out such modes. However, in the steady-state analysis, modes are retained that are much smaller in magnitude (eigenvalues of $\mathbf{S}^T\mathbf{S}$ as small as 10^{-10}) than those of the dynamic analysis. The fundamental difficulty with retaining low-energy modes in the dynamic analysis is not observed in the steady-state analysis. Retaining a large number of low energy modes is not a practical problem, since it is desirable to use fewer than the maximum number of modes. When the number of retained modes is decreased to 40, the accuracy of the ROM is nominally degraded, and the number of computed points satisfying the residual norm cutoff is diminished. Most notably, solutions at Mach 1.1 do not meet this criterion, which may not be surprising, since these points are on the boundary of the snapshot region and reflect the most nonlinear fluid dynamic behavior.

Beran and Pettit have also computed unsteady solutions of the Euler equations for supersonic flow over an oscillating bump with an implicit, POD formulation. Their results [104] are reported here to document the robustness and accuracy of the implicit technique described in the Analysis section. They consider a Mach 1.2 flow over a bump with oscillation specified by the following baseline parameters: $\delta_1 = 0.005$, $\omega = 1.0$, and $\alpha = 3$. The computational domain is discretized in a manner equivalent to that used in the steady-state analysis. A POD-based ROM is constructed for the baseline case by explicitly integrating the discrete equations, expressed as (15), and collecting snapshots. Integration is carried out for 20 time units (approximately four cycles) with a time step of 0.01, the maximum value observed to permit stable integration. A total of 200 snapshots, each representing a collocation of the conserved variables over the computational domain, are collected at 10-iterate intervals. The initial state of the flowfield is specified to be uniform flow at freestream conditions and is used in the definition of $\mathbf{W}_0$.

Pettit and Beran [52] block the snapshot matrix so that the non-trivial elements of each column of $\mathbf{S}$ represent only one of the conserved variables at a specified instant. In this manner, the 200 snapshots described above fill $\mathbf{S}$, which is organized as a block diagonal matrix with a total of 800 columns. Each block is associated with one of the conserved variables, as are each of the 800 computed modes. This approach is inefficient for very large problems owing to the increased size of $\mathbf{S}$, but leads to an adaptable framework for computing modes for each conserved variable.

Following (14), ROMs are computed for between 6 and 20 retained modes. With 20 modes retained, the number of DOFs is decreased by a factor of 2000. Pettit and Beran observe that with as few as eight modes retained, ROM integration yields very accurate results in comparison to full-system analysis for the case used to construct the ROM. This result is illustrated qualita-

tively in the left and middle portions of Fig. 20, where the structure (and magnitudes) of the density fields near the bump explicitly computed with a 14-mode ROM and full-system analysis are nearly identical (shown at the end of the sampling period, $t = 20$). In the right portion of Fig. 20, time histories of pressure at the bump midpoint are reported for a 10-mode ROM implicitly computed with the Crank–Nicolson scheme. There it is seen that implicit integration of the ROM accurately reconstructs the aerodynamic response, even using time steps 40 times larger than needed for explicit integration of the full system. Results are shown for five subiterates in the Crank–Nicolson scheme; solutions can be obtained with two subiterates (without loss of accuracy), an order of magnitude faster than with full-system analysis.

In a manner motivated by the frequency-domain analysis of Hall et al. [50], Pettit and Beran [53] construct hybrid ROMs combining snapshots computed for different bump amplitudes and frequencies. These hybrid ROMs successfully reproduce aerodynamic responses for cases not explicitly included in the sampling process. For the bump problem, the sub-space projection method yields numerically divergent results when the number of retained modes exceeds 19 [52,53]. By increasing the number of modes, the onset of divergence can be delayed, and the accuracy of the ROM solution increased prior to divergence. At present, the cause of this instability has not been identified; however, a violation of mass conservation in the system can be associated with the onset of divergence, which suggests a direction for future examination.

4.3.2. Quasi-steady shock motion

The application of POD to flows with shocks is a challenging endeavor, owing to the obvious difficulty of capturing movements of solution discontinuities with a fixed set of global modes. There are two classical approaches to the moving shock problem: shock fitting and shock capturing. We will provide some detail on the use of POD in a shock fitting approach as introduced by Lucia et al. Shock fitting with POD has also been investigated by Brooks and Powers (see [152]), and we refer the reader to the literature for more information on their technique.

Lucia [113] demonstrated the utility of POD for modeling the quasi-static movement of strong shock waves in a quasi-one-dimensional nozzle. The location of the standing shock was varied by altering the ratio of specific heats in the Euler equations. It was observed that with straightforward application of the nonlinear POD analysis described in Section 2.2.4, accurate modeling of shock movement required an excessively large number of modes and data samples. Essentially, one snapshot was needed for every grid point location traversed by the moving shock. To improve the
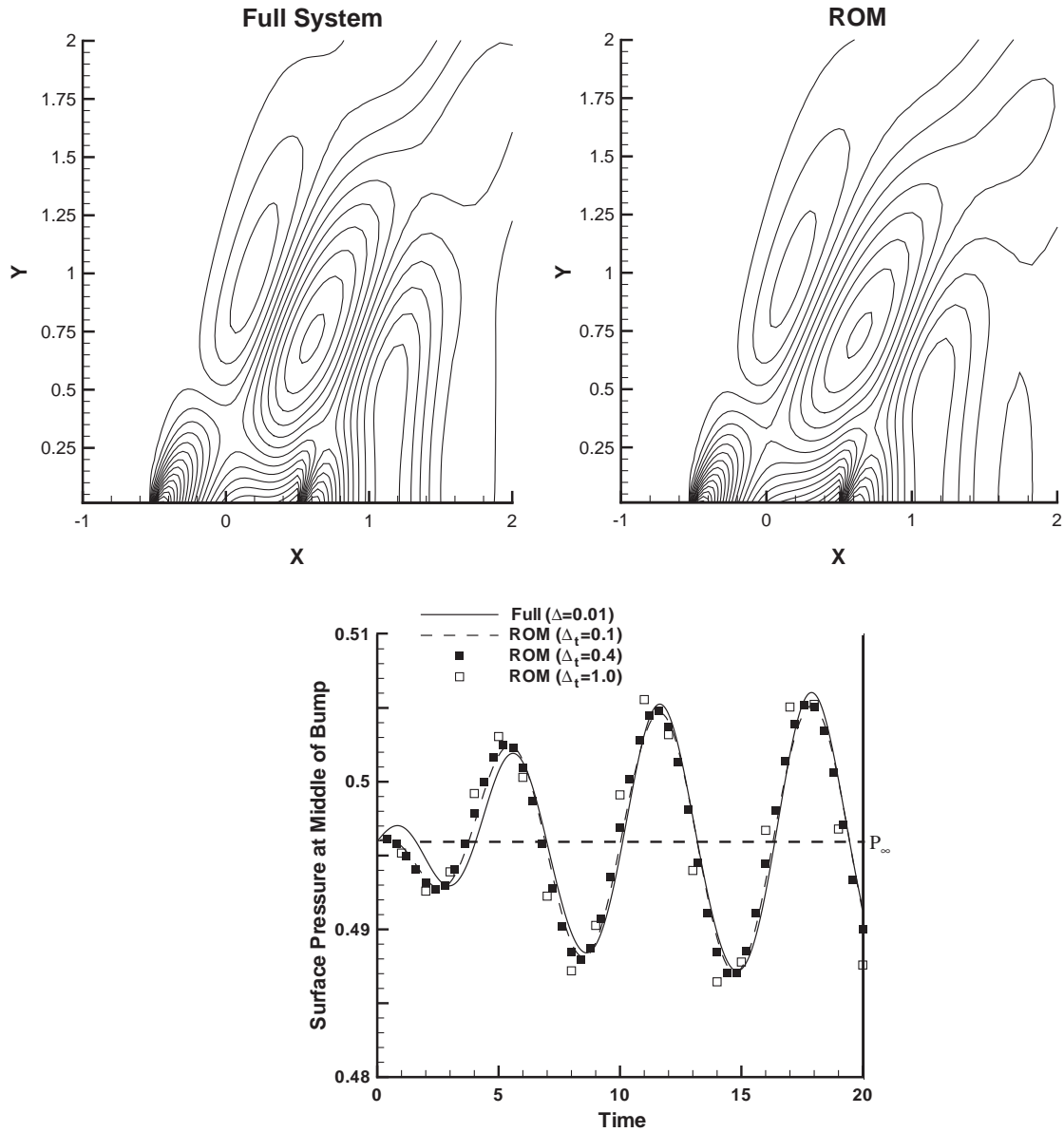
Fig. 20. Comparison of full-system and POD-based ROM predictions of aerodynamic response to bump oscillation ($\delta_1 = 0.005$). Left and middle: computed density contours at time $t = 20$ (14-mode ROM). Right: time histories of computed surface pressure at bump midpoint for different integrations of 10-mode ROM.

effectiveness of POD for problems of this type, Lucia [106] proposed the domain decomposition approach detailed in Section 2.2.6. With almost no degradation of accuracy, this methodology captures shock movement in the nozzle, see Fig. 21, using an order of magnitude fewer DOFs. The ability to model the shock region with POD was also demonstrated by Lucia [113], along with the special techniques required to realize the ROM.

Lucia et al. [107] extended the domain decomposition method to quasi-steady shock motion in 2-D. In this application, the desired output was a steady-state, supersonic flow-field around a blunt body. From this steady-state flow field, surface pressures were extracted to serve as the key parameter for accuracy determination. The inputs for the system were free stream Mach number and AoA. Since the free stream Mach number was supersonic for this study, the steady-state flow field contained a bow shock of a strength and location that varied based on free stream conditions. The parameter space of interest was a window of AoA and Mach
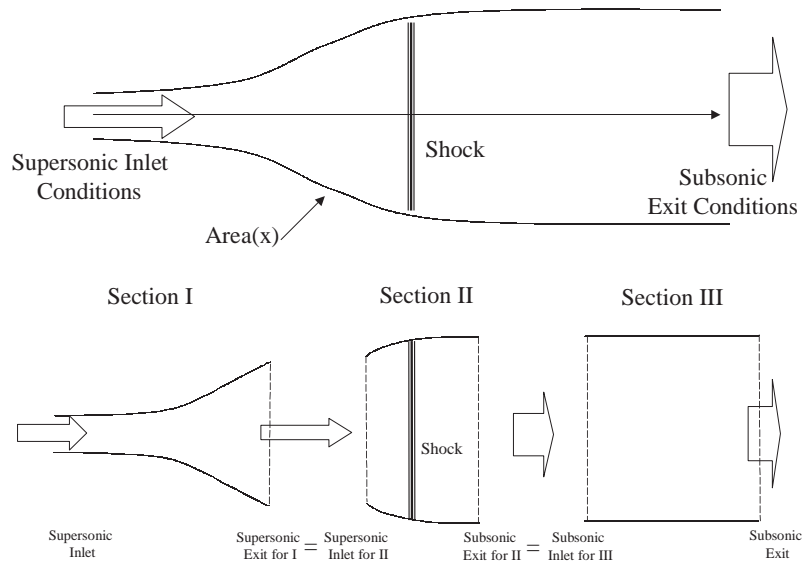
Fig. 21. Top: nozzle with standing shock. Bottom: decomposed domain for POD analysis.

number. Surface pressures at steady state were desired across this parameter space. When stepping between steady-state conditions transient flow field behavior was not of interest; only the quasi-steady shock motion obtained after reaching the various steady-state conditions was important. Quasi-steady shock motion and AoA for a parameter range of Mach number were within the steady-state shock locations for Mach 2.5, AoA $0°$, and Mach 5, AoA $0°$. Steady-state pressure contours for these cases are shown in Fig. 22.

The blunt body geometry was a $15°$ wedge with a circular nose and was generated using two line segments tangent to a circle. A structured grid with 53 nodes along the solid surface and 35 nodes extending to the free stream was generated, as shown in Fig. 23. This grid was developed to align cells with expected shock locations to yield a smooth shock wave across the parameter space of interest. The number of cells in the selected grid was determined to have reasonable fidelity for this problem through an informal analysis of shock resolution versus number of grid points.

The reduced-order modeling goal was to identify a low-order system with POD by using the same system inputs and outputs described for the full-order system as a more efficient means of studying the Mach number and AoA parameter space. Domain decomposition was used to isolate a region of the computational mesh containing the shock motion. The solution methodology for steady analysis of the ROM with a full-order shock region involved a combination of explicit time integration with a chord method implementation (see Section 2.2.4). No domain overlap was used for this implementation.
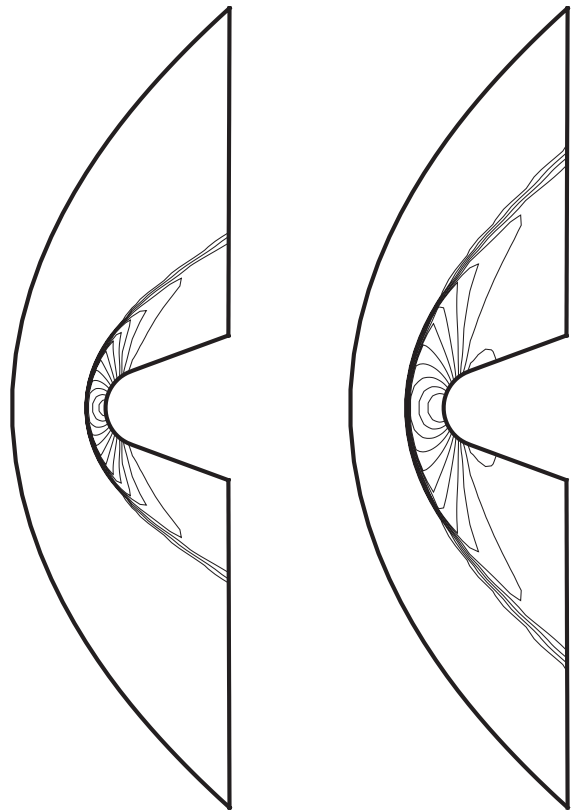

Fig. 22. Steady-state pressure contours for Mach 5 (left) and Mach 2.5 (right).

When adjoining domains were modeled with POD, additional restrictions were required to produce solutions that match at the internal boundaries. Enforcing
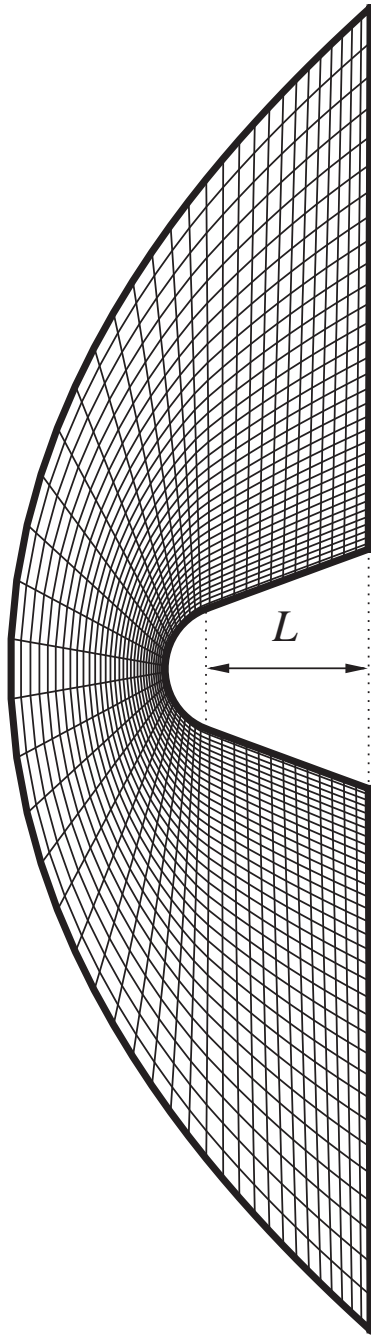
Fig. 23. Blunt body geometry.

smoothness on the boundary for solutions of adjoining regions required overlapping the domains. Smoothness in the overlap regions was enforced by using Lagrange constrained optimization as described in Section 2.2.6.

The results that follow refer to the POD implementation using a full-order shock region, and are a summary of Lucia et al. [107] POD training was accomplished using steady-state flow field solutions. Steady-state solutions were obtained from the full-order solver at AoAs $-2°$, $-1°$, $0°$, $1°$, and $2°$ and Mach numbers of 2.5, 2.6, and 2.7. All combinations of these parameters produced 15 snapshots. The resulting ROM was comprised of eight DOFs from POD, and the entire ROM totaled 1644 DOFs when the full-order shock region was included. Without POD, this problem contained 7072 DOFs at full order.

The numerical efficiency was evaluated by comparing wall-clock time for comparable runs of both the full system and the ROM. A realistic expectation for computational improvement comes from the reduction in DOFs. For this problem, the reduction in DOFs was 4.3 to 1. A similar improvement in computational efficiency can be expected from a reasonable implementation of the ROM. The full-order solver reached the convergence threshold after 1300 iterations. Wall-clock time was 37.73 s. The ROM converged in 900 iterations of the full-order shock region, requiring 8.51 s of wall-clock time. The computational improvement for this case was 4.43 to 1. The ROM converged to steady-state in fewer total iterations than the full-order solver due to the chord method implementation other domain sections. The implicit ROM formulation in the domain section behind the shock converged to steady state very quickly and did not require any Jacobian updates throughout the solution procedure. As a result the wall-clock time savings was slightly better than expected when considering the reduction in DOFs.

The accuracy of surface pressure values from the ROM was examined across a parameter space well beyond that for which the POD was trained. The ROM performed well at parameter values within or near the limits of the training. Errors in surface pressure were less than 1% everywhere on the surface for AoAs less or equal to $2°$ and Mach numbers between 2.5 and 2.7. The errors were larger the farther the ROM was removed from the training window in the parameter space. To illustrate accuracy, steady-state solutions were obtained across the parameter space. The steady-state pressure distributions were integrated across the body surface to produce C_L.

The difference between these results and the results from the full-order solver are shown in the bottom portion of Fig. 24. Notice that the errors in C_L grow as the parameter space was extended beyond the training window in both Mach and AoA. This error growth was reduced by adding more modes from the same training window. The same C_L error plot for a ROM using 20 POD modes is shown in the lower portion of Fig. 24. ROM performance could have been enhanced further by extending the training window to encompass more of the parameter space, but POD's accuracy at producing steady-state solutions within the training window did not require further demonstration.
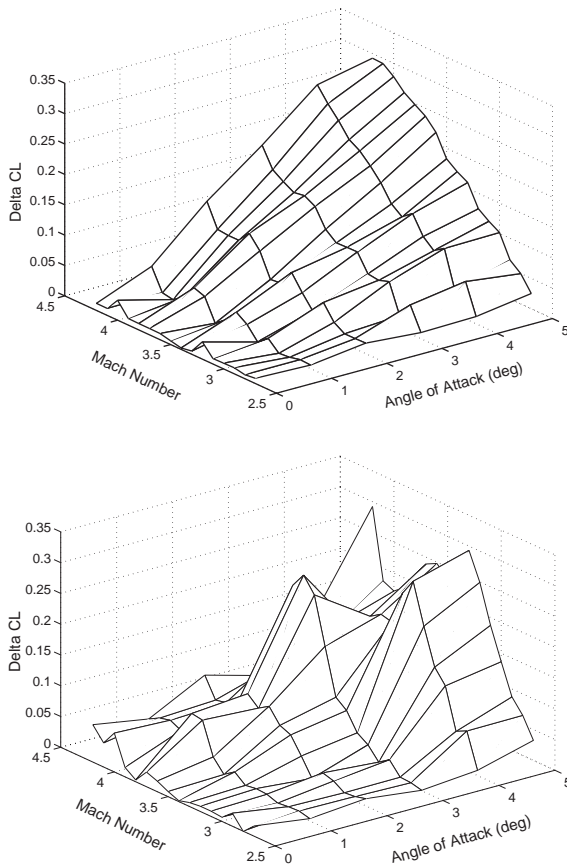
Fig. 24. C_L error for steady analysis, 8 POD modes (upper) 20 POD modes (lower).

These results demonstrate the potential of POD with domain decomposition for application to steady, high speed flows with quasi-steady shock motion. Model training was very robust across a wide parameter space for the portions of the flow field without the moving shock wave. Unsteady applications will require reduced-order modeling of the shock region, and this requirement will be addressed as part of the LCO applications to come (Section 4.4.4). POD training for moving shocks is not problematic for applications with repetitive or cyclical shock motion. Training of the ROM using time integration of the shock motion is extendable across a parameter space in such applications [56,113]. A Galerkin approach for high speed problems would improve computational performance and perhaps robustness. Efforts to develop low-order projection methods are addressed next.

4.3.3. Low-order projection methods

Lucia and Beran [108] developed a general POD implementation of both Galerkin and Direct projection

for the Euler equations (see Section 2.2.5). These methods were applied to a 2-D, inviscid flow problem along a solid wall containing a small circular arc. While both Galerkin and Direct projection are extendable to nonlinear applications, the initial application [108] was linear for simplicity. The geometry for this analysis was the same as described earlier in Section 4.3.1, and shown in Fig. 18. Unsteadiness was introduced by spatially varying the ratio of specific heats, γ, with time. The unsteady forcing term $\gamma \equiv \gamma(\mathbf{x}, t)$ enters (15) through the flux terms in the Euler equations. This type of forcing was selected to provide unsteady behavior without the added complication of a dynamic boundary condition. γ is a time varying spatial function formed by modulating $f_{\mathrm{mod}}(\mathbf{x})$ with a time-varying scalar function $g(t)$ as follows:

$$\gamma(\mathbf{x}, t) = \gamma_{xy}(\mathbf{x}) + g(t)f_{\mathrm{mod}}(\mathbf{x}). \qquad (76)$$

The function $\gamma_{xy}(\mathbf{x})$ is the base value γ assumes when no forcing is applied. $f_{\mathrm{mod}}(\mathbf{x})$ was a two-dimensional Gaussian distribution as depicted graphically in Fig. 25 and was discretized using the computational mesh for the full-order solver. The fixed panel deflection from Fig. 18 was a circular arc of length 1 and height 0.001 centered at $x = 0$, $y = 0$, and the Gaussian curve was centered directly above it at $x = 0$, $y = 2.5$. The covariance terms determine the spread of the Gaussian curve and were $\sigma_x = \sigma_y = 0.25$. The time varying function $g(t)$ was defined as

$$g(t) = \alpha \sin(\omega t). \qquad (77)$$

For the results that follow, the baseline amplitude was $\alpha = 0.07$, and the baseline frequency ω was 0.2145.

In Lucia et al. [108], the Galerkin and direct projection methods of Section 2.2.5 were used to identify a system of ODEs for this model problem at the baseline amplitude and frequency. Additional dissipation was required to stabilize the ODEs, and varying types and amounts of dissipation were explored. The ODEs generated from both methods were compared by
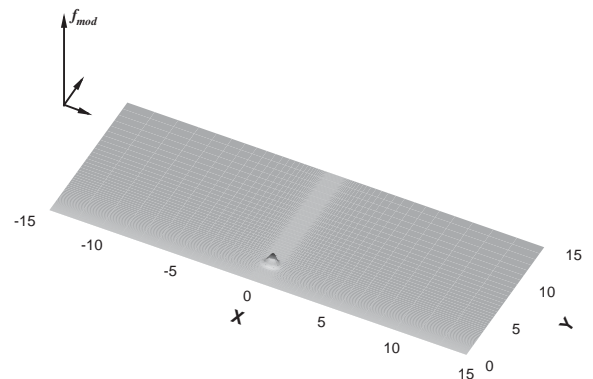

Fig. 25. Modulating function for γ.

examining the eigenvalues of the state-space dynamics matrix. Accuracy was assessed by comparing the modal amplitude responses. The time histories of $\hat{w}$, once expanded to w using (13), were also compared with the pressure time history of the full-order system. Both the pressure time history results and the computational performance improvement are summarized here.

Time responses of surface pressure for various ROMs are compared to the full-order system in Fig. 26, which provides the time history for three cycles of fully developed flow. The reduced-order results using subspace projection are considered along with the Galerkin and direct projection ROMs. Linear quadratic regulation (LQR) was used in addition to artificial viscosity to stabilize the Galerkin reduced-order system. LQR was also able to stabilize the direct projection ROM, which contained no artificial viscosity term.

The explicit subspace projection ROM introduced a slow growing instability after the third cycle. These instabilities were consistent with other instances of subspace projection reported in the literature [52,53]. Eliminating the second y-momentum mode improved stability as shown in Fig. 26. Otherwise, the implicit and explicit subspace projection ROMs produced identical results with a bias error in the pressure response. This bias error was the result of a peculiar behavior of the response for the second modes.

Neither the Galerkin nor the direct projection ROMs suffered any instabilities, and average errors were less than 5% for both. The Galerkin projection ROM matched the full-system response better than the direct projection results. The direct projection ROM had a slightly muted response. This difference is insignificant,

since the direct projection response could be tuned to match the full-order results more closely by iterating the weights used for LQR. No ROM matched the transient period ($t < 15$ s) within 10% average error, but this degraded performance was expected since the transient flow field data was not sufficiently sampled by the snapshots.

The motivation for employing projection methods with ROM was to realize a computational performance improvement consistent with the reduction in the number of DOFs. Computational performance, summarized in Table 1, was assessed by measuring the wall-clock time for each solver to provide an 88 s time history of the flow. All computations were run on a 800 MHz Pentium-based personal computer.

The explicit non-Galerkin method (the fastest of the two subspace projection methods) was not nearly as efficient as the Galerkin or direct projection approach, because the subspace projection method used the flux evaluation of the full-order model. Sub-space projection truncated high-frequency oscillations and permitted stable integrations at a Courant–Friedrichs–Lewy (CFL) condition of 5 (the full-order model required CFL < 1 for stability). The larger time step associated with the large CFL number yielded the reduction in wall-clock time shown in Table 1. Notice that subspace projection only provided one-order of magnitude reduction in computation time to accompany four orders of magnitude reduction in DOFs. In contrast, Galerkin and direct projection both reduced compute time by four-orders-of-magnitude and realized an improvement in performance consistent with the DOF reduction.

These promising results for the linearized Euler equations with fixed boundaries motivates the extension of these projection methods to nonlinear problems with moving boundaries. The computations required to evaluate Galerkin projection of the nonlinear Euler equations would not be prohibitive following the approach described in Lucia et al. [108]. Of-order analysis could be used to reduce the number of nonlinear terms prior to data collection and integration. This might favor the Galerkin approach over direct projection, where computing higher-order terms might become prohibitive, even with reduced-order Jacobians. The extension to moving boundaries would require coupling the boundary operator with the flow field to
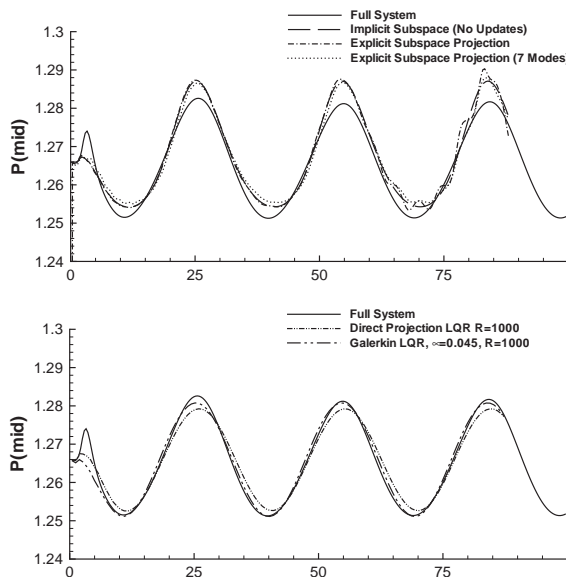

Fig. 26. Time history of panel pressures for various ROMs.

Table 1
Computational performance

Flow solver	DOFs	Wall-clock time (s)
Full-order	64,400	310.256 s
Subspace ROM	8	77.902 s
Galerkin/direct ROM	8	0.08 s

produce a single operator describing the entire system. Either Galerkin or direct projection of this new operator could use modes describing both the interior and the boundary to produce very efficient ROMs for free boundary problems.

4.4. POD analysis of LCO

The determination of aeroelastic behavior is a demanding problem owing to the capture of system nonlinearities, including structural nonlinearities, which play a key role in the aeroelastic phenomenon of LCO [51,121,153,154]. To capture the effects of aerodynamic nonlinearities on aeroelastic behavior, time-integration methods based on the transonic small-disturbance, Euler and Navier–Stokes equations have been developed. These methods can provide accurate approximations of system behavior but generally require very large computation times owing to the time-accurate nature of the calculations and the large integration times required to establish flow stability properties. Direct methods formulated from Hopf bifurcation theory have been developed to compute flutter and LCO onset speeds of aeroelastic systems without time integration [98–100,126] but become computationally expensive when system order becomes large. This next portion of the Results is dedicated to recent work regarding LCO analysis with POD. It encompasses a summary of results obtained from POD analysis of a reacting flow problem as well as the response of an elastic panel in subsonic, supersonic, and transonic cross flow.

4.4.1. Hopf bifurcation in a tubular reactor

To assess the applicability of POD-based ROMs to differential equations that exhibit LCO, Beran et al. [51] computed solutions of a tubular reactor, known to experience LCO [155,156], with the subspace projection technique. The governing equations are

$$\frac{\partial w_1}{\partial t} = Lw_1 - w_1 Q(w_2), \tag{78}$$

$$\frac{\partial w_2}{\partial t} = Lw_2 - \beta_1(w_2 - \beta_3) + \beta_2 w_1 Q(w_2), \tag{79}$$

$$L \equiv \frac{1}{\text{Pe}}\frac{\partial^2}{\partial x^2} - \frac{\partial}{\partial x}, \quad Q(w_2) = \mu \exp\left(\Gamma - \frac{\Gamma}{w_2}\right),$$

where Pe, β_1, β_2, β_3, Γ, and μ are specified parameters. Eqs. (78) and (79) describe convection, diffusion, and reaction within the reactor and are referred to as the convection diffusion reaction (CDR) equations. The variables w_1 and w_2 represent concentration and temperature, respectively, and the parameter μ (the Damkohler number) determines the ability of the CDR equations to sustain LCO. The spatial domain is normalized; boundary conditions are applied at $x = 0$ and $x = 1$. Following spatial discretization of the

equations and specification of suitable initial conditions, which are details described elsewhere [51], the CDR equations take the form $d\mathbf{w}/dt = \mathbf{R}(\mathbf{w}; \mu)$.

The CDR system experiences a supercritical Hopf bifurcation at $\mu^* \equiv \mu = 0.16504$ [51] which is accurately predicted by a POD-based ROM. The stability properties of the CDR system are shown in Fig. 27, which shows that stability of the equilibrium system is lost beyond the bifurcation point. Solutions are characterized by the maximum value of temperature computed over the domain, T_{max}. The ROM is developed by sampling the CDR system as it evolves towards steady state $(0 \leqslant t \leqslant 2.5)$ for a value of μ leading to system stability: $\mu^0 = 0.16 < \mu^*$. Following this procedure, eight modes are computed and retained, representing a 15-fold reduction in problem size. Solutions of the full system are explicitly computed with time integration using a maximum time step of 0.0005 (limited by numerical stability). Equilibrium solutions of the ROM are computed with the procedure described above, while LCO solutions are found with an explicit procedure like that applied to the full system [51]. It should be noted that even with the explicit procedure, dynamic solutions of the ROM can be obtained with time steps 50 times larger than 0.0005. This increase in allowable time step is a consequence of the absence of high-frequency, odd-even modes in the POD-based ROM that would destabilize the numerical scheme [51].

Equilibrium solutions of the full system and the ROM are observed to be in excellent agreement. As seen in Fig. 27 (left), agreement is nearly exact at $\mu^0 = 0.16$, where the POD is constructed, and is excellent for the remaining values of μ shown. A slight inaccuracy is introduced at the Hopf point, where new system behavior becomes available. Beyond the Hopf point, LCO amplitude is well predicted with the ROM. Quantitative differences between ROM and full-system solutions can be reduced with nominal improvements in sampling (increasing the number of retained modes or increasing the sampling period [51].

The critical value of μ at which the CDR system loses stability is also very accurately predicted using reduced-order modeling. The variation of the stability parameter γ computed with the ROM (cf. (32)) is shown in Fig. 27 (middle). Stability loss is observed at $\mu = 0.16503$, nearly the same value predicted with the full-system equations ($\mu = 0.16504$). The Hopf point is computed directly with Newton's method in 11 iterations ($\omega_{hopf} = 0.5$), starting with the equilibrium solution at $\mu = 0.16$.

Sensitivity of the variable T_{max} to the bifurcation parameter μ is computed with the ROM formulation (31) at $\alpha = 0.164$ using the 8-mode ROM described above. As shown graphically and quantitatively in Fig. 27, the accuracy is excellent, with only a 1% difference between the ROM and full-system results.
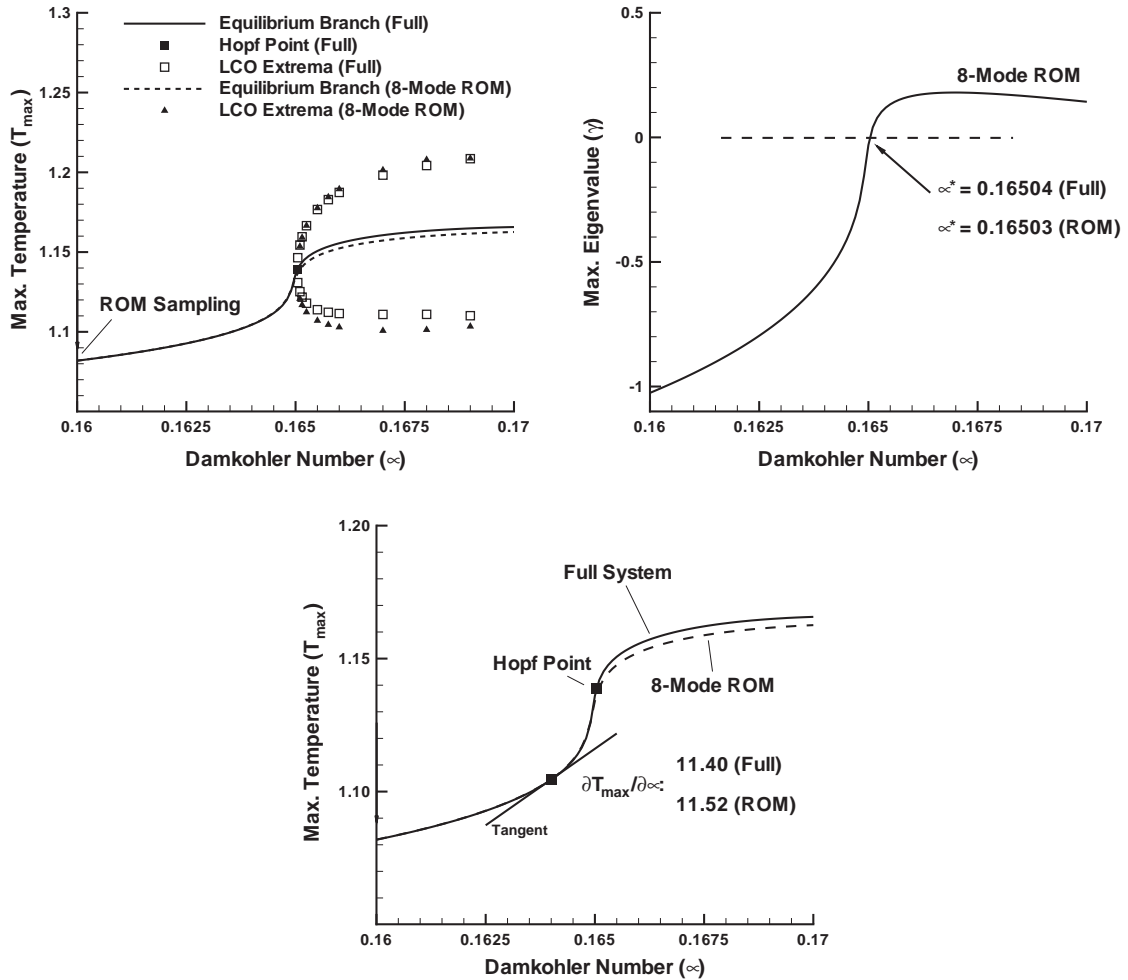
Fig. 27. Comparison of full-system and ROM solutions for an 8-mode ROM trained at $\mu^0 = 0.16$. Left: equilibrium and LCO branches. Middle: ROM system stability. Right: sensitivity to μ variation.

4.4.2. Panel LCO with subspace projection

Subsequent work by Beran et al. [54,55] applied POD to the Euler equations in an effort to capture aerodynamic nonlinearities in a reduced-order aeroelastic model. The results from Beran et al. [55] are highlighted below. A low-order POD representation of the discrete, 2-D Euler equations [52] was coupled with the von Kármán equation to simulate the dynamics of flow over a flexible panel [54]. ROMs in this section were formed using subspace projection (see Section 2.2.4). For supersonic flows that were essentially linear (Mach 1.2), LCOs were accurately computed with the POD model using time steps of moderate size. In a more recent work [55], the methodology was substantially altered to improve the temporal coupling between the aerodynamic and structural dynamic equations, thereby greatly increasing the allowable time step and decreasing the computational effort necessary to achieve LCO.

Furthermore, a modal representation of the structure is employed, which permits a more efficient formulation of the reduced-order aeroelastic system, further increasing computational efficiency. The modal representation also permits judicious application of structural damping to temper the spurious behavior of some eigenvalues of the low-order aeroelastic system that apparently arises from the form of data sampling used to construct the ROM. With very small amounts of damping, a direct method was used to predict the onset of LCO at a Hopf bifurcation point at least two orders of magnitude faster than with the full-order model.

Results obtained with reduced-order representations of the aeroelastic system are now presented for Mach 0.9 and 1.2. First, at Mach 0.9, a ROM was constructed to directly predict the critical value of λ at which the panel loses stability to non-trivial, steady deflections. This procedure was repeated for Mach 1.2 following

construction of a second ROM, but in this case, the new ROM was also used in the calculation of LCOs at selected dynamic pressures.

At Mach 0.9, a 10-mode ROM was constructed using four steady solutions computed for $\lambda = 20$ and $\lambda = 30$ on the inward- and outward-deflected solution branches. A search procedure was carried out to compute the crossover point. The search procedure was very fast, requiring about two-CPU minutes on a 1.13 Ghz laptop computer and 10–15 iterations, depending on initial guess and jump size. In comparison, computation of a single steady-state solution required about two CPU hours on the same class of computer.

When the 10 most significant modes of the ROM were retained, the location of the bifurcation point was computed to be $\lambda = 15.28$. This value was lower than that found with the full-order analysis, which brackets the bifurcation point between $\lambda = 18$ and 18.5. See Fig. 28. Direct prediction of the bifurcation point, while precise for a specified number of POD modes, was found to be somewhat sensitive to the number of retained modes, M_r. For a moderate number of retained modes, a trend of decreasing dynamic pressure at the critical point with increasing M_r was established: 17.16 ($M_r = 8$), 16.74 ($M_r = 9$), 15.28 ($M_r = 10$), and 15.05 ($M_r = 11$). When 12 or more modes were retained (up to 16 maximum), the modes appear to lose linear independence, and the results became unreliable. With less than eight modes, there appeared to be too little information representing the system. Thus, for the ROM constructed, the bifurcation point was between about 15 and 17, depending on M_r.

Solutions exhibiting accurate LCO behavior were obtained with a POD-based ROM constructed for Mach

1.2 and $\lambda = 25$. This same ROM was used in the direct determination of the critical value of λ at which the panel first lost stability. A 10-mode ROM was constructed from 40 full-system samples collected at a uniform rate during the first 20 time units of a computation that required about 300–400 time units to establish LCO. With this number of modes, about 98% of the energy represented by the sampled data was retained. The ROM was found to predict LCO frequency and amplitude with reasonable accuracy up to about $\lambda = 40$. For reasons to be discussed below, a small level of structural damping was assumed in the second mode: $\zeta_2 = 0.01$. The location of the Hopf bifurcation was computed to be at $\lambda = 17.61$, which was consistent with full-order analysis, which brackets the bifurcation point between $\lambda = 17$ and $\lambda = 18.5$. At the bifurcation point, the imaginary component of the critical, complex pair was 0.683 radians per time unit, which corresponded to a period of 9.20 for the neutral mode. (Fully developed LCOs at and below $\lambda = 18.5$ were not computed with full-order analysis owing to the very large computational times necessary to capture these lightly damped solutions.)

LCO solutions are shown in Fig. 29 for ROM solutions computed with $\Delta t = 0.05$, a time step 10 times larger than that permitted (i.e., by stability) for integration of the full-order system. ROM solutions were in excellent agreement with the full-order results for λ less than about 40. The ROM was found to be inaccurate when $\Delta t \geqslant 0.1$. For these large time steps the natural response of the second structural mode did not appear to be properly resolved, thereby permitting the

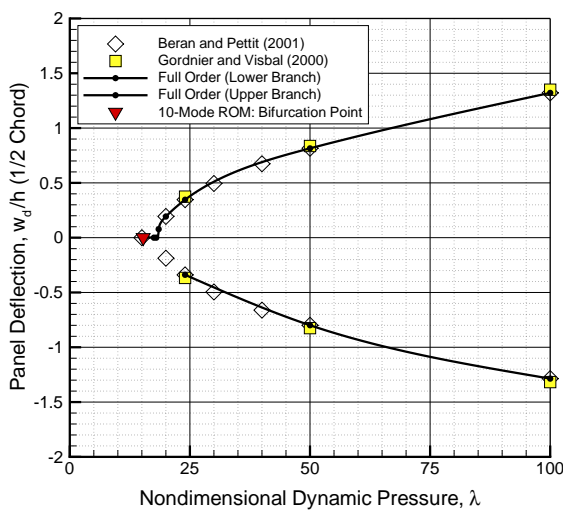Fig. 28. Bifurcation point directly computed with the ROM method for Mach 0.9 ($\lambda \approx 15.28$) and non-trivial solution branches.
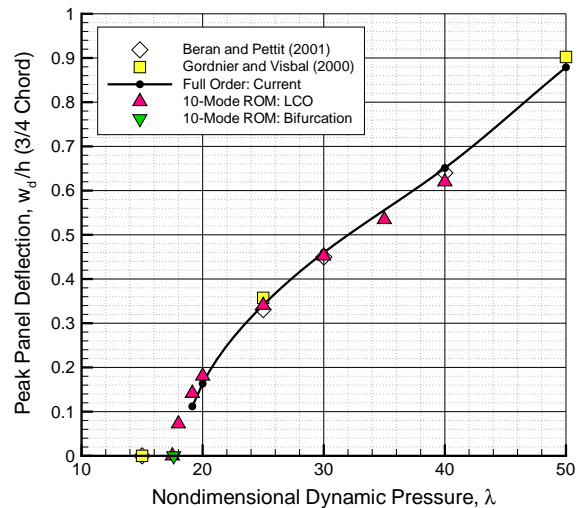

Fig. 29. Comparison of peak deflections at 3/4-chord location for full-order ($\zeta_2 = 0$) and reduced-order ($\zeta_2 = 0.01$) models for Mach 1.2, including ROM-predicted bifurcation point at $\lambda = 17.61$.

sustainment of a high-frequency error (approximately 10% of the base LCO amplitude).

Time histories of deflections predicted with the 10-mode ROM (constructed for $\lambda = 25$) compared reasonably well with those obtained using full-order analysis. Results are presented in Fig. 30 for a subcritical case, $\lambda = 10$, and in Fig. 31 for a supercritical case, $\lambda = 25$, the value of λ at which the ROM was constructed. In the supercritical case, LCO amplitude and frequency were in excellent agreement, although at large times, there was a slight accumulated phase shift
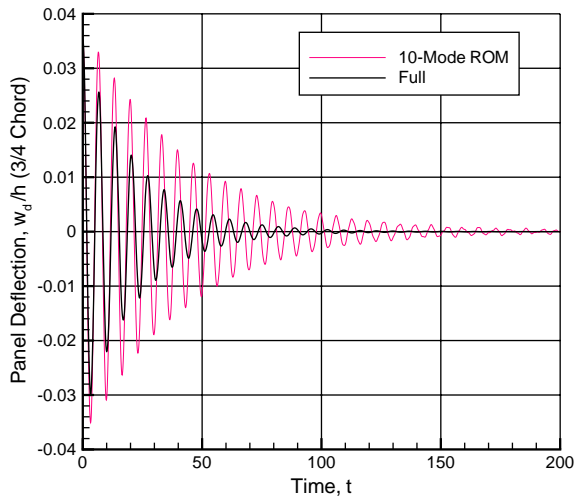
Fig. 30. Comparison of full-order ($\Delta t = 0.005$) and ROM ($\Delta t = 0.05$) time histories of 3/4-chord panel deflection at Mach 1.2 and $\lambda = 10$.
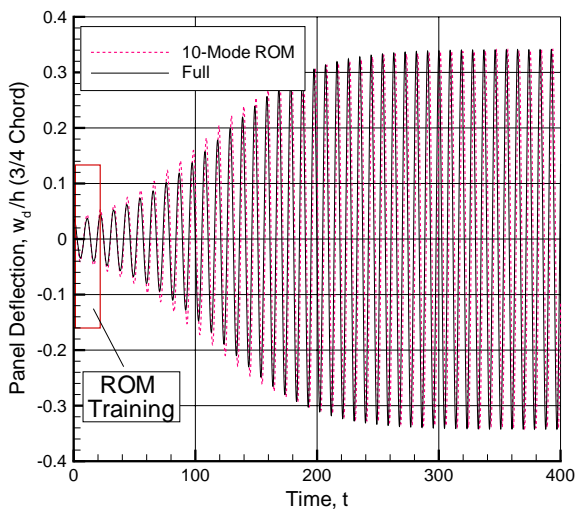
Fig. 31. Comparison of full-order ($\Delta t = 0.005$) and ROM ($\Delta t = 0.05$) time histories of 3/4-chord panel deflection at Mach 1.2 and $\lambda = 25$.

error. When λ was decreased to 10, the aeroelastic system was stable, as predicted by both full-order and reduced-order analysis. However, the ROM solution had a lower level of damping than desired.

The aeroelastic system was analyzed with greater computational efficiency using the ROM. The full-order system was analyzed in about two CPU hours (a simulation of 400 time units), while the reduced-order system was time-integrated in about one quarter of the time. The location of the Hopf bifurcation point was predicted even more efficiently in about two CPU minutes. The cost of constructing the ROM was relatively small, approximately one-twentieth that of the complete full-order simulation. Once the ROM was constructed, it could be applied over a fairly wide range of dynamic pressures without change.

4.4.3. Supersonic panel LCO with POD-Volterra

The work of Beran et al. summarized above relied on subspace projection for time integration of the ROM. Time integrating POD/ROMs with subspace projection produced about one order of magnitude improvement in compute time to accompany four orders of magnitude drop in problem order. While able to provide a very efficient computation of the Hopf bifurcation point, subspace projection was not an efficient way to time integrate the low-order, aeroelastic ROM.

The hybrid Volterra-POD method described in Section 2.4 was developed to achieve computational savings on the order of DOF reductions for time-accurate, nonlinear calculations with POD. Lucia et al. [109] applied this approach to the same problem just described (i.e. an elastic panel in supersonic cross flow), and the results are summarized below. In comparison to the use of subspace projection from this problem, the Volterra-POD method provided a more computationally efficient ROM.

POD basis functions were formed from snapshots obtained during the initial build-up of LCO, and with a fixed value of dynamic panel pressure ($\lambda = 25$). This procedure was the same POD training procedure used in Beran et al. [55] and described in the previous section. The full-system model was impulsed using the structural velocity and position modes. The flow field was projected onto the POD modes to determine the modal amplitudes, and a linear, state-space realization for the fluid dynamics was synthesized from the modal impulse responses using ERA. The fluid and structural models were tightly coupled to form the aeroelastic ROM as described in Section 2.4. Two cases were considered. The first case used uniform flow as the base flow term $\mathbf{W}_0$ from (13) about which perturbations were computed by the reduced-order fluid model. The second case used steady-state flow over the initial panel deflection as the base-flow term. Both cases resulted in ROMs that correctly predicted LCO behavior over a wide parameter

space; however, Lucia et al. concluded that uniform base flow was more desirable for predicting LCO onset. In addition, it was desirable to filter high-frequency information out of the impulse response data by computing the realization with relatively large time steps.

For the results that follow, the Galerkin panel model contained four modes for a total of eight DOFs. The panel dynamic pressure λ was treated as a parameter and was varied to produce a variety of panel LCO amplitudes.

4.4.3.1. Time history. Both the uniform flow (also called slug-flow) base case and the steady-state base case Volterra-POD ROMs, were time-integrated using $\lambda = 25$, and the results are shown in Fig. 32. Both cases correctly produced LCO, but the steady-state base case was more accurate in amplitude, frequency, and phase than the slug-flow base case. The 3/4 chord panel-amplitude was muted by 9% for the steady-state base case, and magnified by 25% for the slug-flow base case. The phase and frequency error were negligible for the steady-state base case, but the larger amplitudes of the slug-flow base case introduced a small increase in LCO frequency (resulting in an accumulating phase error).

The improvement in performance associated with the steady-state base flow was most likely due to the choice

of data windowing parameters used in the ERA realization. No substantive differences were identified in either the POD modes or the impulse response of the full-system flow-field between either case. Data windowing parameters were selected to provide a realization whose impulse response closely matched the original impulse data. Reducing the size of Δt introduced high-frequency dynamics into the realization. The high-frequency data in the impulse response was not germane to the large-time behavior of the aeroelastic system, and its inclusion resulted in a less accurate ROM under aeroelastic conditions.

4.4.3.2. ROM robustness. Both aeroelastic ROMs were time-integrated using a variety of panel dynamic pressure values (λ). The intent was to explore the predictive accuracy of the Volterra-POD ROMs across a nonlinear parameter space. Both ROMs were trained at $\lambda = 25$ (as described earlier), and robustness was defined as the ROM's ability to predict panel amplitude (at the 3/4 chord position) in fully developed LCO across the parameter space including non-LCO cases.

The ROM results are compared with full-system results and other results from the literature [157] for the same problem in Fig. 33. The steady-state base case ROM was better suited to large LCO amplitudes where the larger panel amplitudes excited a panel nonlinearity that corrupted the results of the slug-flow base case.
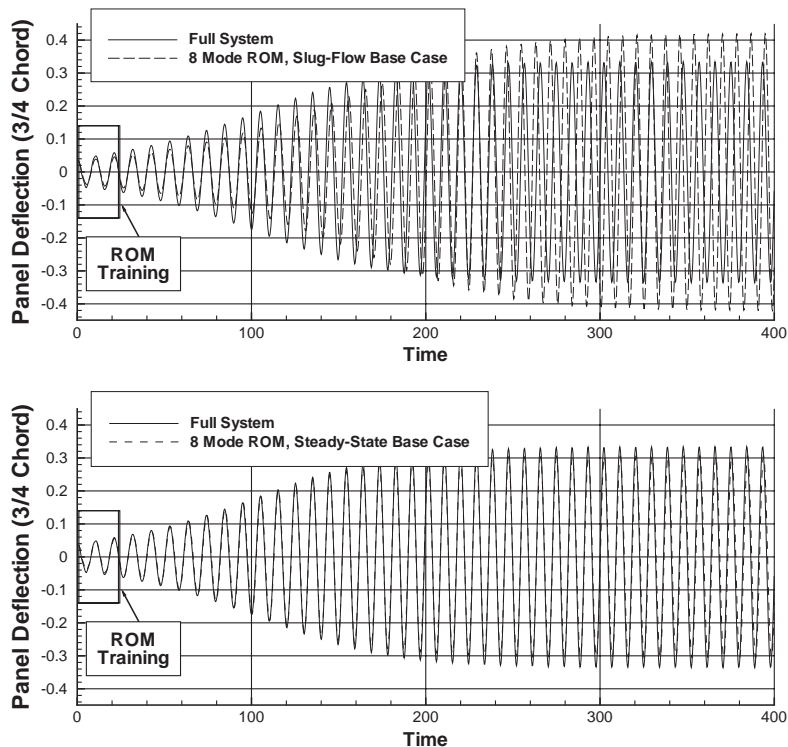

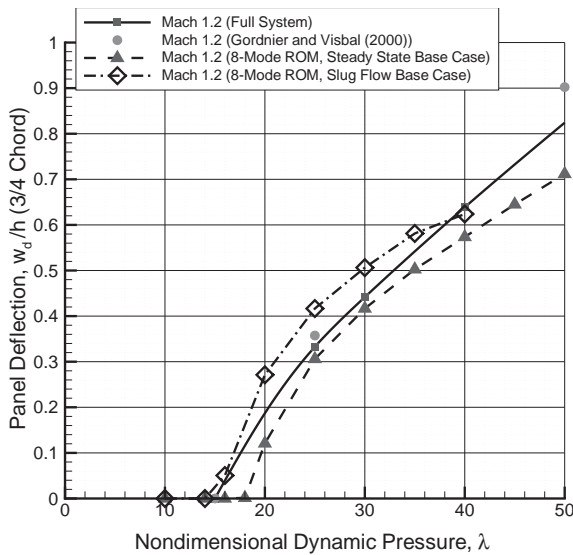Fig. 32. Panel deflection (w_d/h) time history, $\lambda = 25$, Mach 1.2.

Fig. 33. Panel response versus dynamic pressure.

Conversely, the use of slug flow as the base-flow term permitted a more accurate prediction of LCO onset at the lower values of λ. A non-LCO solution for the slug-flow base case occurred when $\mathbf{Y}_f = \mathbf{0}$ and $\mathbf{Y}_s = \mathbf{0}$, but the use of steady-state flow over an initial, non-zero value of $\mathbf{Y}_s$ required a non-zero value of $\mathbf{Y}_f$ to produce $\mathbf{Y}_s = \mathbf{0}$. The steady-state base case had difficulty producing this result. In addition, the small panel amplitudes near LCO-onset did not excite the high-frequency errors in the slug-flow base case that were evident at larger values of λ.

Finally, the Volterra-POD approach produced a stable and accurate aeroelastic ROM with four orders of magnitude reduction in problem order and computational expense. In this analysis, it took 6.2 h (wall-clock time) to produce 400 non-dimensional time units of data from the full-order solver. The POD-Volterra ROM required 8.1 s to yield the same results. The full-order solver contained 64400 DOFs, compared to 8 DOFs in the POD-Volterra ROM. The relative magnitude of the computational performance improvement was general since both the full-order solver and the ROM were run on the same computer, using the same programming language, input/output rates, and compiler options. The full-order solver in Section 4.4.2 was faster (only 2 hours instead of 6.2) because that analysis was done on a faster computer. Reduced-order modeling of the structure was also explored, and the results demonstrated that a single training event could produce adequate POD modes for both the fluid and structure. Future applications of this technique will involve very high-order, nonlinear structural models requiring order-reduction along with the fluid model.

4.4.4. Transonic panel LCO

The determination of aeroelastic behavior in the transonic regime is an especially demanding problem owing to the capture of essential nonlinearities in the aerodynamics in addition to structural nonlinearities. Lucia et al. [56] applied POD with domain decomposition and developed a ROM that successfully simulated transonic aeroelastic panel LCO, which involves correctly modeling a flow field with large shock motion. Domain decomposition enabled the use of POD for this case. The ROM was based on subspace projection and used a constrained optimization approach to link internal boundaries as described in Section 2.2.6. Time-accurate results were obtained using different time steps for each domain, and the reduced-order fluid model was coupled to the panel dynamics to provide an accurate reduced-order aeroelastic system.

A summary of the findings in Lucia et al. [56] follows. Two cases were considered: the first case used the full-order model in the domain section containing the moving shock (this case is referred to as the "Full-case"), and the second case included a POD based ROM of the shock region (this case is referred to as the POD-case). An 88% reduction in DOFs resulted in a 66% computational saving for implementations using the full-order model in the region of the flow field containing the shock. When POD was used in the shock region, there was almost three orders of magnitude reduction in DOFs (from 64,400 to 125). Both cases yielded accurate panel LCO and replicated correct motion of the transonic shock. In addition, both cases accurately modeled transonic LCO states corresponding to parameter values not used for POD training.

4.4.4.1. Domain decomposition. The solution domain was divided into sections to facilitate the use of POD with the moving transonic shock. Isolation of the transonic shock was the primary goal of the domain decomposition. The solution domain was divided into three regions to form the ROM. The geometric shape of the region did not influence the solver performance, so regions formed by the intersection of rectangles were used for simplicity. Since the transonic shock was always attached to the panel, the region of the flow field directly above the panel was identified as the shock region. The domain decomposition is depicted in Fig. 34. Domain decomposition also improved the computational performance because different time steps were employed for the different regions of the flow field to minimize the number of solver iterations [158,159].

Since the domain was divided into three sections, analysis for the ROM involved solving three smaller fluid problems that were linked by internal boundaries. Internal boundaries were handled with ghost cells which were filled with the corresponding values from the adjacent domain. Domain overlap was necessary when
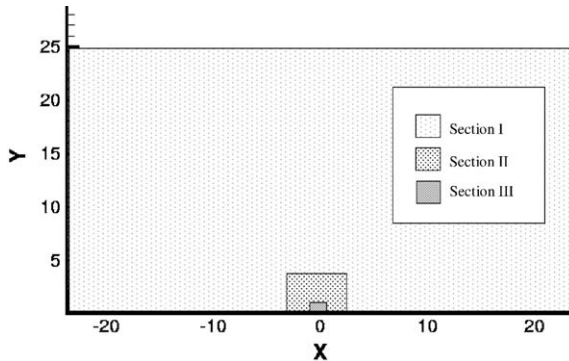
Fig. 34. Domain decomposition.

implicit solvers we used for the time integration. The domain decomposition approach produced flexibility in choosing the set of snapshots and number of modes used to create the ROM for each section.

4.4.4.2. Full-system transonic LCO. Variations in panel dynamic pressure (λ) constitute the parameter space of interest for the transonic panel analysis. Panel response at Mach 0.95 across this parameter space is illustrated in Fig. 35. For comparison, this figure contains data obtained from the literature for the same problem [103,157]. The maximum panel deflection amplitude at the $\frac{1}{2}$-chord point is shown for a range of λ. Fig. 35 illustrates how the upper static branch evolves into LCO, while the lower branch remains static when 1750 > λ > 2500.

With $\lambda = 2500$, the full-system simulation produced the transonic LCO shown in Fig. 36 and Fig. 37. A portion of the LCO cycle exhibits a moving shock [160]. The panel deflections corresponding to the portion of LCO containing a moving shock are shown in Fig. 36. The plot of C_P shows the shock motion progressing from subplot A to D. The dissipation in the first-order Roe's solver, which was used as the full-order solver for this research, slightly smears the moving shock. A stronger shock also develops at the end of the panel during this portion of the LCO. Because this was a stationary shock, it did not pose a significant problem for ROM development.

The upper portion of Fig. 37 shows the panel-deflection (denoted W(3/4)) time history at the $\frac{3}{4}$-chord point. Transonic LCO was established very quickly from a small panel deflection in free stream conditions. The initial panel deflection was a small, downward sinusoidal panel deflection of 1×10^{-3}. The LCO was well established by 15 time units, which was about half the period of a single panel oscillation. This extremely rapid LCO onset makes time integration an efficient implementation for analysis of this case. The bottom half of Fig. 37 is a phase plot of panel velocity (denoted S($\frac{3}{4}$)) and positioned at $\frac{3}{4}$ chord. Strong nonlinearities are
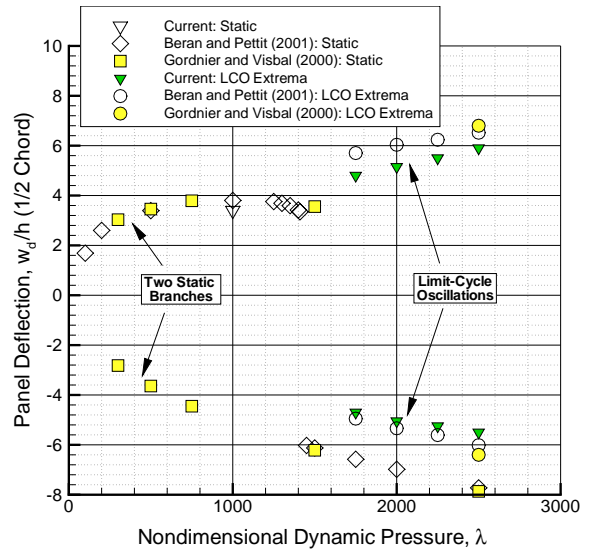

Fig. 35. Panel response with changing dynamic pressure.

evident in the upswing of the panel (at point I) and again after the crest at points II and III on the downswing. These nonlinearities appear as loops or peaks in the phase map.

4.4.4.3. Robustness. The panel phase plot in Fig. 38 demonstrates the ability of the ROM to capture nonlinear behavior at $\lambda = 2500$, which was the value used for POD training. When POD is used in the shock region, the flow field near the panel is constrained by the projection into the reduced-order space. The flow field does not damp high-frequency structural responses in the same way as the full-order flow field, which results in the differences between the full system and the POD-case responses on the phase plot. At Mach 0.95, LCO states exist for any value of λ greater than 1750 [103]. Only static panel deflections have been identified for $\lambda < 1750$. ROMs trained with snapshots from LCO at Mach 0.95 and $\lambda = 2500$ were able to model the LCO states at Mach 0.95; however, neither ROM could produce a static solution for $\lambda < 1750$. The snapshots contained data from an LCO flow field, and the subspace projection ROM could not produce a stable, static solution.

Next, the extendability of the ROM was explored. The POD basis from training at $\lambda = 2500$ (the same model used for results shown in Fig. 38) was used to model the panel response for $\lambda = 2000$. Referring to Fig. 35, this parameter variation encompasses $\frac{2}{3}$ of the LCO parameter space. No effort was made to optimize POD training for accuracy or robustness over the parameter space. This example demonstrates the robustness of POD in the presence of moving shocks with sub-optimal training.
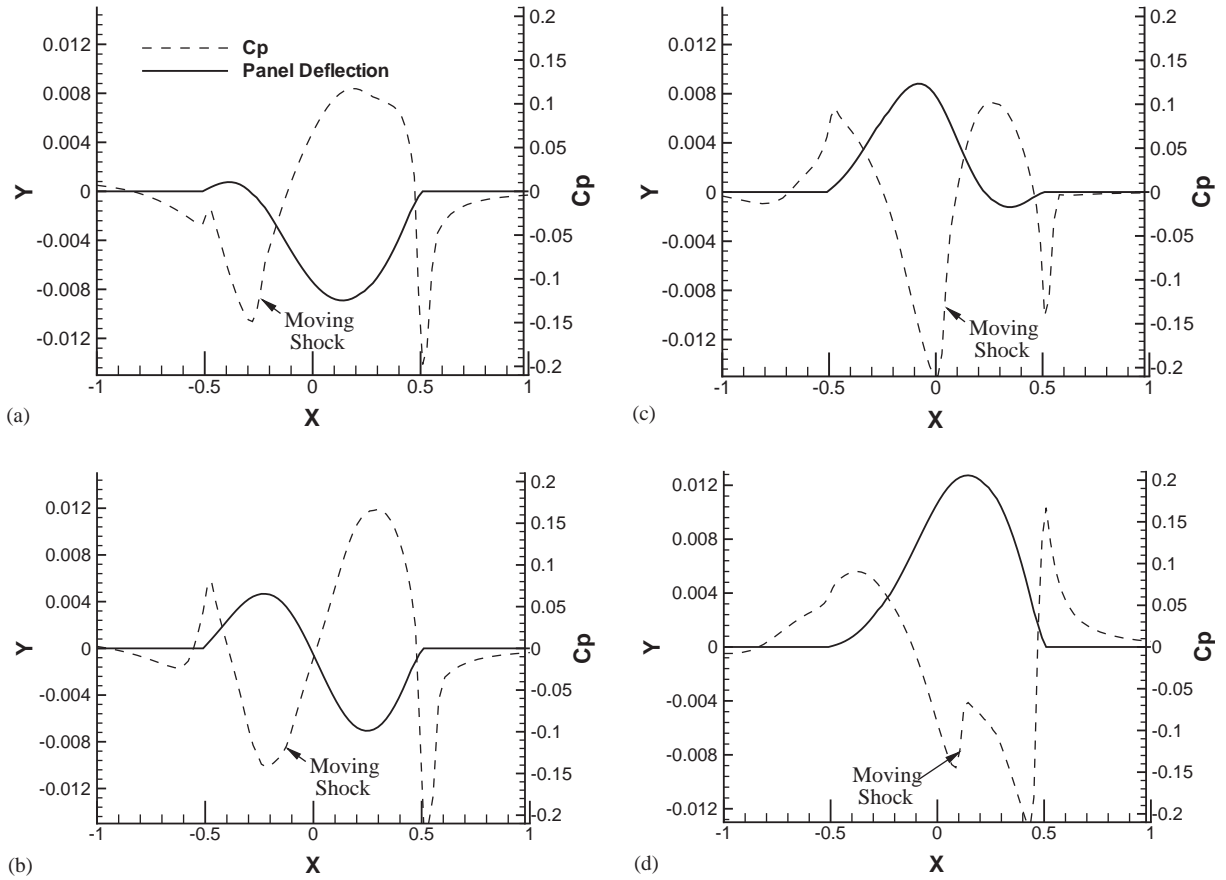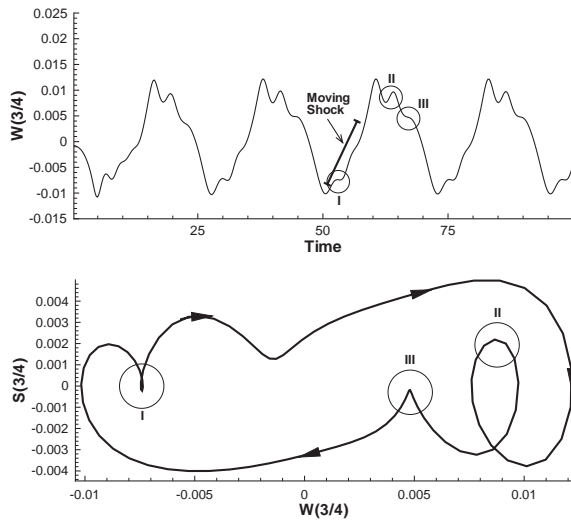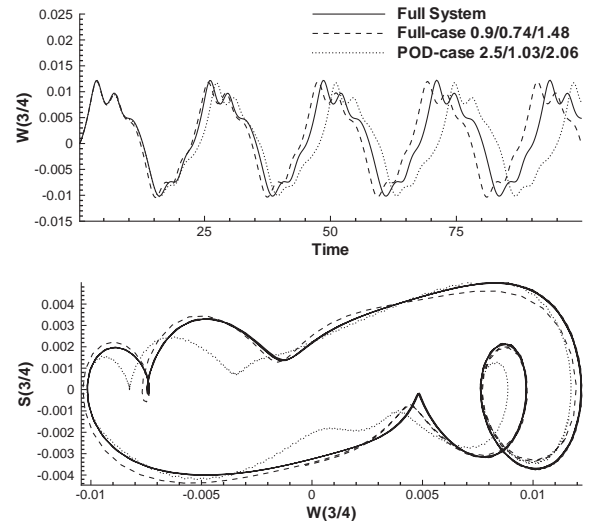
Fig. 36. Moving transonic shock.

Fig. 37. LCO onset.

Fig. 38. LCO for $\lambda = 2500$.

The panel response and phase plot for $\lambda = 2000$ is shown in Fig. 39. The full system LCO response at $\lambda = 2500$ is shown with a thick dashed line. At $\lambda = 2000$

the panel response is reduced, and the phase plot fits within the phase plot for $\lambda = 2500$. Both ROMs track this trend, while preserving the nonlinear panel behavior
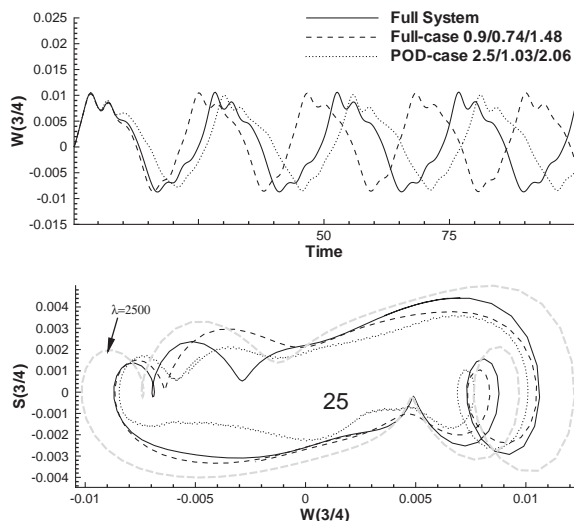
Fig. 39. LCO for $\lambda = 2000$ (trained at $\lambda = 2500$).

Fig. 40. Flow field error over a forced panel using deforming grids.

at the new value of λ. The extendability of POD across this large change in parameters using this simple, sub-optimal approach demonstrates the potential for future analysis of flows with moving shocks using this implementation.

4.5. Impact of grid deformation on POD efficiency

In another recently completed investigation, the accuracy of POD-based ROMs was assessed for unsteady problems using deforming grids [115,116,161,162]. Deforming grids are commonly encountered in aeroelastic analysis in response to structural deformation and pose additional research issues for ROM construction.

Anttonen et al. conducted an investigation on the accuracy of deforming grids on POD-based ROMs using an oscillating bump in 2-D subsonic channel flow [162]. This work was extend to a pitch and plunge airfoil application in a subsequent work [116]. The findings of these studies are summarized below.

4.5.1. Error assessment for an unsteady forced panel

Anttonen et al. [162] studied the effect of grid deformation on POD by applying the non-linear, discrete, full potential equation, in the simulation of unsteady flow over a forced, oscillating panel. POD accurately reproduced the flow field using a moving grid when the grid motion in the ROM computation corresponded closely to the grid motion observed in POD training. In this case, errors in fluid variables were less than 5% of the full-order system and thus represented a reasonable level of accuracy for design.

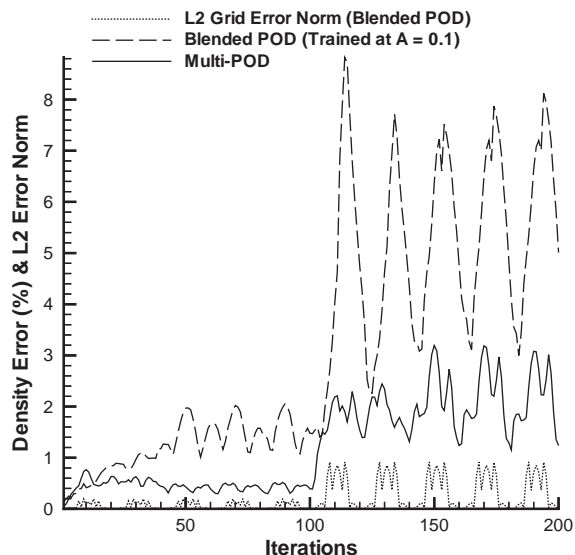The fluid ROM was trained at a certain panel oscillation amplitude, and ROM accuracy was degraded

when applied to a larger panel oscillation. Increasing the panel amplitude introduced grid deformations that were not included in POD training. A POD/ROM trained at 0.1 amplitude and run at 0.15 amplitude had maximum density errors of $\pm 12\%$.

Anttonen et al. developed the technique described in Section 2.2.7 to switch between multiple ROMs, each trained at differing levels of grid deformation. Using this technique, the most appropriate ROM for a given grid deformation was used to provide an accurate solution. The results of this technique (called ''Multi-POD'' by the authors) are shown in Fig. 40. Two ROMs, trained at panel oscillation amplitudes of 0.05 and 0.15, respectively, were used to model amplitude deflections from 0.05 to 0.15. In this example, the panel amplitude was 0.05 for five oscillations, then 0.15 for five oscillations. When compared to a single ROM (trained at an panel amplitude of 0.1 and denoted as ''blended'' in Fig. 40), the Multi-POD was more accurate. The density error of the single ROM exceeded 8% while the Multi-POD remained below 5%. The L_2 error norm clearly identified the point at which the algorithm changed ROMs as reflected in the sudden increase in the L_2 error norm plot.

4.5.2. Application on pitch and plunge airfoil

Anttonen et al. [116] extend the multi-POD approach to an inviscid 2-D flow over a pitching and plunging airfoil. This study used a NACA 0012 airfoil and a free stream Mach number of 0.5 to ensure subsonic flow over the airfoil. The airfoil motion was synchronized in both pitch and plunge, and the oscillation frequency was

non-dimensionalized based on the period c/U_∞ (where c is the chord).

A C-grid was used with a wake cut along the trailing edge that extended to the outflow boundary. The domain was discretized using 251×50 grid points, with 150 grid points evenly spaced on the airfoil surface. The grid deformation was based upon the location of the rigid airfoil, and the grid was re-formed at each time step using an elliptical solver. The elliptical solver used a tension spline to prevent grid line crossing.

Forced pitch and plunge cases were used to generate snapshots. Forced pitch angles varied from 0.0 to $\pm 2.0°$, and plunge depths varied from 0.0 to ± 0.2 chord. Oscillation frequencies for both pitch and plunge varied from 0.02 to 0.1. Both plunge, $h(t)$, and pitch, $\alpha(t)$, were modulated using sine waves. The pitching and plunging were synchronized, with the pitch angle zero at minimum and maximum deflection. For oscillation frequencies below 0.04, the flow was nearly quasi-steady. The flow was non-linear in higher frequencies, due to compressibility. In addition, increased plunge depths also produced compressibility because plunge depth defined the relative speed of the airfoil for a given frequency.

Free response in pitch and plunge was also considered. Free response started with a steady-state flow field and an initial pitch angle $\alpha = 1.0°$. The motion of the airfoil in the free case was based on a 2-D structural model.

The multi-POD technique was shown to be effective for the 2-D pitching and plunging airfoil. In Fig. 41, errors in airfoil AoA were less than 6%. For these results, the multi-POD was formed using three ROMs. The results without multi-POD are also shown in Fig. 41. A single ROM trained using the same variety of pitch angles and frequency but only one plunge depth was unable to correctly track the airfoil motion (denoted as "blended" in Fig. 41). The grid error norm from (58) was able to identify the ROM best suited for the grid deformation, which accurately reproduced the airfoil motion.

4.6. POD analysis of two-phase flows

Beyond aeroelastic applications, POD has been used by a number of investigators to develop ROMs of low order for the study of various nonlinear phenomena. One noteworthy example is the work of Cizmas et al. [163], which involves the construction of ROMS for two-phase flow, heat transfer and combustion in dense or dilute fluid-solids flows. Cizmas et al. [163] used a two-fluid hydrodynamic model to simulate a two-dimensional bed filled with sand particles. This bed was uniformly aerated across the bottom at minimum fluidization. The fluidized bed was $40\,cm \times 60\,cm$ of $500\,\mu m$ particles. Additional air was injected through a central nozzle to produce a jet. POD was used to extract the dominant spatial features directly from the numerical simulations. Because of the central jet, the motion of the bed was most significant in a central channel. The gas-particle flow within this structure was successfully captured by a few POD eigenfunctions, approximately six modes. Reconstructions with more modes captured higher-dimensional features such as flow along the sides of the channel.

Results obtained by Cizmas et al. demonstrated the ability of POD to capture efficiently the energy content in a gas/solid mixture. The governing transport equations were much more complex than the Navier–Stokes equations; three gas and three solids equations
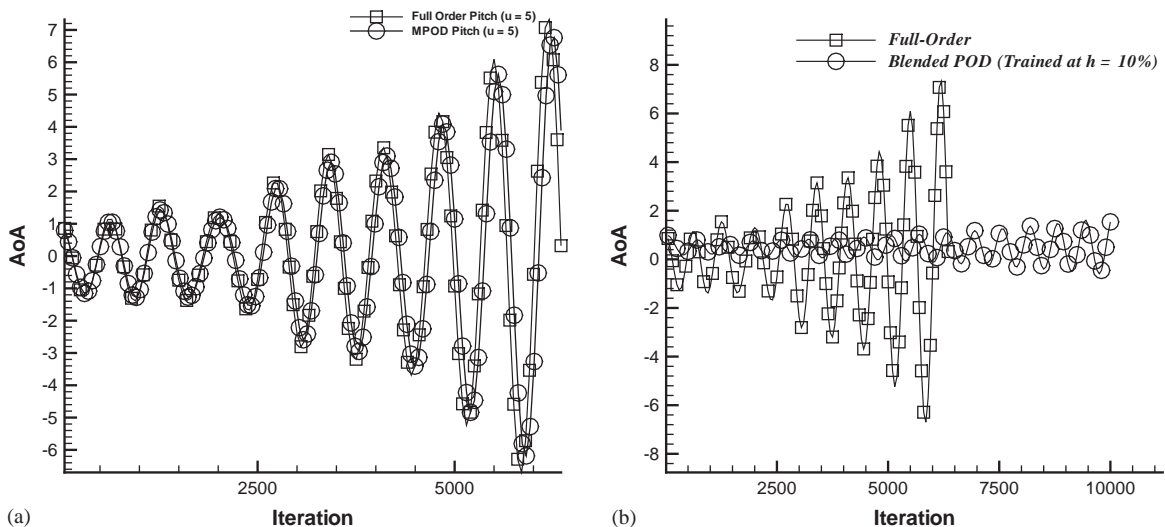

Fig. 41. Airfoil pitch accuracy with deforming grids. (a) Multi-POD and (b) ROM trained using a single grid deformation.
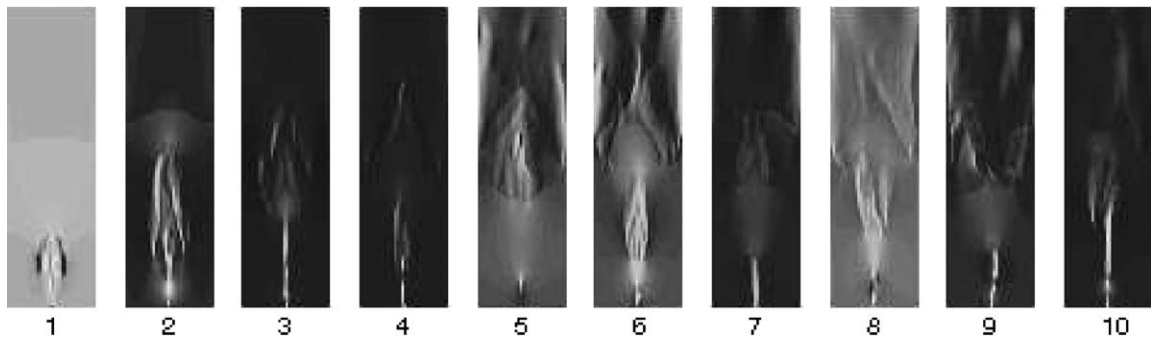
Fig. 42. Snapshots of gas velocity in the *y*-coordinate direction at 10 equally spaced time instants of a gas/solid mixture (from Cizmas et al. [163] with permission).

comprised the set. Illustrated in Fig. 42 are 10 snapshots of the *y*-component of velocity taken at equal intervals in time that partially represent the ensemble of snapshots over all system variables. The snapshots are used in the computation of 20 POD modes for this component of velocity that account for 80% of the system energy (ratio of sum of retained POD eigenvalues to sum of all POD eigenvalues).

The time-average and the POD modes of all representative variables had a channel structure to which the main flow motion was confined. Computer animations of the reconstructed flow with increasing numbers of POD modes, from one to ten (including the time-average), were performed and compared with the original simulations. Visual inspection of these animations reproduced the overall motion through the middle of the channel structure. For example, Fig. 43 shows a time snapshot of various reconstructions with successively higher-order POD modes. As the number of modes increased, each individual reconstructed image showed less reflectional symmetry. In addition, high-dimensional features, such as flow motion along the sides of the channel, became more visible. In the particular case of gas pressure, P_g, the time-average and the first four POD modes revealed a layer structure with different pressure values that ran from the bottom to the middle of the bed. The simulations were carried out outside the bubbling regime. However, a careful examination of POD reconstructions indicated that the circular features that appear in some of the modes were physically related to the burst of gas pressure that emanated from the nozzle located at the bottom-center of the bed. Both the channel structure of the flow and the layer structure of gas pressure were consistent with reported experimental work [164].

The results indicated that a low number of POD modes could capture the overall characteristics of the flow that appeared to be confined to a central channel formed from the bottom to the top of the bed. Phase-space plots (not shown here) further illustrated the

existence of a low-dimensional attractor with approximate reflective symmetry.

5. HB results

In this final results chapter, we describe results obtained with the HB technique of Hall et al. A significant body of successful aeroelastic analysis has been reported using HB. We focus on the transonic work accomplished at Duke University, which is rapidly progressing to 3-D analysis of complex geometries. We also describe results from Maple et al. on a 1-D moving shock problem.

5.1. Transonic aerodynamics with HB

We begin with a summary of stability results obtained for a front-stage rotor in viscous flow using the HB technique. Hall et al. consider the flowfield near the tip of a front-stage rotor for a high-pressure compressor [60,165]. The flow is modeled as two dimensional and the configuration is treated as an infinite blade row by imposing a suitable periodicity condition. The inlet Mach number is specified to be 1.27, and the governing equations are the Navier–Stokes equations, closed with the Spalart–Allmaras turbulence model [166]. A baseline grid of H-O-H topology with 193×33 points is found to produce grid-converged results. The complexity of the steady-state flowfield is captured in Fig. 44, where shock–shock and shock–boundary layer interactions occur.

Time-periodic unsteadiness is introduced by Hall et al. in the rotor flowfield by oscillating the rotors in pitch about their midchords with a reduced frequency of 1. While they report many results, we summarize their findings for the imaginary component of the first harmonic of the unsteady surface pressure, which has implications for aeroelastic stability [60]. Variations with respect to two parameters are examined: the pitch amplitude ($\bar{\alpha}$) and the interblade phase angle (σ).
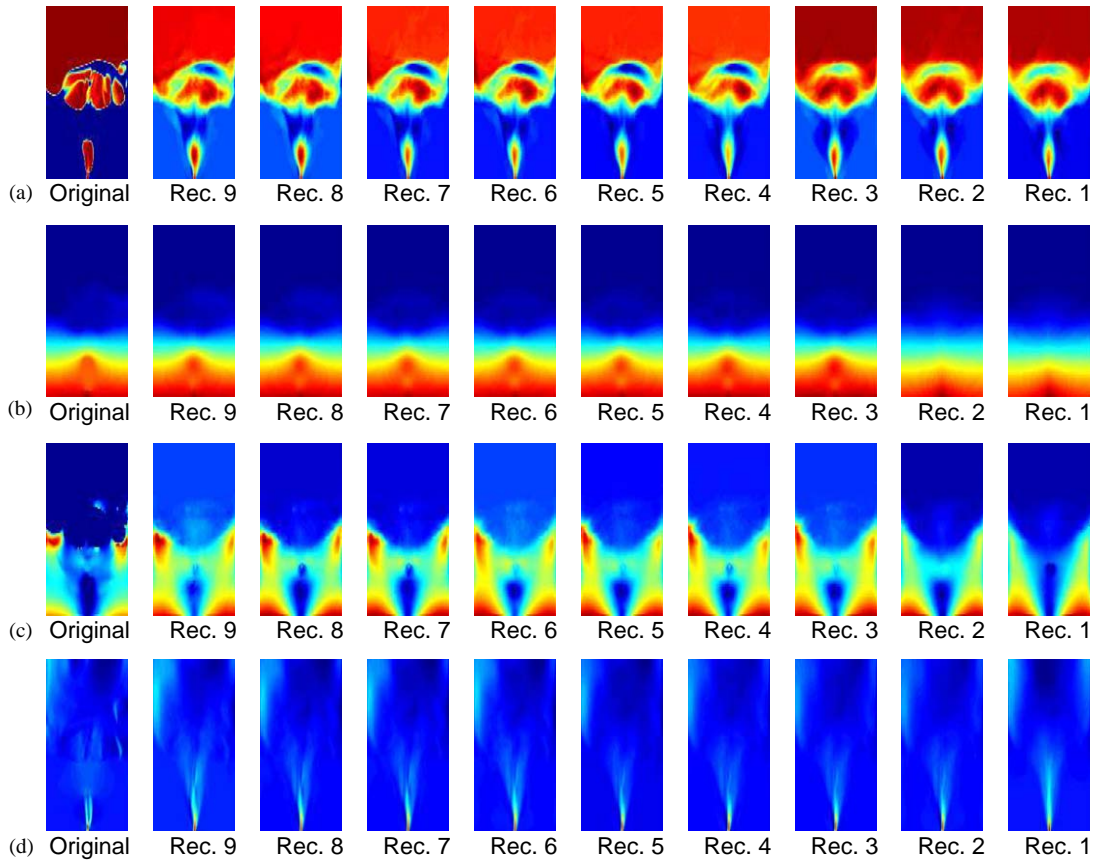
Fig. 43. Sequence of reconstructions (Rec.) with successively higher-order POD modes. Time is held fixed at $t = 100$. Level of detail increases from right to left (from Cizmas et al. [163] with permission). (a) ϵ_g, Volume fraction of fluid phase; (b) P_g, gas pressure; (c) P_s, solids pressure and (d) v_g, gas velocity along the y-axis.

Pressure is nondimensionalized by inlet dynamic pressure (q_{inlet}), airfoil chord (c), and $\bar{\alpha}$ (to better display nonlinear effects). For $\sigma = 30°$, first harmonics of the unsteady pressure distributions are shown for different values of pitch amplitude and numbers of retained harmonics (N_{HB}) in Fig. 45. The first harmonic solution is rapidly convergent in N_{HB}, with five harmonics being sufficient to capture all details of the unsteady pressure distribution. Nonlinearity arises with increasing $\bar{\alpha}$ and is particularly noticeable when $\bar{\alpha}$ reaches $1°$ near a normalized airfoil surface position of 0.4. At this location, the unsteady pressure spike spreads out, a result of shock movement about this point [60].

Variation of the imaginary part of the first harmonic of the pitching moment yields a more dramatic indication of the role of nonlinearity. Blade stability is achieved when this component of the integrated pitching moment is negative for all values of σ [60]. Results are displayed in Fig. 46, which shows that nonlinear aerodynamics serve to stabilize the flow when $\bar{\alpha}$ is increased to about $1°$.

The HB scheme is reported to be highly efficient, an order of magnitude faster than conventional time-accurate, time-integration schemes [60,165]. Converged results are found when five harmonics are retained, at a computational cost 7.5 times larger than that of steady-state analysis per iteration. Convergence to a numerical solution is not obtained with the HB method when N_{HB} is increased to 7. The authors believe this instability is associated with the longest wavelengths, not the shortest wavelengths that cause most instabilities in CFD solvers. The Fourier stability analysis that predicts asymmetric stabilities for non-zero frequencies assumes short wavelengths and therefore does not include far-field boundary effects. The authors' numerical experiments show the far-field boundaries have a stabilizing affect on the solver; however, if the frequency is too large (i.e. for the higher harmonics such as $N = 7$), the stabilizing affect of the boundaries is not sufficient. This instability is not serious, since a smaller number of harmonics ($N = 5$ or less) is sufficient for the envisioned applications of the method.
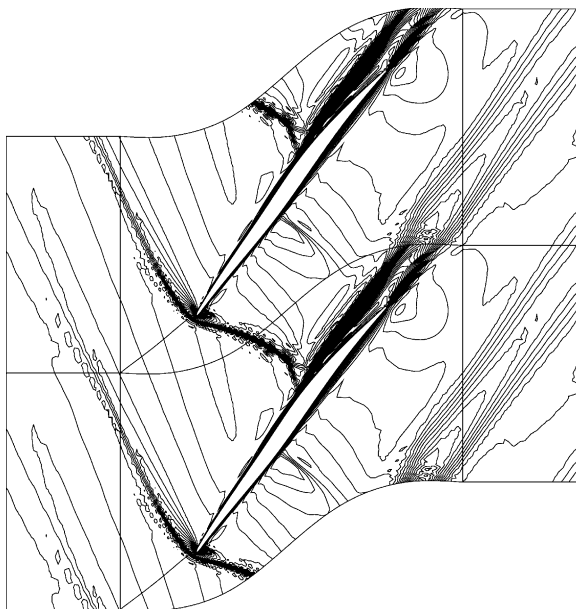
Fig. 44. Computed Mach number contours for transonic viscous flow through front stage compressor rotor (from Hall et al. [60] with permission). Two instances of spatially periodic flowfield shown for clarity.

Thomas et al. [77,167] have also applied the HB scheme to the study of LCO in airfoils with structural coupling in the transonic regime, both inviscid and viscous [168] flows. For the inviscid case, an unsteady transonic flow was coupled to a linear structural dynamics model. Both one and two DOF flutter models were studied. Nonlinear aerodynamic effects were found to produce a favorable divergence trend, an unstable LCO solution for the single-DOF flutter model, and stable LCO for the two-DOF flutter model [167]. Viscous effects were shown to significantly influence LCO trends when compared to an inviscid analysis. Shock induced boundary layer separation led to a more gradual rate of increase in LCO amplitude relative to the inviscid analysis [168]. In other recent work soon to be published, Kholodar et al. have applied HB for parametric investigations on a transonic airfoil. Parameters included in these investigations consist of free-stream Mach number, structural-inertial parameters, and mass ratio. This work is important in unraveling the role of moving shocks in the phenomenon of LCO.

Finally, Thomas, Hall and Dowell have successfully applied HB to three dimensional, unsteady transonic analysis. Their analysis of LCO characteristics of the AGARD 445.6 wing, in both inviscid [169] and viscous [170] transonic flow conditions is summarized here. The AGARD wing configuration is depicted in Fig. 47. The configuration consists of a $45°$ quarter chord swept wing based on a NACA 65004 airfoil section. The aspect ratio is 3.3 and the taper ratio is 2/3.
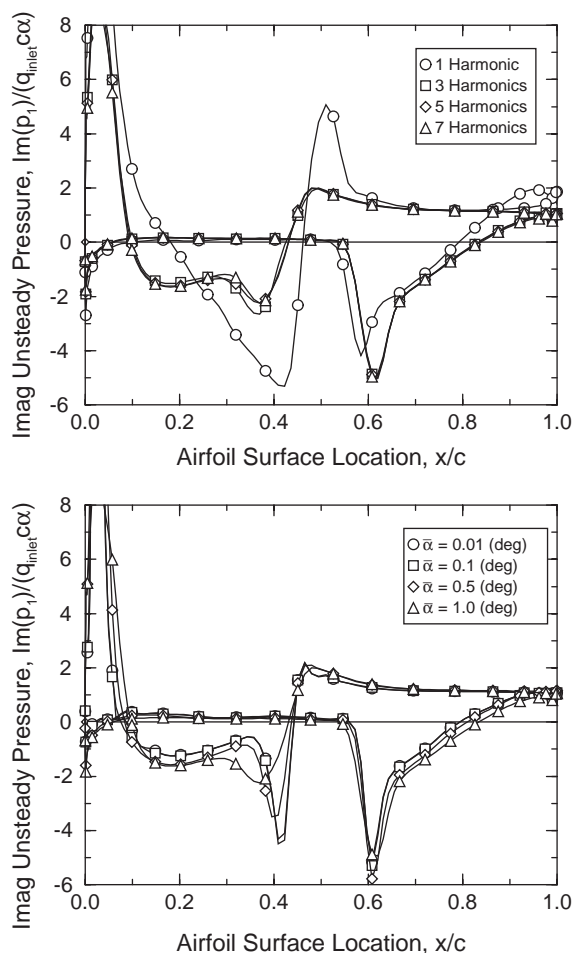

Fig. 45. First harmonic of unsteady pressure distribution for front stage compressor rotor airfoils vibrating in pitch. Top: variation of number of retained harmonics for pitch amplitude of $1°$. Bottom: variation of pitch amplitude for $N_{HB} = 5$ (from Hall et al. [60] with permission).

The LCO solution procedure employs HB, and the reader is referred to [169] for a detailed development. The LCO trends for the AGARD 445.6 wing are shown in Fig. 48 for six different Mach numbers. Shown is the LCO amplitude of the first structural mode versus the reduced velocity for each Mach number. The data point for what appears to be a zero LCO amplitude is actually a very small LCO amplitude of 0.0001. Note how the LCO trends are nearly vertical. This is indicative of linear aeroelastic LCO response, which is expected for a thin wing (maximum thickness ratio of 4%). The LCO characteristics observed using the HB technique are consistent with higher-order computational results from Gordnier and Melville [171].

For the viscous case, Fig. 49 shows LCO solutions for viscous and inviscid flow models at $M_\infty = 1.141$. The beginnings of a stable nonlinear LCO trend is apparent
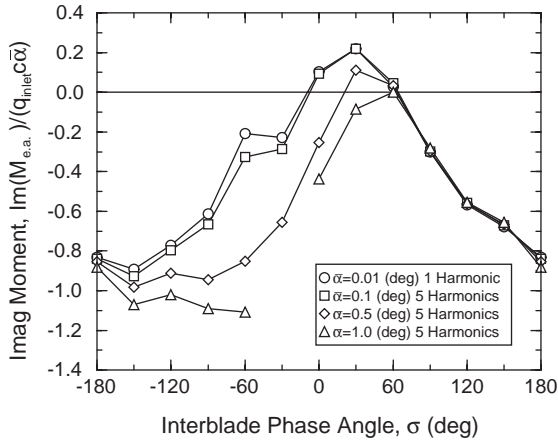
Fig. 46. Imaginary part of first harmonic of the blade pitching moment as a function of interblade phase angle (from Hall et al. [60] with permission).

for the viscous flow model for very small amplitudes. Linear aeroelastic behavior is evident at large amplitudes of the inviscid model. The effect of viscosity on large amplitude LCO is still under investigation by the authors at Duke University.

5.2. Adaptive HB applied to a quasi-1D nozzle

Finally, we summarize the results of Maple et al. [79] where the adaptive HB technique from Section 2.3.2 was applied to a quasi-1D nozzle problem (Fig. 50). A common steady-state quasi-1-D nozzle test case [172] was modified to generate an unsteady flowfield. Assumed conditions at the inlet were: Mach number = 1.5, density = 0.002241 slugs/ft^3, pressure = 2000 lb$_f$/ft^2, and temperature = 520R. Unsteadiness was introduced by adding a sinusoidal variation to the exit density:

$$\rho = 0.003954 + 0.0001 \sin(\omega t) \text{ slugs/ft}^3. \tag{80}$$

For computation, all properties were non-dimensionalized by the inlet values.

Without the unsteady term in the exit density, these boundary conditions resulted in a flow field with a normal shock near the midpoint of the nozzle and subsonic exit flow [172]. With the addition of the specified unsteadiness at the exit, the flow behind the shock became continuously unsteady but remained subsonic. The location of the shock oscillated about its steady-state location, while the supersonic flow ahead of the upstream limit of shock motion was not affected and remained steady.

A typical growth history of an adapted frequency distribution is shown in Fig. 51. The figure shows the adaptation history for a solution on the finest grid with an augmentation threshold of $5.0e-7$. The *y*-axis
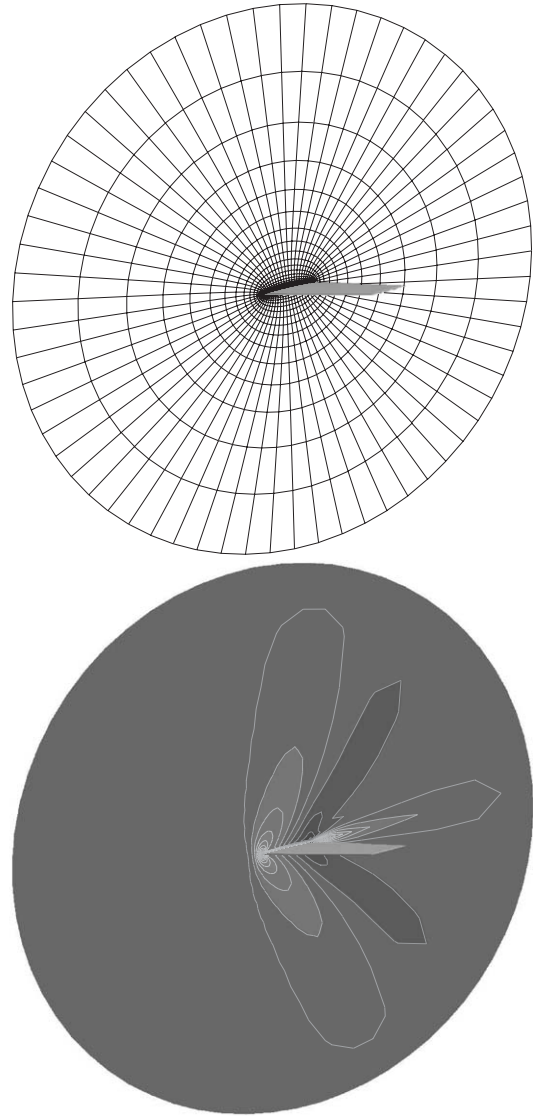

Fig. 47. AGARD 445.6 wing viscous case wing Top: Grid topology, Bottom: Mach contours for $M_\infty = 1.141$ (from Thomas et al. [170] with permission).

represents the number of harmonics included for a particular cell location. Each frame shows the frequency distribution after frequency augmentation at the indicated iteration from the first adaptation at iteration 4725 to the final adaptation at iteration 16,990. As the figure shows, the frequency distribution had stabilized outside the shock region by the fourth adaptation. Subsequent adaptations added frequencies only to the region of shock motion.

In Fig. 52, pressure distributions for the final adapted solution from Fig. 51 are shown at 10 snapshots in time spanning one period of the flow oscillation. Also shown are snapshots from a time-accurate calculation on the
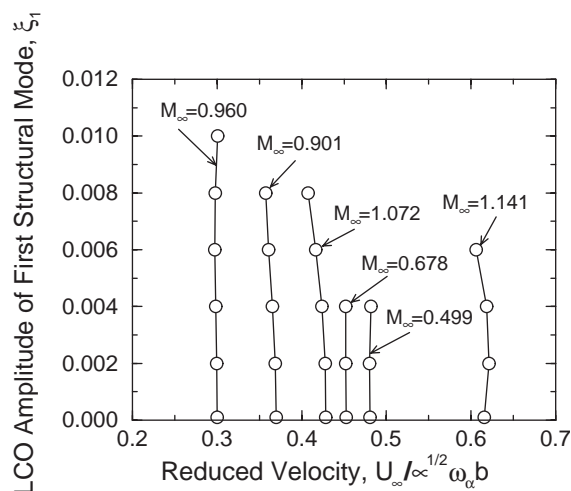
Fig. 48. Computed AGARD 445.6 wing configuration LCO trends (inviscid results) (from Thomas et al. [169] with permission).
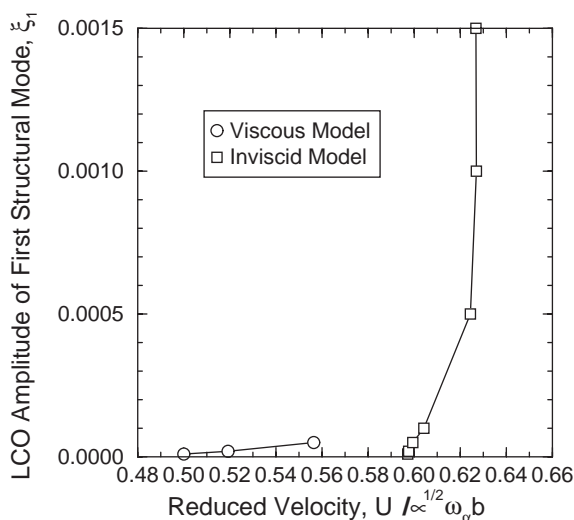

Fig. 49. Computed AGARD 445.6 wing configuration LCO characteristics. $M_\infty = 1.141$, and $Re_\infty = 860,000$ for the viscous case (from Thomas et al. [170] with permission).
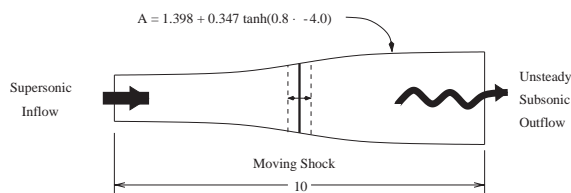

Fig. 50. Unsteady diverging nozzle configuration (from Maple et al. [79] with permission).

same computational grid along with the final frequency distribution envelope. This figure illustrates how the number of frequencies included in the adapted solution

varies with local flow behavior. Fig. 52 also illustrates the ability of the adapted HB solution to sharply capture the oscillating normal shock and agree with the time-accurate solution at all points in time. The spatially varying frequency content produced no visible artifacts in the computed solution.

To determine the efficiency of the adaptive HB approach relative to non-adapted (fixed-frequency) HB, Maple et al. recomputed each of the HB solutions with a fixed number of frequencies. The maximum frequency content from each of the adapted solutions was used to generate the fixed-frequency solutions, ensuring that both solutions maintained the same fidelity. The efficiency of the adaptive method was examined by comparing problem sizes and compute times.

Augmentation threshold values greatly influenced the efficiency improvement. For the largest augmentation threshold, the reduction in problem size was approximately 45% for all grid densities, which represents a significant reduction, considering that the average number of frequencies in each solution was approximately one (the minimum possible number of frequencies for a frequency augmentation approach). Any improvement would require a frequency decimation approach, where frequencies are identified as unnecessary and removed from the solution. The problem size reduction was more substantial for the small thresholds, approaching 90% for the smallest threshold on the finest grid.

At a threshold of $5.0e - 2$, the overhead of the adaptation algorithm was significant relative to the maximum absolute run-time reduction on all grids, resulting in an average ratio (converted to percent) of 47%. For lower thresholds, the overhead was less significant, and ratios were higher, averaging 91% for a threshold of $5.0e - 6$ and 95% for a threshold of $5.0e - 7$. The adaptive solution on the finest grid with an augmentation threshold of $5.0e - 7$ achieved a ratio of 99% with an 86% reduction in compute time.

6. Concluding remarks

6.1. Volterra summary

The development of ROMs based on the time-domain version of the Volterra theory of nonlinear systems has been described including continuous- and discrete-time versions of the theory. The basic objective of the theory is the identification of linearized and nonlinear kernel functions that capture the dominant response features of a nonlinear system. Volterra theory is, in fact, a nonlinear Green's function method that provides a very natural and intuitive extension of well-understood linear phenomena into the nonlinear domain.
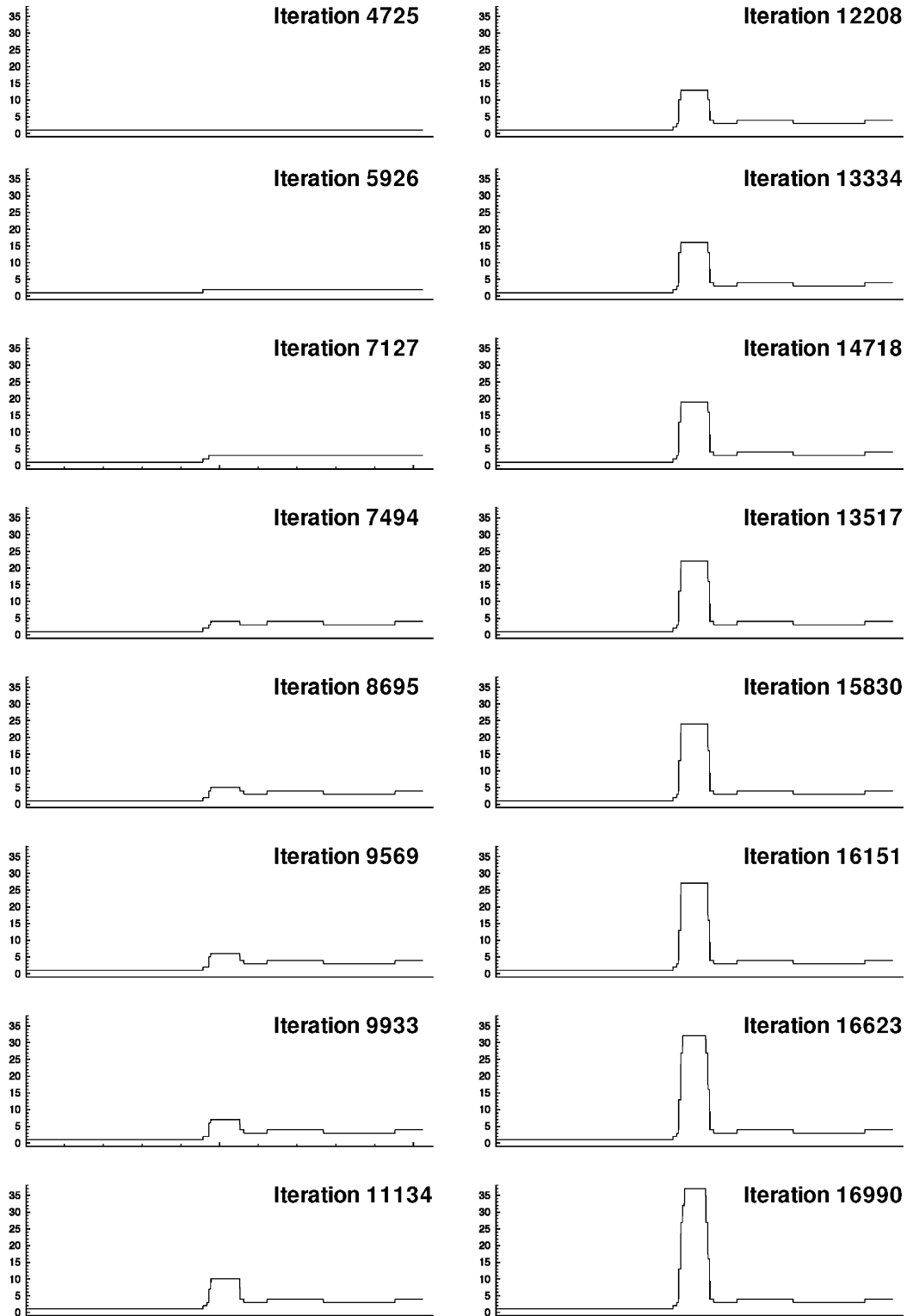
Fig. 51. Evolution of the adapted frequency distribution, 1024 cells, augmentation threshold $5.0e - 7$ (from Maple et al. [79] with permission).
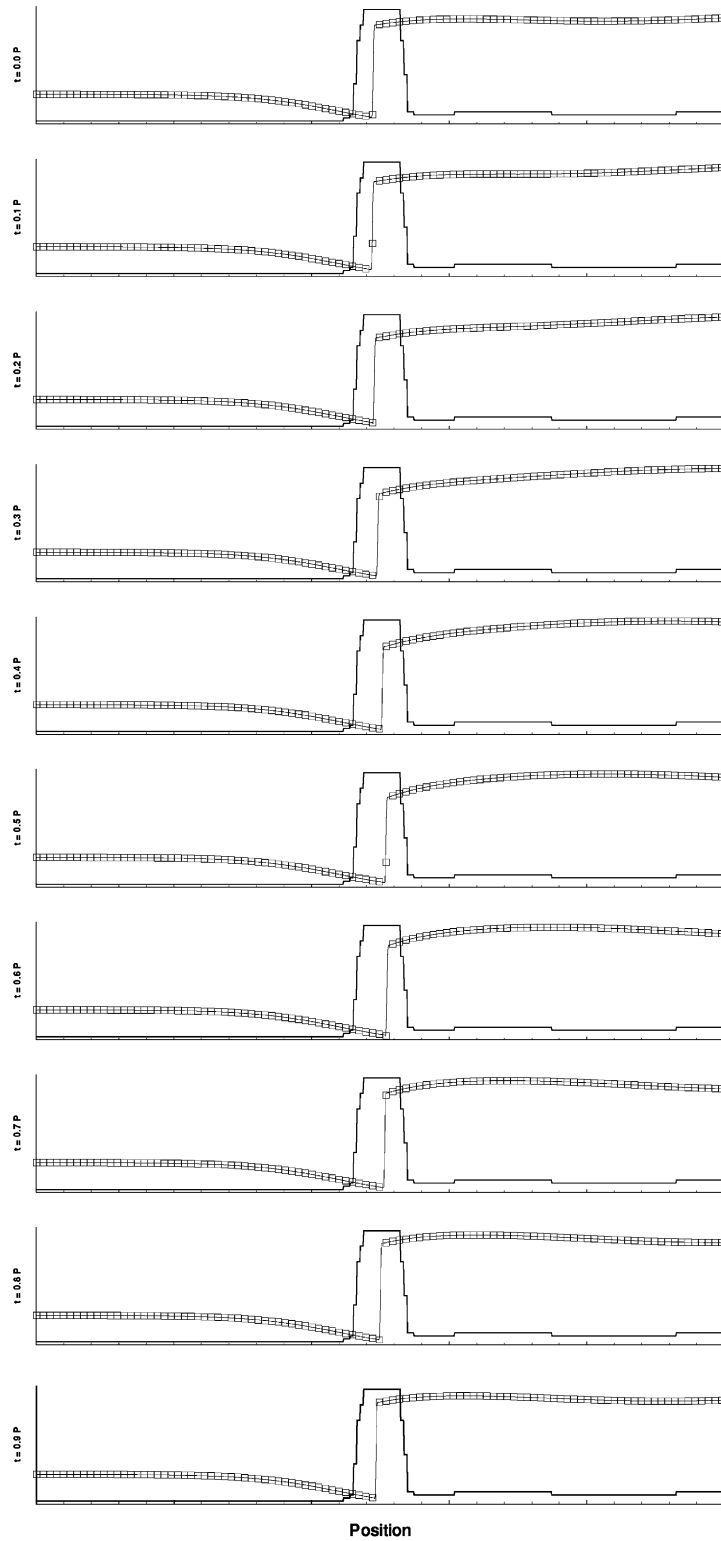
Fig. 52. Comparison of adaptive HB (symbols) and time-accurate solutions (solid) at 10 points in time spanning one period of oscillation, with adapted frequency distribution (heavy solid) (from Maple et al. [79] with permission).

In the fields of unsteady aerodynamics and aeroelasticity, the use of influence coefficient functions, such as aerodynamic influence coefficient (AICs) functions and structural influence coefficient (SICs) functions is routine. Since these influence coefficient functions are derived from Green's function concepts, the extension of these concepts into the nonlinear domain via the Volterra theory is quite natural and effective. In fact, these functions can be seen as a linear subset of a much broader nonlinear Volterra functional space.

While in its infancy for the analysis of large, spatially discrete systems, the Volterra method is currently under continued development. One of the encouraging applications presented is for a Navier–Stokes solution of a 2-D RAE airfoil in transonic flow using the CFL3D code with the Spalart–Allmaras turbulence model. First- and second-order kernels were computed for plunging motions of the airfoil. It was shown that the first-order kernel (that captures amplitude-dependent nonlinearities) was used successfully to predict the plunging response of the airfoil for large (nonlinear) plunging motions at a minute fraction of the cost of the full CFD solution. Another important result reviewed was an Euler solution of the AGARD 445.6 Aeroelastic Wing recently computed by Raveh et al. [14] using the EZNSS CFD code. It was shown that with pulse or step responses the full linearized frequency-domain GAF matrices were reproduced at a fraction of the time and cost than that required by standard techniques.

The status of the Volterra-based ROM approach can be summarized as follows. The method has been used to show that discrete-time concepts, indeed digital signal processing concepts such as unit pulses and step inputs, are directly applicable to CFD codes. The method has also been shown to be a higher-level generalization of the standard linear methods in use today. This finding is beneficial, because it means that industry experts do not need to restructure their analysis process in order to introduce Volterra-based methods into their design algorithms. In addition, the nature of the method requires minimal, if any, modification to the CFD code of interest. Most unsteady aerodynamic or aeroelastic CFD codes already have various excitation inputs (e.g., sinusoidal), and extension to a Volterra-based ROM approach simply involves adding a pulse (or step) input to the suite of available inputs—the CFD code itself remains unchanged.

As for the challenges associated with the Volterra-based ROM approach, much work must be done. An important issue that needs to be addressed is the issue of modal superposition with respect to nonlinear effects. Although it is clear that a mode-by-mode excitation is a linearization of the aeroelastic process, it is important to understand the limitations of this approach. In addition, work continues on the development of a technique that

provides simultaneous excitation to all modes, eliminating the linearization issue. Linearized state-space models are being developed using the CFD-based pulse responses. These state-space models can be incorporated directly into control system analysis, for example. These state-space matrices also sidestep the need to transform time-domain CFD loads into the frequency-domain only to transform the frequency-domain loads back into the time domain via rational function approximations. Using the Volterra approach, time-domain CFD-based information goes directly into creating time-domain state-space matrices, a more efficient process. But the ultimate challenge lies in the creation of nonlinear (bilinear) state-space matrices, which are mathematically related to the Volterra kernels. Some work has been done in this area, but there is significantly more work that needs to be done.

6.2. POD summary

The results reviewed in this paper demonstrate the viability of POD-based reduced-order models (ROM) for rapid analysis of aerodynamic and aeroelastic problems. The frequency-domain approach of Hall et al. [50] has previously been shown to predict accurately the linearized response of structurally coupled airfoils in transonic flow. As is typical in the use of POD-based ROMs, the computational cost of constructing low-order models through the frequency-domain approach is dominated by sampling (snapshot collection). Solutions are required for discrete distributions of frequency in each of the characteristic modes of deformation (pitch and plunge in the case of the structurally supported airfoil). The cost of obtaining a large number of snapshots can exceed that required to execute a small number of general simulations. However, several important benefits in the application of POD to aeroelastic problems are suggested by the work of Hall et al. for 2-D airfoils [50] and Thomas et al. for 3-D wings [101]. Following the one-time construction of a very low-order aeroelastic model, effects of parametric variations in the structural dynamics model can be rapidly assessed. Furthermore, the consequences of more fundamental changes to the structural model, such as freeplay [57], can be understood with greater clarity. The extension to higher level multi-disciplinary applications, e.g., aeroservoelasticity or design with aeroelastic constraints, may be made practical by the presence of low-order models. Lastly, the frequency domain POD represents an efficient and accurate compression of the salient dynamic characteristics of the aeroelastic system. In summary, the efficiencies of POD-based ROMs are realized when system properties can be characterized and observed once for ROM construction and then be allowed to vary in new ways compatible with the previous observations.

Application of the subspace projection method to the steady-state analysis of inviscid, compressible flow over a bump has yielded significant insight into the suitability of POD-based methods for nonlinear aerodynamic and aeroelastic analysis. By collecting a nominal number of solution samples over a two-parameter space, defined by bump amplitude and freestream Mach number, a POD-based ROM was constructed that preserved the nonlinear transition of supersonic flow states towards transonic states. Not surprisingly, we observed that the range of validity (as measured by a residual norm of the full system) of the ROM decreased as the number of retained modes was decreased. Interestingly, validity was longest lasting in the linear region of the parameter space (small amplitude for given Mach number), suggesting that low-energy modes were important in the accurate capture of nonlinear behavior, as also seen in the dynamic analysis. Computation of ROM solutions required approximately two orders of magnitude fewer function evaluations, which allowed a much more rapid and detailed exploration of the previously sampled solution space. We speculate that such ROMs are more reliable and useful than interpolation, although this assertion should be documented. Aside from the potential advantages of data compression (i.e., keeping fewer modes than fully represented by the snapshot data), which could be significant in large systems characterized by large numbers of parameters, POD provides a compact set of degrees of freedom (DOFs) that can be varied to evaluate sensitivities, optimal configurations, and system stability in a manner based on the discrete equations of the full system.

Unsteady aerodynamic solutions were also obtained with the subspace projection method at a significant computational savings over standard analysis. Results were reported for the response of a supersonic flow over a bump, like that described in the steady analysis, whose amplitude varied sinusoidally in time. Following construction of a ROM, the time-dependent character of the reduced-order system was accurately and efficiently computed with a sub-iterate form of the implicit Crank–Nicolson scheme. Time-dependent solutions of the ROM were computed an order of magnitude faster than full-system analysis. As true of the steady-state analysis, the computational cost associated with application of the POD-based ROM was dominated by the cost of data sampling used in ROM construction. The relative significance of the sampling cost can be minimized by constructing hybrid ROMs that account for frequency and amplitude variations and which are robust over a wider range of possible bump dynamics.

Efficiency of the subspace projection technique was derived from two sources: decrease of the number of variables that characterize the system and increase of allowable time step. In the bump problem, the number

of variables was decreased by three orders of magnitude (40,000 to about 10). However, the method was not three orders of magnitude faster since evaluations of the full-system source term ($\mathbf{R}$ in (15)) were required with this approach. For steady analysis, full-system evaluations were employed in the construction of the ROM Jacobian, and in unsteady analysis, full-system evaluations were also necessary in the computation of dynamic residuals. With the POD-based ROM, computational work associated with implicit portions (i.e., left-hand sides) of system equations was virtually eliminated. Thus, the subspace projection method was particularly well suited for implicit formulations of nonlinear problems, such as steady-state, sensitivity and bifurcation analyses. For unsteady problems, it was also found that time steps allowed by POD-based ROMs were an order of magnitude larger than that allowed by explicit, full-system analysis. The current approach should be compared to the computation of a relevant viscous flow using a standard implicit technique to determine potential savings for a practical problem.

Once sampling identifies the most energetic POD modes, other techniques are available with which the governing equations can be reduced in order. The relative merits and demerits of the Direct, Galerkin, and subspace projection methods are described in the Analysis section. Both Direct and Galerkin approaches have been applied to the Euler equations in an initial application with promising results [108]. Both Galerkin and Direct projections required artificial dissipation to stabilize the ROM realizations, which lead to the development of a hybrid POD/Volterra method [91,109] that produced stable, linear ROMs. The next challenge in this area involves the identification of nonlinear terms and their inclusion in low-order ROM realization. The extension of the POD to 3-D applications awaits the further refinement of systems identification techniques and deforming grid methodologies.

6.3. Harmonic balance (HB) summary

An alternative approach to POD based on HB has been proposed by Hall, Thomas and Clark [60] for the efficient computation of complex, time-periodic systems. With their technique, the response of a rotor flow field to rotor pitch oscillation was accurately simulated, and behaviors related to shock movement and shock/boundary-layer interaction were captured. Of all the techniques described in this paper, HB is the most mature, with successful applications in 3-D and current work extending HB to complex geometries.

Adaptive HB was introduced as a novel advancement that is still in its infancy. Adaptive HB shows promise for increased fidelity, reduced computational expense, and improved stability. The applicability of adaptive HB to aeroelastic problems of interest remains to be

demonstrated as the new approach has been applied in only 1-D to date.

6.4. Future challenges

In closure, several methods have been described in this paper that offer new potential for the computational analysis of large, nonlinear systems. These methods share a common reliance on existing numerical techniques and in this sense do not replace traditional methods. Instead, reduced-order and HB techniques provide existing methods with a higher level of algorithmic operation that enables more sophisticated computations. For example, a POD-based ROM of a discretized CDR system was described and shown capable of determining a variety of important characteristics of the nonlinear system, including nonlinear static behavior, bifurcation to limit-cycle behavior, and sensitivity to changes in system parameters. The CDR problem serves as an analog for the study of the aeroelastic properties of a wing, including static analysis (e.g., determination of a control-surface reversal speed), dynamic analysis (e.g., prediction of a limit-cycle oscillation amplitude), bifurcation analysis (e.g., at what reduced velocities of the nonlinear system does flutter occur), and sensitivity analysis (e.g., how do aeroelastic behaviors depend on structural parameters). Aeroelastic analysis of all these behaviors in a manner that is useful for structural or aeroservoelastic design is well beyond traditional methods. It is by answering more difficult questions, typically in the framework of multidisciplinary analysis, that ROM techniques become attractive, if not necessary.

There are several challenges that need to be overcome before ROM methods can be routinely applied to practical problems. We group these difficulties into three categories: construction, generality, and accuracy assessment. Which ROM method should be applied to a particular problem will probably depend on the relative significance of these issues to the specified problem, the analyst's ability and/or desire to modify available computational procedures, and the degree to which a low-order representation of the system is needed. By construction, we mean the process by which the low-order model is built, an issue dominated by how easily and effectively data samples can be computed. Generality is a separate issue encompassing the question of how readily or stubbornly the technique may be extended to different problems, particularly those involving different simulation tools or response characteristics. Finally, accuracy assessment is an important topic dealing with the ability to evaluate the quality, inherently or a posteriori, of ROM solutions.

Limited attention has been given to the construction of ROMs, particularly with POD techniques. While careful thought has been given to constructing frequency-robust ROMs (from frequency-domain methods), much work is needed to understand what response behaviors should be sampled in the construction of POD-based ROMs to model robustly the response characteristics of systems with large numbers of system parameters. In other words, how much sampling is required for a particular but arbitrary nonlinear system? On a related theme, there are different ways in which parameters can become represented in the derived low-order systems. Ideally, free parameters should remain identified in the ROMs, but this ideal may not be easily accomplished. For example, it may be difficult for the Galerkin projection method to produce ROMs with preserved parameters if the parameters are spatially varying, and appear buried within nonlinear relationships in the governing equations. The subspace approach avoids this complication by occasional evaluation of the full-order residual, but this approach is costly. Direct projection could cope with more complicated parametric expressions, although we envision that additional expansion terms would have to be computed to approximate the parametric dependence. As both POD and Volterra are semi-empirical in nature, we expect that each of these approaches will be challenged in similar fashions. However, since Volterra treats the full-order method as a "black box", handling parametric variation is anticipated to be more difficult than with POD. In contrast, the HB technique, which does not involve a compression of spatial data, preserves parametric relationships without loss of fidelity.

Generality of these new techniques is also an important consideration. Once methods are ready to be transitioned beyond demonstrative problems, sensible questions arise. Is the method readily or stubbornly extendable to different problems (perhaps exhibiting different physical processes) involving different simulation tools? Can the method function with modern, shock-capturing, CFD algorithms that incorporate turbulence models and deforming meshes with unstructured or structured/overset connectivities? Certainly, data oriented model reduction techniques are most general, functioning as higher level algorithms that allow high-fidelity simulation tools to be abstracted as data generating objects. The Volterra approach appears to yield the greatest generality, provided that system inputs and outputs are clearly defined and relatively small in number. Use of the POD enables the development of an extensible framework for treating large systems that experience a number of prototypical nonlinear behaviors. One barrier to wider generality of POD is the potential for discontinuous solution behavior (moving discontinuities), which interferes with the definition and use of global modes. We have documented ways to deal with this situation, but these strategies demand a limited level of intrusion into the system that currently is not automated. HB is less general because it is constrained

to time-periodic systems; however, there are a wide range of important applications that fall within this constraint. The HB method is itself a solution algorithm, and adapting existing time-domain production codes to incorporate HB is not expected to be simple even economical in some cases. For disciplines dominated by periodic, time-dependent solutions, such as aeroelasticity, it makes sense to invest in new applications tailored to the HB approach.

Furthermore, the accuracy of ROMs must be quantifiable for confident use, which is one of the more challenging issues to address. The spectral temporal accuracy and consistent spatial discretizations associated with HB provide a sound basis for traditional convergence analysis. Two sources of error challenge POD and Volterra techniques: incomplete training and training inconsistent with application. Systematic procedures must be developed (such as residual monitoring) to self-check ROM solutions and highlight conditions upon which ROMs should be re-constructed. We maintain the philosophy that access to the high-fidelity simulation tool is needed to enable periodic re-evaluation of the solution implied by the low-order model. Such a link is maintained and can be exploited, for example, in the subspace projection method, although with the liabilities expressed above.

And finally, we consider the issue of model efficiency. Each of the methods described in this review represents great improvement over traditional, high-fidelity, time-domain techniques for a number of problem classes. It is difficult to quantify the level of improvement that could be *routinely* expected out of these new methods because of changes in problem complexity and other real computational challenges, but it is clear how well the techniques can potentially work. With POD, problems of reasonable complexity, even in 3-D, can be captured with $O(100)$ modes. Construction of a reduced-order system of this size would permit very fast modeling, even real-time, of the desired system. For applications such as modeling and simulation, test and evaluation, control design, and engineering design analysis, synthesis of low-order models may be the only foreseeable way to account for nonlinear behavior, whether these models are obtained with POD, Volterra, or some other nonlinear system identification technique. However, it should be remembered that semi-empirical methods require data sampling, a cost that may be significant. For POD, the cost can be on the order of a tenth of the cost of modeling the complete system once. The training costs associated with Volterra would appear to be somewhat less, owing to the rapidity with which impulse responses die out. Thus, we conclude that while data compression strategies may do no worse than an $O(10)$ improvement over traditional methods for suitable problems computed once, much greater efficiencies, bounded by the ratio of order reduction (which can be

very large, approaching 10^{4-5} for 3-D problems) can be achieved if repeated use of the low-order model can be made (e.g., in parametric variations). Whether or not this situation exists is problem and purpose dependent. In the computation of time-periodic systems, implicit time-domain algorithms routinely require $O(100)$ time steps per cycle (although especially robust implicit methods may require fewer operations). In contrast, when harmonic content is relatively low, such as in aeroelasticity applications, harmonic balance techniques may capture the relevant dynamics in only a few harmonics, potentially representing a near two order of magnitude improvement over traditional approaches. This level of improvement should be regarded as an upper limit on efficiency (except when very close to Hopf bifurcation points where time-domain methods converge to limit cycles very slowly). HB reduces the temporal DOFs and not the spatial DOFs where the potential for reduction is much greater.

With the studies described in this review, it is evident that new methods are available for tackling tough problems in computational physics with a great deal of economy. A very positive result of this situation is that there is potential for modeling system nonlinearities in practical situations previously thought to be inconsistent with high-fidelity analysis. With a number of approaches available, the definition and study of benchmark problems of wide interest will help guide researchers towards a better understanding of the potentialities and limitations of these methods.

insights are helping us understand the various aspects of ROM techniques.

References

[1] Silva WA. Discrete-time linear and nonlinear aerodynamic impulse responses for efficient CFD analyses. Ph.D. thesis, College of William & Mary, December 1997.

[2] Bisplinghoff RL, Ashley H. Principles of aeroelasticity. New York: Dover; 1975.

[3] Giesing JP, Kalman TP, Rodden WP. Subsonic unsteady aerodynamics for general configurations, Part I. Direct application of the nonplanar doublet lattice method. Report AFFDL-TR-71-5, vol. I, November 1971.

[4] Leishman J, Crouse G. A state-space model of unsteady aerodynamics in a compressible flow for flutter analyses. AIAA Paper 89-0022, January 1989.

[5] Nixon D. Alternative methods for modeling unsteady transonic flows, unsteady transonic aerodynamics. Progress in Astronautics and Aeronautics, vol. 120. New York: AIAA; 1989.

[6] Reisenthel PH. Development of a nonlinear indicial model for maneuvering fighter aircraft. AIAA Paper 96-0896, January 1996.

[7] Marques F, Anderson J. Modelling and identification of non-linear unsteady aerodynamic loads by neural networks and genetic algorithms. ICAS Paper 96-7.1.1, September 1996. p. 243–51.

[8] Govind G, Ramamoorthy PA. Multi-layered neural networks and Volterra series: the missing link. IEEE International Conference on Systems Engineering, August 9–11, 1990. p. 633–6.

[9] Soloway DI, Bialasiewicz JT. Neural network modeling of nonlinear systems based on Volterra series extension of a linear model. IEEE International Symposium on Intelligent Control, Glasgow, Scotland, 1992.

[10] Dowell EH, Hall KC, Romanowski MC. Eigenmode analysis in unsteady aerodynamics: reduced order models. Appl Mech Rev 1997;50(6):371–85.

[11] Baker ML. Model reduction of large, sparse, discrete time systems with application to unsteady aerodynamics. Ph.D. thesis, University of California at Los Angeles, 1996.

[12] Seidel DA, Bennett RM, Ricketts RH. Some recent applications of XTRAN3S. AIAA Paper 83-1811.

[13] Lee-Rausch EM, Batina JT. Wing flutter computations using an aerodynamic model based on the Navier–Stokes equations. J Aircr 1996;33(6):1139–48.

[14] Raveh D, Levy Y, Karpel M. Aircraft aeroelastic analysis and design using CFD-based unsteady loads. AIAA Paper 2000-1325, April 2000.

[15] Silva WA, Raveh DE. Development of aerodynamic/aeroelastic state-space models from CFD-based pulse responses. AIAA 2001-1213, 42nd AIAA/ASME/ASCE/AH Structures, Structural Dynamics, and Materials Conference, Seattle, WA, 2001.

[16] Diaz H. Modeling of nonlinear systems from input–output data. Ph.D. thesis, Rensselaer Polytechnic Institute, 1986.

[17] Pitas I, Venetsanopoulos AN. Nonlinear digital fitters: principles and applications. Dordrecht: Kluwer Academic Publishers; 1990.

[18] Ueda T, Dowell EH. Flutter analysis using nonlinear aerodynamic forces. Proceedings of the 23rd AIAA/ASME/ASCE/AHS Structures, Structural, Dynamics, and Materials Conference, New Orleans, LA, AIAA Paper 82-0728-CP, p. 462–81.

[19] Tobak M, Pearson WE. A study of nonlinear longitudinal dynamic stability. NASA Technical Dissertation R-209.

[20] Jenkins JE. Relationships among nonlinear aerodynamic indicial response models, oscillatory motion data, and stability derivatives. Proceedings of the AIAA Atmospheric Flight Mechanics Conference, Boston, MA, August 1989 AIAA Paper 89-3351-CP.

[21] Stalford H, Baumann WT, Garrett FE, Herdman TL. Accurate modeling of nonlinear systems using Volterra series submodels. American Control Conference, Minneapolis, MN, June 1987.

[22] Rugh WJ. Nonlinear system theory, the Volterra–Wiener Approach. The John Hopkins University Press; 1981.

[23] Clancy SJ, Rugh WJ. A note on the identification of discrete-time polynomial systems. IEEE Trans Automat Control AC-24 December 1979 (6).

[24] Schetzen M. Measurement of the kernels of a nonlinear system of finite order. Int J Control 1965;1(3):251–63.

[25] Boyd SP, Chang YS, Chua LO. Measuring Volterra kernels. IEEE Trans Circuits Syst 1983; CAS-30(8).

[26] Reisenthel PH. Prediction of unsteady aerodynamic forces via nonlinear kernel identification. Presented at the International Forum on Aeroelasticity and Structural Dynamics, Williamsburg, VA, June 1999.

[27] Tromp JC, Jenkins JE. A Volterra kernel identification scheme applied to aerodynamic reactions. AIAA Paper 90-2803.

[28] Rodriguez EA. Linear and nonlinear discrete-time state-space modeling of dynamic systems for control applications. Ph.D. thesis, Purdue University, December 1993.

[29] Silva WA. Application of nonlinear systems theory to transonic unsteady aerodynamic responses. J Aircr 1993;30(5):660–8.

[30] Silva WA. Extension of a nonlinear systems theory to transonic unsteady aerodynamic responses. AIAA Paper 93-1590, April 1993.

[31] Karhunen K. Zur Spektral Theorie Stochastischer Prozesse. Ann Acad Sci Fennicae Ser 1946.

[32] Loeve M. Functions Aleatoire de Second Ordre. C R Academie des Sciences, Paris, France, 1945.

[33] Ahmed N, Goldstein MH. Orthogonal transforms for digital signal processing. Berlin: Springer; 1975.

[34] Lumley JL. The structure of inhomogeneous turbulence. In: Yaglom AM, editor. Proceedings of the International Colloquium in the Fine Scale Structure of the Atmosphere and its Influence on Radio Wave Propagation. Dokl Akad Nauk SSSR, Moscow, 1967. p. 166–78.

[35] Bakewell P, Lumley JL. Viscous sublayer and adjacent wall region in turbulent pipe flows. Phys Fluids 1967;10:1880–9.

[36] Berkooz G, Holmes P, Lumley JL. The proper orthogonal decomposition in the analysis of turbulent flows. Ann Rev Fluid Mech 1993;25:539–75.

[37] Masri SF, Smyth AW, Traina M-I. Probabilistic representation and transmission of nonstationary processes in multi-degree-of-freedom systems. Trans ASME 1998;65: 398–409.

[38] Jeong S-W, Bienkiewicz B, Ham H-J. Proper orthogonal decomposition of building wind pressure specified at non-uniformly distributed pressure taps. J Wind Eng Ind Aerodyn 2000;87:1–14.

[39] Krysl P, Lall S, Marsden JE. Dimensional model reduction in non-linear finite element dynamics of solids and structures. Int J Numer Meth Eng 2000, submitted for publication.

[40] Mortara SA, Slater JC, Beran PS. A proper orthogonal decomposition technique for the computation of non-linear panel response. AIAA Paper 2000-1936, 2000.

[41] Moin P, Moser RD. Characteristic-Eddy decomposition of turbulence in a channel. J Fluid Mech 1989;200: 471–509.

[42] Sirovich L. Turbulence and the dynamics of coherent structures. Part I: coherent structures. Q Appl Math 1987;45(3):561–71.

[43] Deane AE, Kevrekidis IG, Karniadakis GE, Orszag SA. Low-dimensional models for complex geometry flows: application to grooved channels and circular cylinders. Phys Fluids 1991;3(2):2337–54.

[44] Park HM, Cho DH. The use of the Karhunen–Loeve decomposition for the modeling of distributed parameter systems. Chem Eng Sci 1996;51(1):81–9.

[45] Park HM, Lee MW. An efficient method of solving the Navier–Stokes equation for flow control. Int J Numer Meth Eng 1998;41:1133–51.

[46] Rediniotis OK, Ko J, Yue X, Kurdila AJ. Synthetic jets, their reduced order modeling and applications to flow control. 37th Aerospace Sciences Meeting and Exhibit, Reno, NV, AIAA Paper 99-1000, January 1999.

[47] Tang KY, Graham WR, Peraire J. Active flow control using a reduced order model and optimum control. AIAA Paper 96-1946, 1996.

[48] Romanowski MC. Reduced order unsteady aerodynamic and aeroelastic models using Karhunen–Loeve Eigenmodes. 6th AIAA/USAF/NASA/ISSMO Symposium on Multidisciplinary Analysis and Optimization, Bellevue WA, AIAA 96-3981-CP, September 1996. p. 7–13.

[49] Kim T. Frequency-domain Karhunen–Loeve method and its application to linear dynamic systems. AIAA J 1998; 36(11):2117–23.

[50] Hall KC, Thomas JP, Dowell EH. Proper orthogonal decomposition technique for transonic unsteady aerodynamic flows. AIAA J (also AIAA Paper 99-0655) 2000;38(10):1853–62.

[51] Beran PS, Huttsell LJ, Buxton BJ, Noll C, Osswald G. Computational aeroelasticity techniques for viscous flow. CEAS/AIAA/ICASE/NASA Langley International Forum on Aeroelasticity and Structural Dynamics, Williamsburg, VA, June 1999.

[52] Pettit CL, Beran PS. Reduced-order modeling for flutter prediction. 41st AIAA/ASCE/AHS/ASC Structures, Structural Dynamics and Materials Conference, Atlanta, GA, AIAA Paper 2000-1446-CP, April 2000.

[53] Pettit CL, Beran PS. Application of proper orthogonal decomposition to the discrete Euler equations. Int J Numer Meth Eng December, 2000, submitted for publication.

[54] Beran PS, Pettit CL. Prediction of nonlinear panel response using proper orthogonal decomposition. Presented at the 42nd AIAA/ASCE/AHS/ASC Structures, Structural Dynamics and Materials Conference, Bellvue, WA, April 2001.

[55] Beran PS, Lucia DJ, Pettit CL. Reduced order modeling of limit-cycle oscillation for aeroelastic systems. IMECE 2002-32954, 2002 ASME International Mechanical Engineering Congress and Exposition, New Orleans, LA, November 17–22, 2002.

[56] Lucia DJ, Beran PS, King PI. Reduced order modeling of an elastic panel in transonic flow. J Aircr 2003;40(2): 338–47.

[57] Dowell EH, Thomas JP, Hall KC. Transonic limit cycle oscillation analysis using reduced order modal aerodynamic models. Presented at the 42nd AIAA/ASCE/AHS/ASC Structures, Structural Dynamics and Materials Conference, Bellvue, WA, April 2001.

[58] Maple RC. Adaptive harmonic balance method for unsteady, nonlinear, one-dimensional flows. Ph.D. thesis, Air Force Institute of Technology, School of Engineering and Management, 2002.

[59] Hayashi C. Nonlinear oscillations in physical systems. Princeton, NJ: Princeton University Press; 1964. p. 28–31.

[60] Hall KC, Thomas JP, Clark WS. Computation of unsteady nonlinear flows in cascades using a harmonic balance technique. Ninth International Symposium on Unsteady Aerodynamics, Aeroacoustics and Aeroelasticity of Turbomachines and Propellers, Lyon, France, September 4–8, 2000.

[61] Verdon JM, Caspar JR. Subsonic flow past an oscillating cascade with finite mean flow deflection. AIAA J 1980;(18):540.

[62] Verdon JM, Caspar JR. Development of a linear unsteady aerodynamic analysis for finite-deflection subsonic cascades. AIAA J 1982;(20):1259.

[63] Verdon JM, Caspar JR. A linearized unsteady aerodynamic analysis for transonic cascades. J Fluid Mech 1984; 149:403–29.

[64] Verdon JM. Linearized unsteady aerodynamic theory. In: Platzer MF, Franklin CO, editor. AGARD Manual on Aeroelasticity in Axial-Flow Turbomachines, vol. 1, Unsteady Turbomachinery Aerodynamics, No. AGARD-AG-298 in AGARDograph, AGARD, 1987.

[65] Hall KC, Crawley EF. Calculation of unsteady flows in turbomachinery using the linearized Euler equations. AIAA J 1989;27(6):777–87.

[66] Hall KC, Clark WS. Linearized Euler predictions of unsteady aerodynamic loads in cascades. AIAA J 1993;31(3):540–50.

[67] Verdon JM, Barnett M, Ayer TC. Unsteady aerodynamic models for turbomachinery aeroelastic and aeroacoustic applications. NASA Contractor Report NASA/CR 4698, NASA, November 1995.

[68] Cizmas PGA, Hall KC. A viscous-inviscid model of unsteady small-disturbance flows in cascades. AIAA 95-2655, 31st AIAA/ASME/SAE/ASEE Joint Propulsion Conference and Exhibit, San Diego CA, July 10–12, 1995.

[69] Verdon JM, Montgomery MD, Chuang AH. Development of a linearized unsteady Euler analysis with application to wake/blade-row interactions. NASA Contractor Report NASA/CR 1999-208879, NASA, November 1999.

[70] Hoyniak D, Clark WS. Aerodynamic damping predictions using a linearized Navier–Stokes analysis. ASME 99-GT-207, International Gas Turbine & Aeroengine Congress & Exhibit, Indianapolis IN, June 7–10, 1999.

[71] Clark WS, Hall KC. A time-linearized Navier–Stokes analysis of stall flutter. ASME 99-GT-383, International Gas Turbine & Aeroengine Congress & Exhibit, Indianapolis IN, June 7–10, 1999.

[72] Florea R, Hall KC. Sensitivity analysis of unsteady inviscid flow through turbomachinery cascades. AIAA Paper 2000-0130, January 2000.

[73] Ning W, He L. Computation of unsteady flows around oscillating blades using linear and nonlinear harmonic Euler methods. J Turbomach 1998;120:508–14.

[74] He L, Ning W. Efficient approach for analysis of unsteady viscous flows in turbomachines. AIAA J 1998;17(11):2005–12.

[75] Chen T, Vasanthakumar P, He L. Analysis of unsteady blade row interaction using nonlinear harmonic approach. AIAA J Propulsion Power 2001; 17(3):651–8.

[76] McMullen M, Jameson A, Alonso JJ. Acceleration of convergence to a periodic steady state in turbomachinery flows. AIAA 2001-0152, 39th AIAA Aerospace Sciences Meeting & Exhibit, Reno NV, January 8–11, 2001.

[77] Thomas JP, Dowell EH, Hall KC. Nonlinear inviscid aerodynamic effects on transonic divergence, flutter and limit cycle oscillations. April 16–19, 2001.

[78] McMullen M, Jameson A, Alonso JJ. Application of a non-linear frequency domain solver to the Euler and Navier–Stokes equations. AIAA 2002-0120, 40th AIAA Aerospace Sciences Meeting & Exhibit, Reno NV, January 14–17, 2002.

[79] Maple RC, King P, Wolff JM, Orkwiz PD. Adaptive harmonic balance method for nonlinear, time periodic flows. J Comput Phys 2004, submitted for publication.

[80] Maple RC, King P, Wolff JM, Orkwiz PD. Split-Domain harmonic balance solutions to Burger's equation for large amplitude disturbances. AIAA J 2003;41(2): 206–12.

[81] Maple RC, King P, Oxley ME. Adaptive harmonic balance solution to the Euler's equation. AIAA J 2004, submitted for publication.

[82] Volterra V. Theory of functionals and of integral and integro-differential equations. New York: Dover; 1959.

[83] Schetzen M. The Volterra and Wiener theories of nonlinear systems. New York: Wiley; 1980.

[84] Bendat JS. Nonlinear system analysis & identification from random data. New York: Wiley-Interscience; 1990.

[85] Silva WA. Reduced-order models based on linear and nonlinear aerodynamic impulse responses. CEAS/AIAA/ ICASE/NASA Langley International Forum on Aeroelasticity and Structural Dynamics, Williamsburg, VA, June 1999. p. 369–79.

[86] Boyd SP. Volterra series: engineering fundamentals. Ph.D. thesis, University of California, Berkeley, 1985.

[87] Oppenheim AV, Schafer RW. Discrete-time signal processing (Prentice Hall Signal Processing Series). Englewood Cliffs, NJ: Prentice Hall, 1989.

[88] Marzocca P, Librescu L, Silva WA. Nonlinear stability and response of lifting surfaces via Volterra series. Presented at the 20th International Congress of Theoretical and Applied Mechanics, Chicago, IL, 27 August–2 September, 2000.

[89] Prazenica R, Kurdila A, Silva WA. Multiresolution methods for representation of Volterra series and dynamical systems. AIAA Paper 2000-1754, April 2000.

[90] Juang JN, Pappa RS. An eigensystem realization algorithm for modal parameter identification and model reduction. J Guidance 1984;8(5):620–7.

[91] Lucia DJ, Beran PS. Reduced order model development using proper orthogonal decomposition and Volterra theory. AIAA J 2002, accepted for publication.

[92] Holmes P, Lumley JL, Berkooz G. Turbulence, coherent structures, dynamical systems and symmetry. Cambridge: Cambridge University Press; 1996.

[93] Newman AJ. Model reduction via the Karhunen–Loeve expansion part 1: an exposition. Technical Report T.R. 96-32, Institute for Systems Research, University of Maryland, 1996.

[94] Childers DG. Probability and random processes. New York: McGraw-Hill; 1997.

[95] Mallat SA. A wavelet tour of signal processing. San Diego: Academic Press; 1998.

[96] Strang G. Linear algebra and its applications, 3rd ed. New York: Harcourt Brace Jovanivich; 1988.

[97] Romanowski MC, Dowell EH. Aeroelastic analysis of an airfoil using eigenmode based reduced order unsteady aerodynamics. 36th AIAA/ASME/ASCE/AHS/ASC Structures, Structural Dynamics, and Materials Conference, New Orleans, LA, AIAA Paper 95-1380-CP, April 1995. p. 1863–1870.

[98] Beran PS, Morton SA. Continuation method for calculation of transonic airfoil flutter boundaries. J Guidance, Control Dyn 1997;20(6):1165–71.

[99] Morton SA, Beran PS. Hopf-bifurcation analysis of airfoil flutter at transonic speeds. J Aircr 1999;36(2): 421–9.

[100] Beran PS. A domain-decomposition method for airfoil flutter analysis. AIAA Paper 99-0098, January 1998.

[101] Thomas JP, Dowell EH, Hall KC. Three-dimensional transonic aeroelasticity using proper orthogonal decomposition based reduced order models. Presented at the 42nd AIAA/ASCE/AHS/ASC Structures, Structural Dynamics and Materials Conference, Bellvue, WA, April 2001.

[102] Slater JC, Pettit CL, Beran PS. In-situ residual tracking in reduced order modelling. Shock Vib 2002;9(3): 105–21.

[103] Beran P, Silva W. Reduced order modeling: new approaches for computational physics. AIAA 2001-0853, 39th Aerospace Sciences Meeting and Exhibit, Reno, NV, January 2001.

[104] Beran PS, Pettit CL. In: Atluri SN, Brust FW, editors. Computational aeroelasticity for multidisciplinary optimization. Advances in Computational Engineering and Sciences 2000 (Collection of Papers presented at the ICES

2K Conference) vol. 2. Tech Science Press, August 2000. p. 1562–7.

[105] Isaacson E, Keller HB. Analysis of numerical methods. New York: Wiley; 1966.

[106] Lucia DJ, King PI, Beran PS. Domain decomposition for reduced-order modeling of a flow with moving shocks. AIAA J 2002;40(11):2360–2.

[107] Lucia DJ, King PI, Beran PS. Reduced order modeling of a two dimensional flow with moving shocks. Comput Fluids 2003;32:917–38.

[108] Lucia DJ, Beran PS. Projection methods for reduced order models of compressible flows. J Comput Phys 2003; 188(1):252–80.

[109] Lucia DJ, Beran PS, Silva WA. Aeroelastic system development using proper orthogonal decomposition and Volterra theory. AIAA 2003-1922, 44th AIAA/ASME/ASCE/AHS Structures, Structural Dynamics, and Materials Conference, Norfolk, VA, April 7–10, 2003.

[110] Naylor AW, Sell GR. Linear operator theory in engineering and science. New York, NY: Springer; 1982.

[111] Stakgold I. Green's functions and boundary value problems, 2nd ed. Washington, DC: Wiley; 1998.

[112] Marsden J, Tromba A. Vector calculus. New York: W. H. Feeman and Company; 1981. p. 200–4.

[113] Lucia DJ. Reduced order modeling for high speed flows with moving shocks. Ph.D. thesis, Air Force Institute of Technology, School of Engineering and Management, 2001.

[114] Strang G. Introduction to applied mathematics. Cambridge, MA: Wellesley Cambridge Press; 1986.

[115] Anttonen JSR. Techniques for reduced order modeling of aeroelastic structures. Ph.D. thesis, Air Force Institute of Technology, School of Engineering and Management, 2001.

[116] Anttonen JSR, King P, Beran PS. Application of multi-POD to a pitching and plunging airfoil. Int J Math Comput Modeling, 2003.

[117] Willcox K, Peraire J. Balanced model reduction via the proper orthogonal decomposition. AIAA J 2002; 40(11):2323–30.

[118] Moore B. Principal component analysis in linear systems. IEEE Trans Automat Control 1981;AE26(1): 17–31.

[119] Lall S, Marsden J, Glavaski S. Airfoil design optimization using reduced order models based on proper orthogonal decomposition. Proceedings of the IFAC World Congress, vol. F, International Federation of Automatic Control, Beijing, 1999. p. 473–8.

[120] Guruswamy GP, Tu EL. Navier–Stokes computations on flexible advanced transport wings in transonic regime. J Aircr 1996;33(3):576–81.

[121] Gordnier RE, Melville RB. Accuracy issues for transonic wing flutter using 3-D Navier–Stokes. Proceedings of the 39th AIAA/ASME/ASCE/AHS/ASC Structures, Structural Dynamics, and Materials Conference, Long Beach, CA, AIAA Paper 98-1729-CP, April 1998.

[122] Parker TS, Chua LO. Practical numerical algorithms for chaotic systems. New York, NY: Springer; 1989.

[123] Nayfeh A, Balachandran B. Applied nonlinear dynamics. New York, NY: Wiley; 1995.

[124] Seydel R. From equilibrium to chaos: practical bifurcation and stability analysis. Amsterdam: Elsevier Science; 1988.

[125] Holodniok M, Kubicek M. DERPER—An algorithm for the continuation of periodic solutions in ordinary differential equations. J Comput Phys 1984;55: 254–67.

[126] Beran PS. Computation of limit-cycle oscillation using a direct method. AIAA Paper 99-1462, April 1999.

[127] Schwer DA, Green Jr WH. Split-operator methods for computing steady-state reacting flow fields. AIAA 2001-2635, 15th AIAA Computational Fluid Dynamics Conference, Anaheim, CA, June 11–14, 2001.

[128] Silva WA, Bartels RE. Development of reduced order models for aeroelastic analysis and flutter prediction using the CFL3Dv6.0 Code. AIAA 2002-1594, 43rd AIAA/ASME/ASCE/AHS Structures, Structural Dynamics, and Materials Conference, Denver, CO, April 22–25, 2002.

[129] Rumsey CL, Biedron RT, Thomas JL. CFL3D: Its history and some recent applications. NASA TM 112861, May, 1997.

[130] Raveh DE, Levy Y, Karpel M. Structural optimization using computational aerodynamics. International Forum on Aeroelasticity and Structural Dynamics, Williamsburg, VA, June 1999 p. 469–81.

[131] Marzocca P, Librescu L, Silva WA. Flutter, postflutter, and control of a supersonic wing section. J Guidance Control Dyn 2002;25(5):962–70.

[132] Marzocca P, Librescu L, Silva WA. Aeroelastic response of nonlinear wing sections using a functional series technique. AIAA J 2002;40(5):813–24.

[133] Marzocca P, Librescu L, Silva WA. Aeroelastic response and flutter of swept aircraft wings. AIAA J 2002;40(5): 801–12.

[134] Silva WA, Piatak DJ, Scott RC. Identification of experimental unsteady aerodynamic impulse responses. AIAA 2003-1959, 44th AIAA/ASME/ASCE/AHS Structures, Structural Dynamics, and Materials Conference, Norfolk, VA, April 7–10, 2003.

[135] Silva WA, Hong MS, Bartels RE, Piatak DJ, Scott RC. Identification of computational and experimental reduced-order models. International Forum on Aeroelasticity and Structural Dynamics, Amsterdam, the Netherlands, June 4–6, 2003.

[136] Haji MR, Silva WA. Nonlinear flutter aspects of the flexible HSCT semispan model. International Forum on Aeroelasticity and Structural Dynamics, Amsterdam, the Netherlands, June 4–6, 2003.

[137] Isogai K. On the transonic-dip mechanism of flutter of sweptback wing. AIAA J 1979;17(7):793–5.

[138] Ehlers FE, Weatherhill WH. A harmonic analysis method for unsteady transonic flow and its application to the flutter of airfoils. NASA CR-3537, May 1982.

[139] Edwards JW, Bennet RM, Whitlow Jr. W, Seidel DA. Time-marching transonic flutter solutions including angle-of-attack effects. J Aircraft 1983;20(11):899–906.

[140] Lee-Rausch EM, Batina JT. Wing flutter boundary prediction using unsteady Euler aerodynamic method. J Aircr 1995;32(2):416–22.

[141] Epureanu BI, Dowell EH, Hall KC. Mach number influence on reduced-order models of inviscid potential flows in turbomachinery. J Fluids Eng 2002;124:977–87.

[142] Epureanu BI, Hall KC, Dowell EH. Reduced order models in turbomachinery using inviscid-viscous coupling. J Fluids Struct 2001;15(2):255–76.

[143] Epureanu BI, Dowell EH, Hall KC. A parametric analysis of reduced order models of potential flows in turbomachinery using proper orthogonal decomposition. 2001-GT-0434, Proceedings of ASME Turbo-Expo 2001, New Orleans, LA, June 4–7, 2001.

[144] Cizmas PG, Palacios A. Proper orthogonal decomposition of turbine rotor–stator interaction. J propulsion Power 2003; 19(2).

[145] Ito K, Ravindran SS. A reduced-order method for simulation and control of fluid flows. J Comput Phys 1998;143:403–25.

[146] Shvartsman SY, Kevrekidis IG. Nonlinear model reduction for control of distributed systems: a computer-assisted study. Am Inst Chem Eng 1998;44(7):1579–95.

[147] Banerjee S, Cole JV, Jensen KF. Nonlinear model reduction strategies for rapid thermal processing systems. IEEE Trans Semicond Manuf 1998;11(2):266–75.

[148] Kunisch K, Volkwein S. Control of the Burgers equation by a reduced-order approach using proper orthogonal decomposition. J Optim Theory Appl 1999;102(2):345–71.

[149] Harten A. High resolution schemes for hyperbolic conservation laws. J Comput Phys 1983;49:357–93.

[150] Yee HC. A class of high-resolution explicit and implicit shock capturing methods. NASA TM-101088, 1989.

[151] Strang WZ, Tomaro RF, Grismer MJ. The defining methods of Cobalt60: a parallel, implicit, unstructured Euler/Navier–Stokes flow solver. AIAA Paper 99-0786.

[152] Brooks GP, Powers JM. A Karhunen–Loeve Galerkin technique for optimization of a blunt body geometry. AIAA 2002-3861, 38th AIAA/ASME/SAE/ASEE Joint Propulsion Conference and Exhibit Conference, Indianapolis, IN, July 7–10, 2002.

[153] Dobbs SK, Miller GD, Stevenson JR. Self induced oscillation wind tunnel test of a variable sweep wing. Proceedings of the AIAA/ASME/ASCE/AHS 26th Structures, Structural Dynamics and Materials Conference, Orlando, FL, April 15–17, AIAA Paper 85-0739-CP, 1985.

[154] Cunningham AM. The role of non-linear aerodynamics in fluid–structure interactions. AIAA Paper 98-2423, 1998.

[155] Heinemann RF, Poore AB. Multiplicity, stability and oscillatory dynamics of the tubular reactor. Chem Eng Sci 1981;36:1411–9.

[156] Roose D, Hlavacek V. Numerical computation of Hopf bifurcation points for parabolic diffusion-reaction differential equations. Appl Math 1983;43(5):1075–85.

[157] Gordnier RE, Visbal MR. Development of a three-dimensional viscous aeroelastic solver for nonlinear panel flutter. AIAA 2000-2337, Fluids 2000 Conference and Exhibit, Denver, CO, June 19–22, 2000.

[158] Lions J, Pironneau O. Non overlapping domain decomposition for evolution operators. C R Acad Sci Ser I Mathematique 2000;330(10):943–51.

[159] Yu H. Solving parabolic problems with different time steps in different regions in space based domain decomposition methods. Appl Numer Math: Trans IMACS 1999;30(4):475.

[160] Bendiksen OO, Davis GA. Nonlinear traveling wave flutter of panels in transonic flow. AIAA 1995-1486, 1995.

[161] Antonnen JSR, King PI, Beran PS. The accuracy of POD bases reduced-order models with deforming grids. AIAA 2001-2541, 19th AIAA Computational Fluid Dynamics Conference, Anaheim, CA, June 2001.

[162] Anttonen JSR, King P, Beran PS. POD-based reduced-order models with deforming grids. Int J Math Comp Modeling 2003;38:41–62.

[163] Cizmas PG, Palacios A, O'Brien T, Syamlal M. Proper orthogonal decomposition of spatio-temporal patterns in fluidized beds. Chem Eng Sci 2003;58(19):4417–27.

[164] Kuipers JAM, Tammes H, Prins W, van Swaaij WPM. Experimental and theoretical porosity profiles in a two-dimensional gas-fluidized bed with a central jet. Powder Tech 1992;71:87–99.

[165] Hall KC, Thomas JP, Clark WS. Computation of unsteady nonlinear flows in cascades using a harmonic balance technique. AIAA J 2002;40(5):879–86.

[166] Spalart PR, Allmaras SR. A one equation turbulence model for aerodynamic flows. AIAA Paper 92-0439, 1992.

[167] Thomas JP, Dowell EH, Hall KC. Nonlinear inviscid aerodynamic effects on transonic divergence, flutter, and limit cycle oscillations. AIAA J 2002;40(4):638–46.

[168] Thomas JP, Hall KC, Dowell EH. Modeling viscous transonic limit cycle oscillation behavior using a harmonic balance approach. April 22–25, 2002.

[169] Thomas JP, Dowell EH, Hall KC. A harmonic balance approach for modeling three-dimensional nonlinear unsteady aerodynamics and aeroelasticity. IMECE 2002-32954, 2002 ASME International Mechanical Engineering Congress and Exposition, New Orleans, LA, November 17–22, 2002.

[170] Thomas JP, Hall KC, Dowell EH. A Harmonic balance approach for modeling nonlinear aeroelastic behavior of wings in transonic viscous flow. April 7–10, 2003.

[171] Thomas JP, Dowell EH, Hall KC. Transonic flutter simulations using an implicit aeroelastic solver. J Aircr 2000;37(5):872–9.

[172] Hoffman KA, Chiang ST. Computational fluid dynamics, vol. II, 4th ed. Wichita: Engineering Education System; August 2000. p. 133–51.